Cranfield University

Zakaria Mouti

Localised Low Velocity Impact Performance of Short Glass Fibre Reinforced Polyamide 66 Oil Pans

School of Applied Sciences

Environmental Science & Technology

PhD Thesis

2012

Supervisor: Dr. James Njuguna

Date of presentation: 30/03/2012

"This thesis is submitted in partial fulfilment of the requirements for the Degree of Doctor of Philosophy in Composites Structures."

Abstract

This thesis focuses on the mechanical properties of short glass fibre reinforced polyamide 66 material used in automotive composite structures, and its impact resistance under localised low velocity impact. The main application of this research concerns the impact performance of an oil pan component susceptible to stone impact damage.

The thesis reviews the current state-of-the-art of thermoplastic polyamide materials with an overview of the glass fibre reinforced polyamide under-the-hood components, as well as its manufacturing and processing techniques. The study explores much of the work published in the literature so as to identify the fundamental parameters determining the impact resistance. It then concentrates on assessing the mechanical properties of the material subjected to quasi-static loads and impacts considering the influence and consequences of atmospheric or weathering conditions such as the moisture and salt uptake and the variation of temperature.

The experimental work employed a universal testing machine for the quasi-static tests, drop weight tower and projectile air gun to carry out the dynamic tests. The testing involves different polyamide grades and impact modifier material in small specimens and full-scale oil pan components so as to gain important insights into the material-geometrical coupling effects.

In correlation with the experiments, a finite element analysis was conducted to predict capability and simulate impact events using LS-DYNA solver. The simulation allowed putting to the test and comparing different protective design features. The post-testing investigations focused on the damage assessment and failures at micro- and macro-scales on the structure using visual inspection, scanning electron microscopy and ultrasound flaw detector. This was intended to bring detailed understanding of the failure mechanisms and also shed some light into damage tolerance of typical under-the-hood thermoplastic polyamide components.

Investigation results indicated that impact resistance properties of short glass fibre reinforced polyamide 66 grades are sensitive and influenced by moisture and salt uptakes, temperature ageing and air oxidation. In general, the increase of these parameters reduces the material strength but at the same time improves its strain. The study also compares different structures and shows the significant contribution of the design in terms of shock absorption and stress distribution. The proposed oil pan design with protective ribbing pattern combined with a superior material with rubbery phase considerably improves the impact resistance of the full-scale automotive component studied.

Acknowledgments

I would like to thank Dr. James Njuguna for all the support and guidance that he gave me throughout this challenging research project. I am very grateful to my officemates and friends for their joyfulness at work, the good times we shared and their supports in anyway.

This thesis is supported by the Engineering and Physical Sciences Research Council (EPSRC) under the grant CASE/CAN/07/40, to which I am very grateful for their support and for letting me use their equipment. Many thanks to Keith Westwood and Darren Long from Eaton Corporation UK for their financial support on this project, for providing me material samples and oil pan components for testing. Thanks again for sharing with me some interesting and useful information for the good progress of my work. I also wish to thank Keith Pottinger and Martyn Eccles from Sabre Ballistics for their help in the ballistic field and their experimental air gun apparatus.

Nomenclature and abbreviations

Nomenclature

Units

Length	m	metre
Time	s	second
Mass	kg	kilogram
Force	N	newton
Pressure	Pa	pascal
Velocity	m/s	metre per second
Density	kg/m^3	kilogram per cubic metre
Energy	J	joule
Temperature	°C	degree Celsius

Homogeneous units for simulation

Length	mm (10^{-2} m)	millimetre
Time	s	second
Mass	t (10^3 kg)	tonne
Force	N	newton
Pressure	MPa (10^6 Pa)	megapascal
Velocity	mm/s	millimetre per second
Density	t/m^3 (10^3 kg/m^3)	tonne per cubic metre
Energy	mJ	millijoule

Abbreviations

PA6	Polyamide 6
PA66	Polyamide 66
SGFR	Short glass fibre reinforced
wt%	Weight content ratio
GFwt%	Glass fibre and weight content ratio
ASTM	American Society for Testing and Materials
ISO	International Organization for Standardization
SEBS	Styrene ethylene / butylene styrene
EPDM	Ethylene propylene diene monomer
EPR	Ethylene propylene rubber
SBR	Styrene butadiene rubber
g	Grafted
MA	Maleic anhydride
$CaCl_2$	Calcium chloride
EG	Ethylene glycol
aq.	Aqueous
Me	Methanol

Contents

List of figures

List of tables

Chapter 1. Introduction

1.1. Background

A main concern in the automotive industry is the vehicle weight reduction so as to help reduce fuel consumption and therefore emission levels. One way to realise this objective and meet the challenge of cost and performance is by the use of glass fibre reinforced thermoplastic composites using long or short fibres [1]. They offer distinct advantages over more conventional engineering materials such as aluminium and steel including higher specific strength and stiffness and superior corrosion resistance as well as improved fatigue properties [2-6].

Injection moulded short glass fibre reinforced thermoplastic composites are currently the most prevalent material [7-9]. Figure 1 is one example illustrating this tendency and shows a wet engine oil pan currently in application made of short glass fibre reinforced polyamide 66 (SGFR PA66).

A wet engine oil pan is a very important component in a vehicle since the moving parts of the engine need to be lubricated and cooled by the oil. A wet oil pan stores the oil which is pumped by an oil pump to the top of the engine and drains down towards the oil pan. The wet oil pan system is the

most common type of oil pan and differs from a dry oil pan system which uses a remote oil reservoir to store the excess of oil. A dry system has the advantage to avoid the oil to slosh around in hard cornering or braking situations; although a wet oil pan can uses baffles and trap doors to control the movement of the oil; but a dry system has more parts therefore adds more weight and it is complex thus costly [10].

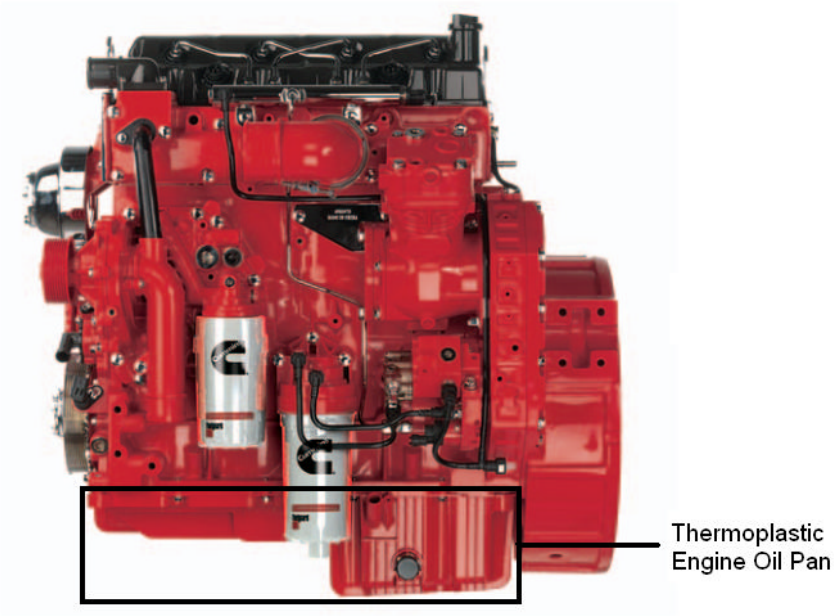

Figure 1 - Thermoplastic engine oil pan fitted on ISF 3.8 Cummins Engine [8]

There are many studies that have been performed in order to investigate the impact properties of thermoplastic composites [2; 11-19]. Low velocity impacts are known to induce damage to the composite in the

form of matrix cracking, delamination, debonding and fibre breakage. A number of studies on the low velocity impact performance of thermoplastic-matrix composites have been conducted but, in most cases, the composites were fully laminated into relatively rigid plates made of polyethylene terephthalate [2; 15], polypropylene [13; 17; 18], polyethylene [19-22] and polyether ether ketone [12; 23] fibre reinforcement. Research has shown that composites are capable of absorbing energy and dissipating it by various fracture and elastic processes when subjected to a low velocity impact [17]. The ability of these materials to absorb energy elastically depends on the mechanical properties of the matrix and fibres, the interfacial strength, the velocity of impact and the size of the component. Polymer matrix composites are known to be highly susceptible to internal damage caused by transverse loads even under low velocity impact [18]. For the effective use of polymer matrix composites in higher performance applications, it is important to understand the cause of damage formation under low velocity impact conditions as well as the potential for improvement of damage resistance characteristics of composites.

Despite increased use in under-the-hood applications [24], published work on the impact behaviour of polyamide short fibre reinforced thermoplastic composites is limited. The polyamide (PA) family consists of different grades depending upon the way they were polymerised. PA6 and PA66 are the most popular forms of polyamides [25]. The automotive

market, principally for new under-the-hood applications, consumes more than 40% of the PA6 and PA66 produced. These materials have a particular utility in performing mechanical duties that traditionally relied on metal parts. However, polyamides have some limitations and the most significant of these is their response to localised impact loading [26-31]. Thus, material substitution involves making sure that the new parts are service lifetime capable. Few available studies have looked into the fracture toughness and the impact behaviour of samples of polyamide plates but mainly focus on fibre content and length effects [32; 33]. These studies found that the addition of around 30-40% weight content ratio (wt%) of short glass fibres on a thermoplastic matrix led to an improvement of fracture toughness with a minor advantage for long fibres. The impact resistance increased with the thickness; nonetheless, the relationship established was valid only in the examined range. Most impact studies use a drop weight testing machine to assess the impact resistance of composites but the impactor type and geometry used in reported studies are different and tests are mostly done on square plates, eliminating the geometry effect that a full component could have.

1.2. Aims and objectives

One of the key concerns in the use of thermoplastic oil pan is that this automotive part must not only perform its original function but also have a structuring role. However, as one of the lowest parts in the engine, thermoplastic oil pans have some limitations and the most significant is their response to localised impact loadings such as that imparted by roadway debris or when dropped to the floor in a workshop [34]. A failure on the oil pan base wall would lead to engine oil leakage and that would result in a catastrophic engine failure from oil starvation. Therefore this thesis attempts to assess and improve the impact performance of thermoplastic polyamide oil pans subjected to localised low velocity impacts by means of experimentations and finite element simulations.

The aims of this research study are:

- To develop an improved understanding of the performance of an existing plastic oil pan considering material grade and geometry changes for improved impact performance and low weight.

The objectives of this thesis are:

- To explore and study the mechanical properties of different grades of SGFR PA66 in quasi-static and dynamic failure modes and also assess how they can be affected by changing conditions (such as variation of

temperature) and treatments (such as materials exposed to moisture and rock salt),

- To perform impact testing on oil pan samples using a drop weight tower and a gas gun impact tester. The investigations are focused on the structural integrity of the oil pan and the assessment of the damage,
- To create a validated model for the simulations with LS-Dyna,
- To use the model to predict impact consequences and also help to make decisions regarding improved design features whilst minimising stress concentration zones on the part.

1.3. Purpose of thesis

The purpose of this thesis is to study the structural integrity of a wet engine oil pan during its functional life in the vehicle. This involves benchmarking potential substituent materials through a material selection process, design feature improvement and assessing potential external influencing parameters on impact performance such as exposure to temperature, moisture and salt but also oil and air oxidation.

It follows that during storage, installation, maintenance and when in use, the oil pan experienced structural loads such as drop impacts to the floor whilst supporting the all engine unit or small debris impacts from the

roads like stones [34; 35]. With the material replacement operated and with all the changes that imply, the end result is to make sure that the thermoplastic oil pan continues to function reliably and remains free of leaks for the lifetime of the vehicle in normal usage conditions.

This thesis presents and discusses the experimental results from impact testing and assesses damages on the part structure. It is also a feasibility study for developing a finite element simulation approach of the problem. The first undertaken action was to review and evaluate the pre-existing under-the-hood thermoplastic components to determine key parameters involved, ways of investigation, weaknesses and limitations already identified concerning designs and polyamide grades used for oil pan applications.

1.4. Methodology

The study is focused on assessing the mechanical properties of two polyamide 66 grades subjected to localised impacts at low velocity range. Single impact scenario is considered in this research, as impact studies of composite polymers are inherently complex to comprehend [11; 36; 37]. Multiple impact scenario involves taking consideration of potential pre-

existing failure or damage in the material and in the component structure which increases even more the complexity [38-40].

Figure 2 presents the gap in current knowledge that is covered in this research. On one hand, there is the composite material configuration that includes matrix properties, filler properties and parameters (such as fibres weight content ratio, shape, size, and the quality of dispersion) and it also may include additives. This material configuration directly determines the mechanical properties and behaviour of the final material which can be experimentally measured and used in the simulations with an appropriate material card. On the other hand, the component is associated to its structural behaviour which results from its design and manufacturing process that directly defines its impact resistance and failure modes. The structural behaviour can also be assessed with the right experiments. However what is not well known is how to correctly link structural behaviour to material mechanical properties.

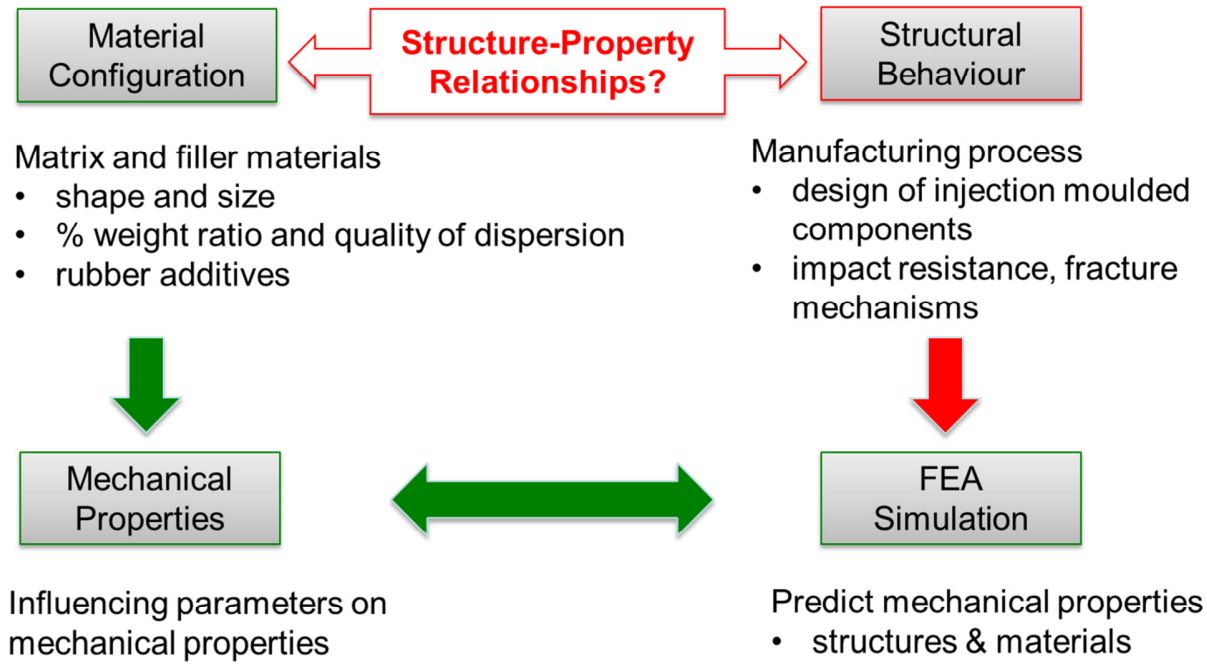

Figure 2 - Gap in current knowledge

The study extends the research by finding out the potential influence of critical parameters on material impact strength. These parameters are the influence of water and aqueous calcium chloride uptake, and the variation of temperature. The results from finite element simulation analysis are compared with experimental data and vice versa. The design of the final oil pan component evolves as the study progresses. This study leads to make some proposals for improving current prototypes and also identify other possible applications or applicable services for future work. A concept of knowledge transfer was also conceived.

1.5. Outline of the thesis

Chapter 1 attempts to acquaint the reader with the subject of the thesis by giving relevant background information and defining aims, objectives and the thesis plan. Key interest is on structural properties relationship of polyamide composites subjected to localised impact. Typical application is presented to stress the importance of the current work in the automotive industry.

Chapter 2 prescribes a literature review of the existing work and knowledge by presenting the current state-of-the-art of polyamides and associated glass fibre reinforced composites. Factors affecting the mechanical properties of polyamides are described from a material point of view and from those associated during their processing to external factors influencing their impact performance. An insight to the current work in finite element analysis of short glass fibre thermoplastics is also given. Overviews of current polyamides in under-the-hood applications and assembly techniques are presented. Finally, key findings of the literature review are drawn.

Chapter 3 assesses the mechanical properties and impact performance of two 35 wt% of SGFR PA66 with one material being rubber toughened PA66 in quasi-static and dynamic loads, respectively named PA66-GF35 and

PA66-i-GF35. This study emphasises the effect of the rubber additive and demonstrates its capacity to toughen the polyamide composite.

Chapter 4 investigates the influence of moisture and aqueous calcium chloride uptakes on the mechanical properties and impact performance of PA66-GF35 and PA66-i-GF35 in quasi-static and dynamic loads. This study inspects the consequences of exposure to moisture and salt conditions that can be faced by under-the-hood thermoplastics components.

Chapter 5 investigates the influence of the temperature on the mechanical properties and impact performance of PA66-GF35 and PA66-i-GF35. Thermal ageing in hot oil and hot air were conducted. Examinations were performed to point out the effect of the rubber additive on the thermal properties of polyamides. This chapter also looks at the behaviour of each material whilst being affected to temperatures in the range between -20 and 120°C.

Chapter 6 examines the influence of structural configurations as a protective feature design and assesses the effect of elongated structure associated to the properties of SGFR PA66s. This study emphasises the important role of the design in terms of impact performance and stress distribution.

Chapter 7 covers the low velocity localised impact testing of SGFR PA66s oil pans and describes the progression to a superior design

configuration associated to a superior impact resistant material. Damage and fracture examinations are covered and impact simulations on the oil pan were also conducted.

Chapter 8 concludes the thesis work, summarising the current understanding of SGFR PA66s in terms of structural and mechanical performances. This research project contributed in the improvement of a thermoplastic composite oil pan but has been beneficial to other under-the-hood components at their early stage of development. Further investigations and improvements are also suggested.

Chapter 2. Literature review

2.1. Introduction

Polyamide, also referred to as nylon, is a semi-crystalline polymer. This material offers an excellent combination of mechanical and electrical properties coupled with good resistance to heat and chemicals [41]. It has high lubricity and moderate strength [42; 43]. It is tough, inexpensive, but has poor dimensional stability due to water absorption [44; 45]. However, whilst they are tough under many impact conditions they tend to be notch sensitive and brittle at low temperatures, so needing modification by the use of various additives [7].

A number of different types of polyamide are available covering a wide range of properties. The most abundant polyamides used in the automotive industry are PA6 and PA66 for their superior heat ageing resistance, good resistance to wearing and good surface finish [4; 46]. PA6 is made by hydrolytic polymerisation of caprolactam. PA66 is made by the polycondensation of hexamethylenediamine and adipic acid. Figure 3 shows the monomers of PA6 and PA66. Dhevi et al. [47] indicated that their good combination of strength, toughness, wear, abrasion and chemical resistance

is attributed to the amide group (-CO-NH-) that provides H-bonding between polyamide chains. Polyamides fall into two groups [28]:

- Those synthesised from one repeating monomer are given a single number in their name, the number of carbon atoms in the monomer unit (e.g. PA6).
- Those synthesised from two different repeating monomers are given two numbers in their name, indicating the number of carbon atoms in each monomer unit (e.g. PA66).

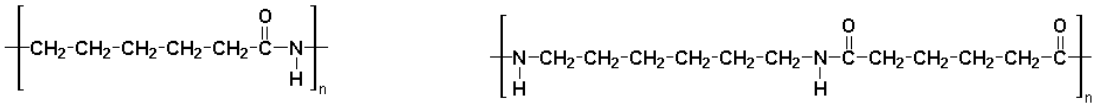

Polyamide 6 Polyamide 66

Figure 3 - Monomers of PA6 and PA66

Table 1 provides the properties of unreinforced and SGFR PA6 and PA66 materials [48; 49]. PA66 has good melting point, and high strength and stiffness. After moulding it absorbs water, causing swelling and increased toughness. It can be modified by glass fibres and by nucleating agents giving rapid crystallisation. It resists most solvents except strong acids or oxidising agents. Outdoor exposure causes colour fading and embrittlement unless the resin is stabilised. Glass fibre reinforced PA66 is as

tough as most amorphous plastics and resists stress cracking or solvent attack, retaining high fatigue and impact resistance. The properties of PA6 are generally similar to those of PA66 but PA6 has a lower melting point, absorbs more water and has less resistance to mineral acids. It has rather higher tensile and impact strength and lower elongation at break. The main advantage of PA6 over PA66 is that it is easier to process and produces lower mould shrinkage. The main disadvantage of PA6 is that it has lower strength, stiffness and abrasion resistance than PA66 and higher water absorption. The main advantages of PA66 are its better low temperature toughness than PA6 and its good fatigue resistance [7; 28].

Table 1 - Properties of unreinforced and SGFR PA6 and PA66

Properties	PA6	PA6-GF35	PA66	PA66-GF35
Physical Properties				
Density (g/cm^3)	1.12	1.40	1.13	1.41
Moisture Absorption at Equilibrium (%)	2.43	1.69	2.39	1.62
Mechanical Properties				
Tensile Strength Ultimate (MPa)	63.5	140	70.3	125
Elongation at Break (%)	85.3	3.5	70.4	3.82
Tensile Modulus (GPa)	2.19	11.40	2.46	11.20
Poisson Ratio	0.35	0.350	0.407	0.380
Charpy Impact (Un)Notched (J/cm^2)	(13.3) 2.34	(9.33) 1.52	(11.8) 1.45	(10.0) 1.75
Thermal Properties				
Melting Point (°C)	219	219	258	258
Service Air Temperature (°C)	[-31; 115]	[-21; 136]	[-30; 132]	[-20; 148]
Processing Properties				
Processing Temperature (°C)	241	249	276	282
Moulding shrinkage (%)	1.31	0.35	1.41	0.50
Injection Pressure (MPa)	85.3	78.4	84.1	76.5

2.2. Factors affecting mechanical properties

2.2.1. Influence of fibre length, diameter and concentration

The mechanical performance of glass fibre reinforced polyamides results from a combination of the fibre and the matrix interface. The fibre content, diameter, orientation and the interfacial strength are key factors to the final balance of properties exhibited by injection moulded thermoplastic composites [50-55].

Bernasconi et al. [56] studied the fibre length distribution on PA6 with 10-20-30 wt% of glass fibres and noticed that fibres are shorter (473-354-276 μm) as the fibre content increases presumably because of fibre breaking during injection moulding process. Hassan et al. [55] also observed the fibre length degradation. From the initial length of 3-6 mm before compounding they found an average fibre length in the injection moulded part in the range of 0.2-0.4 mm. When compared to long glass fibres, short glass fibres have statistically more total fibre length (56%) and more total fibre surface area (33%), which is an advantage in terms of interfacial bonding to the matrix. However, the tensile strength and modulus of long glass fibres reinforced PA66 are superior (20-30%) to those of short glass reinforced PA66 meaning that the length of the individual fibre itself is also a determining parameter

of the composite properties. On the other hand, the fracture strain of long fibre composite is found 20% lower than the short fibre composite and that is believed to be due to the existence of longer fibre that restricts the matrix movement. Curtis et al. [42] also described this reduction of fracture strain associated with a longer fibre and higher fibre volume fraction. In terms of fracture energy and peak load, Hassan et al. [55] found that they are increased with the increase in fibre volume ratio and fibre length.

The effect of fibre diameter and fibre diameter distribution is also an influencing parameter on the performance of glass reinforced polyamides. Sato et al. [51] studied the mechanical properties of injection moulded polyamides with 30 wt% of glass fibre. In the 7-13 μm diameter range, they found that the tensile and flexural strength are low dependent on fibre diameter but below 7 μm, strengths drastically fall. Thomason [57] reported a study on the 9-18 μm range on glass fibre reinforced PA66. He found that the unnotched impact and tensile strength decreased significantly but the tensile modulus presented no dependency over the range. The notched impact varied less but showed a maximum at 14 μm. Over the range studied, the fibre diameter is little significant on fibre orientation. Ramstein et al. [58] investigated the fibre diameter range of 10-24 μm and found significant dependence of unnotched Charpy impact and tensile strength on the fibre diameter but slight effect on tensile modulus and notched Charpy impact.

Thomason [59-61] did extensive studies on the effect of fibre content (0-40 wt% range) on short glass (4 mm length, diameter 10 μm) reinforced PA66. He noticed that the stiffness and strengths in tension and flexion increases almost linearly with increasing fibre concentration. Tensile modulus evolved from 3 to 12 GPa, tensile strength from 70 to 170 MPa and flexural strength from 120 to 330 MPa over the full range of fibre content studied. He also noticed that the tensile elongation drops (3.8-2.9%) with increasing fibre content in the 2-10 wt% range leading to a large reduction in the ductility of the material. From 10-30 wt% the elongation was approximately constant and then above 33% it started to fall again (below 2.8%). Thomason also found that the impact behaviour of PA66 is altered by the addition of fibres. On the notched Izod impact, the increase of fibre content has only beneficial effect above 10 wt%. However, it has severe effect on the unnotched Izod impact since the initial performance of the PA66 is very high and did not break. A small concentration of fibres leads to a sharp fall until 4 wt% and then above the impact resistance steadily rises.

2.2.2. Impact failure mechanism and capability of energy absorption

In composite materials, fracture behaviour is a complex mechanism. The mechanical properties of thermoplastic composites result from a combination of the fibre and matrix properties and the ability to transfer

stresses across the fibre / matrix interface [50; 62; 63]. Key factors such as interfacial adhesion, fibre length to diameter ratio and concentration, matrix ductility, and residual matrix stresses due to differences in thermal expansion between fibres and matrix during processing determine the composite fracture mechanisms [64-67]. Therefore, all of these parameters influence the load bearing capacity of the finished product.

In impact testing, Hassan et al. [55] noticed that longer fibres tend to break in more brittle manner by fibre breakage mechanism and contribute less fracture energy to the composite compared to shorter fibres that tend to break in more ductile manner by fibre pull-out mechanism and contribute more fracture energy to the composite.

Many studies in short fibre reinforced composites [11; 25; 32; 53; 67-70] agreed that fibres act both to initiate cracks and to inhibit crack propagation. On one hand, fibre discontinuities can be considered as structural flaws which initiates cracks, but on the other hand since cracks must often travel around fibres in the crack path, fibres act to inhibit crack propagation by increasing the volume in which energy dissipation can take place [71].

As previously found, composites with small diameter fibres have a large interfacial area between matrix and reinforcement. Since generally fibres are high in modulus and the matrix is low, the interfacial region is

subjected to high stresses during composite deformation. Blumentritt et al. [67] investigated and described fracture mechanisms in short fibre reinforced thermoplastics. They noticed that if fracture occurs at the interface, fibres are pulled out of the matrix with little or no matrix material adhering and very few fibres are found fractured. Matrix failure also results in fibres pull-out but they will be coated with the matrix material. If the matrix and interfacial strengths are high, fibre fracture becomes the predominant failure mode and only fibres with ends near the fracture surface are pulled out during fracture.

Since generally fibres are strong but brittle whilst matrices are weak but tough, fibre fractures are found in high strength composites with low toughness and conversely fibre pull-out are found in tough composites with low strength.

2.2.3. Processing by injection moulding

Polyamide can be processed by a lot of techniques such as using injection moulding, mono and multilayer injection, injection blow moulding, rotomoulding, extrusion blow moulding, mono or multilayer extrusion, thermoforming, thermoretraction, and so on. However, injection moulding is the most widely used process to produce automotive parts such as the oil pan thanks to the ease to form complex shapes and fine details with

excellent surface finish, good dimensional accuracy for high production rate and low cost [6; 28]. Most reinforced thermoplastics for under-the-hood applications are injection moulded in 30-35% SGFR PA6 or PA66 making parts up to 50% lighter than their metal counterparts and contribute to improved engine efficiency and better emissions [72; 73].

The process cycle of injection moulding consists of four stages: clamping, injection, cooling and ejection. The cycle begins when the clamping unit closes the mould halves together. Next, the granulated PA66 is melted with chopped glass fibres by heat between 280-300°C (above its melt temperature of 260°C) and pressure around 100 bars. The molten plastic is then injected thanks to a screw at 200-300 mm/s into the mould cavity (mould temperature 80-90°C). When the mould is filled, a holding pressure is maintained to compensate for the volumetric contraction occurring (shrinkage 0.5%) on solidification and subsequent cooling. After cooling, the part is ejected from the mould [74].

It is important to note that the processing of glass fibres in injection moulded composites leads to large reductions in the fibre length as observed by [55; 75; 76]. Thomason [61] measured a reduction from the initial 4 mm fibres to less than 0.7 mm caused by the compounding and moulding process. He noted that the increase of fibres concentration above 10 wt% reduces linearly the average length of fibres. He attributed this fact by the

increased probability of fibre to fibre and fibre to machine interaction and an increased apparent melt viscosity resulting in higher bending forces on fibres during compounding and moulding. This can explain why the strength based properties show a decreasing reinforcing effect as the fibre concentration is increased.

Russell et al. [77-79] inspected the structure and properties of injection moulded PA66 and recognised a morphology type skin-core. They noticed that the core was composed with spherulites of average diameter of 6 μm. They found that the skin thickness was dependent and affected with the increase in mould temperature. The increase of the mould temperature augments the crystallinity of PA66 in the skin which increase yield strength but reduce toughness.

Apichartpattanasiri et al. [80] investigated the tribological behaviour of PA66 with varying injection moulding parameters. By increasing the mould temperature, they obtained different microstructures in the core with increasing average spherulite size.

Paterson et al. [81; 82] examined the effects of absorbed water on residual stresses and distortion on injection moulded PA66. For low water absorption in the normal stress distribution, they found compressive stresses at the surface and tensile stresses in the interior. For high water absorption, water causes increase of crystallisation in the skin and therefore relative

volume change and residual stresses between skin and core but however with increased toughness. Furthermore, they noticed that uneven water absorption creates distortions and changes in residual stresses.

2.3. Impact performance of polyamides

2.3.1. Effect of specimen configuration and impact methods

The measurement of the impact resistance of thermoplastic composites often depends on the parameters of the test as much as the structure–performance relationships of the material under test. Thomason [61] estimates that a major discriminating factor is whether or not the sample under test has been notched. From a structure–performance point of view, he found that composite impact strength appears to be influenced by all of the same parameters as tensile strength but to different levels. Notched impact data will mostly reflect the energy required to propagate an existing crack through the sample, whereas unnotched impact data will depend on both initiation and propagation energies.

De Monte et al. [83] highlighted that the specimen thickness in thermoplastics affected mechanical properties as the thinner the specimen is the higher is the degree of anisotropy. Hassan et al. [31] reported wide discrepancies on impact properties of PA6 composites (even if the same

polyamide grade was used) whilst assessing three testing parameters using Charpy and drop weight impact testers. They concluded that impact properties such as fracture energy, peal load, critical strain energy and critical stress intensity are largely dependent on the testing conditions such as specimen size / geometry, impactor tip velocity / mass.

As the use of thermoplastics in the automotive industry increases, the need to determine their impact responses to ensure safety and stability of designed structures is important. The impact test fixture should be ideally designed to simulate the loading conditions to which the composite component is subjected in operational service and then reproduce the failure modes and mechanisms likely to occur in real conditions.

Most efforts in understanding the impact performance and failure mechanisms of reinforced thermoplastics were principally concentrated on Charpy and Izod impact testing, and to a lesser extent, drop weight tower impact testing [12; 71; 84; 85]. These tests can yield information on the processes of energy absorption and dissipation within composites [17]. Charpy and Izod are usually destructive and therefore induce failure modes that are not necessarily observed under real conditions on operational structures. They force the specimen to fail at a predetermined area rather than along the weakest plane. The results can be skewed because of the highly anisotropic nature of reinforced thermoplastics. Consequently, these

tests are only suitable for comparing impact resistance of composite materials.

A more representative test to simulate the effect of stones would be in the low velocity range with a blunt tip impactor or projectile. This can be achieved with a gas gun or to a certain extent with a low velocity drop weight tower [12; 17]. In a low velocity drop weight tower, the impact energy and velocity can be varied by changing the mass and height of the dropping weight to where the impactor is attached. The low velocity gas gun impact test gives a more representative test of a stone impact scenario and can be used to test large structures in different angles. It is a single stage high performance projector using compressed air to propel projectiles with various profiles and masses [86]. These tests are not necessarily destructive but can often results in large-scale damage.

2.3.2. Effect of rubber in toughened polyamides

Semi-crystalline engineering thermoplastics such as composite polyamides are pseudo-ductile [87; 88], which means that they have a much higher crack initiation resistance than crack propagation resistance due to the fact that they are notch-sensitive materials. In order to improve their toughness and impact strength especially at low temperature, an elastomeric/rubbery phase is incorporated and dispersed into the matrix

[89]. Under impact loading, the elastomeric regions absorb additional energy and prevent brittle fracture. The role of the rubbery particles is simply to induce yielding processes in the matrix [90]. In principle, the glass fibre reinforced rubber toughened polyamide formed has a good balance of stiffness, strength and toughness.

Different types of rubbers have been successfully used for thermoplastics toughening such as styrene ethylene / butylene styrene (SEBS), ethylene propylene diene monomer (EPDM), ethylene propylene rubber (EPR) and styrene butadiene rubber SBR but most rubbers do not show necessary compatibility with polyamides and cannot correctly disperse in rubber [91-94].

Laura et al. [95] studied the effect of glass fibre and maleated EPR content on tensile and impact properties of PA6. She reported that the incorporation of the rubber into PA6 reduces modulus and yield strength but can be completely reversed by addition of glass fibres providing stiffness and strength. The Izod impact energy of the glass fibre reinforced rubber-toughened PA6 is improved comparatively to the material containing no rubber.

The selection of an elastomer with appropriate mechanical properties is also critical to blend performance. Dermanaki Farahani et al. [91] investigated the mechanical properties of PA66 and toughened PA66 with 20

wt% SEBS triblock copolymers grafted (g) with different levels of maleic anhydride (MA), PA66/SEBS-g-MA. Impact and tensile tests results showed that 20% rubber toughened PA66 exhibits significantly more impact strength (15 times) and elongation at break compared to the polyamide alone. Huang et al. [96] also investigated rubber toughened PA6 and PA66 with SEBS-g-MA, they found that the ductile-to-brittle temperature transition decreased with increased rubber content and decreased rubber particle size.

Indeed, maleated rubbers are high interest for impact modification, Laura et al. [89] reported that during melt processing, the maleic anhydride grafted to the elastomer rapidly reacts with the amine end groups of the polyamide to give graft copolymers that simultaneously improve interfacial adhesion, reduce rubber particle size, and stabilise blend morphology. Huang et al. [96] reported that the nature of the rubber, the matrix, the morphology of the dispersed phase (rubber particle size and distribution) and the rubber content as well as the processing conditions play an important role in determining the level of toughening of polyamides.

2.3.3. Effect of water absorption and hydrolysis ageing

Akay [97] investigated the moisture absorption and its influence on tensile properties of glass fibre reinforced PA66 and found that the equilibrium amounts of moisture absorbed is proportional to the weight

fraction of the polymer but also varies with sample preparation and microstructure. The moisture uptake of the injection moulded composites was found significantly different to those with machined edges. Akay [97] and Valentin et al. [44] observed a sharp deterioration of the tensile strength for glass fibre reinforced PA66 and PA66 at respectively 1.5 wt% and 3 wt% moisture contents. Moisture uptake resulted in increased elongation to failure for PA66 but practically no variation in the elongation behaviour for the glass fibre reinforced PA66.

More than a simple moisture diffusion, Camino et al. [98] witnessed three different mechanisms within the material: the hydrolysis of the macromolecular chains into low molecular weight chains; the hydrophilisation with matrices that swell and plasticise; and the interfacial decohesion inducing a degradation of the composite.

Bergeret et al. [99] studied the stress-strain response of PA66 and found that this relation strongly depended on the humidity conditions. They considered PA66 as dry when the hygrometry is less than 0.2% and saturated at 7.2% and observed that the tensile strength in dry condition in glass fibre reinforced PA66 is twice higher than when saturated.

Thomason [59] observed the plasticising effect of water on PA66 and its composites significantly reduces their performance (tensile modulus respectively reduced by 80-45% and strength by 45-50%) over a range of

0-40 wt% of glass fibres. The tensile elongation showed a large increase particularly at low fibre content. Thomason also assessed the hydrolysis ageing effect after 200, 500 and 1000 hours of water-glycol treatment at 120°C. He found that all conditioned samples behaved similarly and showed a significant low tensile modulus and strength compared with dried samples. However, the 1000 hours water-glycol treatment had a slightly higher tensile modulus and lower strength compared to the other conditioned samples. The conditioning causes a high level of plasticisation of the polyamide matrix.

2.3.4. Effect of aqueous salt solutions

Polyamides used in under-the-hood components undergo deterioration in their mechanical properties when exposed to salt splash used on roads to melt ice during the winter [100; 101].

Kim et al. [102] and Hong et al. [103] observed the degradation of PA66 under repeated contact with aqueous calcium chloride / ethylene glycol solutions (aq. $CaCl_2$/EG), which led to stress cracking. Hattori et al. [104; 105] characterised PA66 dissolved in a mixture of calcium chloride / methanol ($CaCl_2$/Me) and observed the formation of a complex with PA66.

Wyzgoski et al. investigated the stress-rupture behaviour [106], polyamide-salt interactions [107] and craze-growth kinetics [108] in aq. $CaCl_2$ treated PA66 and proposed a plasticisation mechanism for the salt-

induced crazing of crystalline PA66. Xiong et al. [109] examined the complexation mechanism of PA6/$CaCl_2$ and explained the reaction between the amide group and the $CaCl_2$. They proposed that calcium cations coordinate with the oxygen atom of the carbonyl group, which weakens the hydrogen bonding between the molecular chains of PA6 and releases the free N-H group, so that the N-H group can coordinate with chloride anions to form the hydrogen bonding. They found that there was no complexation between calcium cations and the nitrogen atom.

Dhevi et al. [47] investigated the deterioration in mechanical properties of PA66 and glass fibre (30 wt%) reinforced PA66 by aq. $CaCl_2$ mixture solutions. As Xiong et al. [109] but on PA66, they noticed that aq. $CaCl_2$ treated PA66 was not significantly degraded and physical changes involved H-bond breakage and the coordination of calcium cations with the oxygen atom of the carbonyl group of the amide linkage. The absorbed $CaCl_2$ modified the melting and recrystallization of PA66. However, they found that the mechanical properties of aq. $CaCl_2$ treated glass fibre reinforced PA66 exhibited pronounced degradation, which they have associated to the interfacial failure between glass fibre and PA66 matrix.

2.3.5. Effect of temperature

Polyamides are recognised to be temperature dependent with the increase of temperature reducing both the Young's modulus and tensile strength but increasing the failure strain leading to a material more ductile and less stiff [5; 64]. Lhymn et al. [43] and Chevali et al. [110] noted that the temperature could increase the moisture absorption in the material. Eriksson et al. [41] and Rudzinski et al. [111] examined the effect of thermal ageing on unreinforced and glass reinforced polyamide 66 and reported that thermal ageing causes oxidative degradation on the surface region resulting in a decreased elongation at break and embrittlement of the material.

Mouhmid et al. [64] studied the mechanical behaviour of 0-50 wt% glass fibre reinforced PA66 and the effect of the temperature on tensile properties. They noted that the tensile behaviour was strongly dependent on the temperature. In the range of 20-80°C studied, the increase of temperature decreases the normalised Young's modulus following a non-linear relationship whereas the normalised tensile strength also decreases but almost linearly. They also noted that the failure strain increases as the temperature is increased in the range of 5-8% for the reinforced PA66. However, the effect of temperature on the failure strain of the unreinforced PA66 is much more pronounced (12-63%).

De Monte et al. [83] investigated the influence of temperature on the anisotropic properties of SGFR PA66 under tension-tension and tension-compression cyclic loading (constant load at frequency range 5-10 Hz). They noticed that the temperature affects only the ductility of the matrix and has no effect on the material anisotropy. The temperature strongly reduces the fatigue strength under cyclic loading, especially at around 130°C. They observed the temperature distribution and discerned local overheating nearby the shoulder area of the specimen. After 6400 cycles at 10 Hz and 90°C of a 3 mm thick specimen, the temperature differences were up to 20°C between the central and shoulder area. Temperature shortened fatigue life and failure was of thermal rather than mechanical.

Sonsino et al. [112] also perceived the self-heating phenomenon whilst investigating fatigue design of highly loaded SGFR PA66. High temperatures reduced the fatigue strength considerably which diminished fatigue life (80-130°C). With the increase of temperature, the notch sensitivity of PA66 practically disappeared due to the softening of the material.

Thomason [59] assessed the elevated performance of SGFR PA66. He observed that between 0-10 wt% of fibres the deflection temperature under load is raised from 75°C to 245°C. Above 10 wt% of fibres, the temperature slowly increases until it reaches the melting point of PA66 (around 265°C).

Thomason [61] also investigated the impact performance of PA66 and glass fibre reinforced PA66 in the range from -40 to 80°C. A notched Charpy impact at 80°C increases the performance of both materials in comparison to room temperature (23°C) results and particularly for PA66 due to testing above its glass transition temperature (range of 50-75°C). However at -40°C, both materials drop in performance and significantly more for PA66. The notched impact resistance of PA66 from 80 to -40°C reduced by 80% associated to its ductile-brittle transition temperature. This clearly shows that additional energy dissipation mechanisms are activated thanks to the addition of fibres. The loss in impact resistance across the same temperature range was reduced to only 40% for the SGFR PA66.

2.4. Finite element analysis on short glass fibre thermoplastics

As a composite material, the macroscopic behaviour of injection moulded SGFR thermoplastic results from interactions between the highly non-linear thermoplastic matrix and elastic short fibres.

To simulate the macroscopic mechanical response, some authors proposed a micro-modelling method to describe the fibre orientation [113-116] but encounter complications to describe the overall mechanical behaviour. However, Dray et al. [46] and Vincent et al. [113] observed in

their approach the anisotropic distribution with fibres parallel to the injection flow in the composite skin and perpendicular in the composite core.

To overcome the complexity of fibres distribution, several other authors proposed to homogenise the mechanical behaviour of the matrix and short fibres; Doghri et al. [117; 118] and Mlekusch et al. [119] studied elasto-plastic materials; Pierard et al. [120] looked into elasto-visco-plastic composites. These approaches can handle complex interactions between fibres and matrix such as damage, interfacial debonding and so on. However, they require much data to be efficiently used [121-124].

Zhou et al. [125] described a non-linear elasto-plastic model based on the stress-strain relationship for the tensile behaviour of PA66 with 33 wt% of glass fibres using the tensile modulus and a Weibull continuous probability distribution with a Weibull shape parameter, and a Weibull scale parameter as a linear logarithm function of strain rate. In the range of 0.05-5 mm/min, they noticed that the failure strain was not affected by the strain rate but only the tensile modulus and tensile strength.

Lobo [126] also proposed a stress-strain relationship to describe the non-linear behaviour and tried to implement it into LS-DYNA using MAT24 for modelling crash and drop impacts [127]. Despite the fact that thermoplastics do not exhibit a clear yield transition, he decomposed the stress-strain curve between an initial linearity up to a chosen yield point and

beyond the stress-strain curve is described as an effective stress-plastic strain curve up to the failure strain. However, the accuracy of the model on the stiffness depends on the choice of the modulus.

2.5. Joint assembly by vibration welding

Sometimes, further processing techniques are required after injection moulding. In an oil pan module, the integration of functional parts such as the pick-up oil pipe cover is required. In composites structures, assemblies can be mechanically fastened (bolts, rivets and pins) [128], bonded with adhesive joints [129] or welded [130].

For mass volume production of automotive parts, welding is the preferred process as it is a robust method to produce cost effective high strength and pressure tight seals with a joint strength approaching that of the parent material [7; 46; 131]. Welding techniques allow to physical join thermoplastics to fabricate complex hollow assemblies from simpler injection moulded semi-finished parts. Polyamides can be welded by all the processes normally employed for thermoplastics such as vibration, laser, hot plate or IR welding [132].

Amongst all of the welding techniques, the vibration welding offers advantages in relation to speed (2-3 seconds), final appearance and most importantly bond strength even on complex irregular shape [133]. The

vibration welding is based on friction welding in where the heat required to melt the plastic is generated by pressing one part against another and vibrating it through a small relative displacement or amplitude in the plane of the joint. One of the two halves is kept stationary whilst the other moves. Amplitudes range from 0.7-1.8 mm at 240 Hz (high frequency) and 2.0-4.0 mm at 100 Hz (low frequency). When vibrations stop, parts are aligned, the weld cools down and solidifies [133; 134]. Hatcher et al. [135] and Pathan et al. [136] pointed out in their studies that components should be dry prior to welding since excessive moisture can reduce the strength of the bond. Moreover, vibrations and high welding pressure can cause stress and grainy weld flash and wide seam can be observed as well. However, the vibration welding has relatively short cycle times and makes high strength bonds.

2.6. Polyamides for under-the-hood applications

The automotive sector is the biggest market for polyamides. Early applications included gears, windshield wiper components, wiring clips, bearings and switch housings. Table 2 shows the main automotive applications of glass fibre reinforced polyamides. With the introduction of glass fibre reinforced polyamides, main applications are now under-the-hood applications such as the air intake manifold, the air and cooling systems, the throttle body housing, the cylinder head cover, the acoustic cover, the oil

pump, the oil pan and mounting elements for the air duct cover on an oil pan. Table 3 presents some examples of composite polyamides under-the-hood components and their principal characteristics and advantages.

Table 2 – Glass fibre reinforced polyamide grades used for automotive applications [137]

Grades	Features	Processing Method	Example of use
PA66-GF35	Heat stabilised, high stiffness, oil resistant, hydrolysis resistant, good heat-ageing resistance, good flow	Injection moulding or blow moulding	Air inlet manifolds, oil pans, cylinder head covers, solenoid valve housings, cable attachments, electrical insulating parts
PA6-GF35	Heat stabilised, oil resistant, good heat-ageing resistance, good flow	Injection moulding	Manifolds, pedals, oil pans, exterior body panels, external door handle, fan

Table 3 - PA6 and PA66 usage for under-the-hood applications [73; 137; 138]

Under-the-Hood Products	PA Grades	GF content (%)	Characteristics over counterparts
Engine Covers	PA6	20-30%	Surface finish, heat resistance, stiffness, low warpage
Air Intake Manifolds	PA6 PA66	30-35%	Up to -30% cost production/metals, up to -50% weight/metals, parts integration
Rocker Covers	PA6 PA66	30-35%	Weight reduction and flexibility of design over aluminium and thermosets
Heating and Cooling Systems	PA66	30-35%	Heat stability, high stiffness, low warpage, corrosion resistance, weight reduction over metals
Oil Pan Reservoir	PA6 PA66	30-35% >35%	Weight and cost savings over metals, noise reduction, increased capacity, enables additional module content

PA66 and PA6 account for most automotive applications of polyamides. The balance between PA66 and PA6 varies with the application. In under-the-hood uses, PA66 accounts for almost 80% [7; 28; 46]. New components made of thermoplastics are still finding applications in under-the-hood. The substitution of metals to thermoplastics allows new design of very complex parts consisting of assemblies of many components that could not be designed using metals. The weight saving by integrating several functional components in one plastic part is the driving force for a further substitution of traditional materials by thermoplastics [46; 72].

Table 4 presents some properties of commercial polyamide materials and illustrates that within the same polyamide polymer and glass fibre content the properties differ depending on each material brand.

Table 4 - Properties of commercial polyamide materials for oil pan [137; 138]

Properties (dry)	DuPont PA66-GF35	Lanxess PA66-GF35	BASF PA66-GF35	Lanxess PA6-GF60	BASF PA6-GF35
Tensile Modulus (GPa)	11	10,6	11,2	18,9	10
Stress at Break (MPa)	210	200	200	235	170
Strain at Break (%)	3	3,1	3	2,1	3,5
Charpy impact strength +23/-30°C (kJ/m^2)	80/80	80/70	95/75	90/90	102/113
Charpy notched impact strength +23/-30°C (kJ/m^2)	15/10	12/10	13/12	-/-	26/18
Melting Temperature (10 °C/min) (°C)	260	263	260	-	220
Water Absorption (%)	5,5	5	5	5	-
Humidity Absorption (%)	1,7	1,7	1,6	1,5	1,1
Density (kg/m^3)	1410	1410	1410	1570	1360

2.7. Key findings of the literature review

The review of the literature shows that there is a trend in the automotive industry towards more use of composite materials over metals. Amongst those materials, SGFR PA6 and PA66 are appreciated for their overall properties.

Glass fibres characteristics associated with the matrix have a significant influence on properties of the final material. The addition of glass fibre in the matrix causes a loss of ductility and a greater stiffness. Therefore, tensile strength and modulus are augmented and failure strain is reduced. Long fibres have superior mechanical properties over short fibres but break in a brittle manner. Short fibres have more interfacial bonding with the matrix and allow more ductility in the material. Fibres are crack initiators in the composite but at the same time inhibit its propagation by increasing the volume in which energy dissipation can take place. With fibres content above 10 wt% the elongation is improved constantly up to 30-40 %wt. Fibre diameter is found less significant than fibre length and fibre concentration. Composite materials are predominantly processed by injection moulding. However, the injection moulding process reduces significantly fibre length (up to 80%). Injection moulding creates skin-core morphology, with fibres in the skin following the direction of the injection flow and agglomerate of spherulites in the core. Stresses are found in the

skin-core morphology. Water uptake can amplify residual stresses and distortion in the structure. The temperature of the mould is also an important parameter determining the skin thickness and the crystallinity of the matrix.

Impact performance varies with specimen configurations and impact test methods. Specimen thickness in thermoplastics affects mechanical properties responses. The thinner the higher is the degree of anisotropy. There are discrepancies on composite impact properties which largely depend on testing conditions. Notched impact data reflects the energy required to propagate an existing crack, whereas unnotched impact data depends on both initiation and propagation energies. Polyamides are notch-sensitive materials. Incorporating and dispersing an elastomeric/rubbery phase into the matrix can improve their toughness and impact strength. The rubber improves the elongation at break and impact resistance especially at low temperature. Indeed, the increase of rubber decreases the ductile-to-brittle temperature transition. However, the addition of rubber reduces tensile modulus and yield strength. Water and aqueous salt uptakes are significant affecting parameters with deterioration of strength and reduction of impact performance. Water plasticises the matrix resulting in an increased elongation to failure. Aqueous salt can cause stress cracking and interfacial failure. The temperature is also a very significant parameter with the increase of temperature leading to more ductility and less stiffness. Thermal

ageing can cause oxidative degradation resulting in a decreased elongation at break and embrittlement of the material. Impact simulation depends on the scale investigated, the structure and the type of solicitation. At macroscopic scale, short glass fibres and polyamide matrix can be approximated as the behaviour of a single material. Impact simulation of composite material can be performed if the model comprehends the non-linear behaviour of the matrix associated with the elastic behaviour of the fibres. Finally, identical commercial materials (matrix and fibre content) were found with different mechanical properties meaning that manufacturing processing parameters and materials compositions are different.

In order to comprehend the impact performance of SGFR PA66, initial investigations should determine their mechanical properties over a range of stresses and assess the influence and consequences of environmental conditions. Structure-property should also be investigated using experiments and simulations so as to understand their relationship and as a final point improve material and structure on a component.

Chapter 3. The influence of rubber modifier on impact resistance of short glass fibre reinforced polyamide 66s

3.1. Introduction

PA66 is extensively used in engineering applications thanks to its excellent mechanical properties and it has a good combination of high strength and ductility [139-141]. However it is acknowledged that when PA66 is loaded in the presence of a high stress concentration area, such as a notch for instance, the resistance to failure of the material can be seriously reduced in relatively low fracture toughness [142-144]. The use of thermoplastics reinforced with short glass fibres increases both stiffness and strength, but these improvements are accompanied by a reduction of the ultimate strain [42; 145-148].

In automotive under-the-hood components subjected to loadings or impacts, this brittle behaviour is unwelcomed. In recent times, the toughening of thermoplastics with a rubbery phase has been promising to prevent such brittle failure, producing strong, tough and impact resistant materials [68; 87; 149-155]. However, such inclusions often reduce the modulus, stiffness and strength, which are important for material performance [156-158]. The combination of reinforcement with rubber toughening phase may be a solution to balance the end use performance

[89; 95; 159; 160]. In the literature, impact modified polyamide 6/polypropylene blends were investigated in terms of the morphology-property relationship with maleated rubbers. It emerges that they are found to be good impact modifiers for room temperature toughening [93; 161-163]. However, the understanding of such materials is a relatively unexplored area.

This chapter therefore studied the influence and effect of a rubber modifier on the mechanical properties of SGFR PA66s under quasi-static and dynamic loadings.

3.2. Experimental testing

3.2.1. Materials and specimens preparation

Two commercial grades of polyamide 66 with 35 wt% of discontinuous glass fibre, Ultramid A3HG7 (SGFR PA66) and Ultramid A3ZG7 (rubber toughened SGFR PA66) were manufactured by Basf (data sheets available in Appendix 1 and Appendix 2). The rubber modifier in the rubber toughened material has been intimately melt-blended into the base material. The nature and amount of rubber information was not accessible from the material producer but previous studies have shown that one of the most promising types of elastomers used as toughening agents for polyamides are

EPR copolymers in addition of about 20 wt% in the form of small particles [3; 149; 151; 153; 164; 165]. The polyamides are copolymerised with the EPR chains on the terminal amine groups of the polyamide. The graft copolymers produced aids dispersion, creating separate phases in the solid enhancing interfacial adhesion.

The glass fibres have an average length (l) of 300 μm and diameter (d) of 13 μm, thus yielding an average aspect ratio (l/d) of 23. The materials are initially extrusion compounded into pellets by dry blending glass fibres with PA66 pellets and then are injection moulded into test samples (tensile, flexural and plate specimens). After injection moulding, the test samples are immediately sealed in antistatic and opaque polyethylene bags to keep them dry as moulded and avoid any exposition or contamination from the exterior. All test samples in this study come from the same batch of material and are henceforth named PA66-GF35 (A3HG7) and PA66-i-GF35 (A3ZG7) for the toughened material.

3.2.2. Mechanical testing

PA66-GF35 and PA66-i-GF35 samples are tested in dry as moulded condition in quasi-static and dynamic loads. All of the test samples are ensured to be free from visible flaws, scratches, pits, sink marks or other imperfections. All the tests are conducted at a room temperature of 23°C.

For the quasi-static tests, tensile and three-point flexural tests at constant rate are carried out on an Instron 5500R 5/100 KN electro-mechanical testing machine (Figure 4-a). The specifications of tensile and flexural test specimens comply with their respective ISO standards, ISO 527 and ISO 178. Tensile test samples are flat dumb-bell type 1A with an overall length of 170 mm, a width at ends of 20 mm, a width of narrow portion of 10 mm and a thickness of 4 mm. The cross-head displacement is set to 1 mm/min. Flexural test samples are rectangular parallelepiped bars with an overall length of 80 mm, a width of 10 mm and a thickness of 4 mm. The cross-head displacement is set to 2 mm/min. In both case, the injection moulding is made lengthwise. A minimum of 10 samples per tested material is performed.

For the dynamic tests, Charpy, drop weight and air gun impact tests are carried out. Charpy impact strength tests (Figure 4-b) are performed to determine and compare the amount of impact energy absorbed in breaking by the materials, defined as the difference between the initial energy of the pendulum and the energy remaining in the pendulum after breaking the samples. The tests comply with standards ISO 179 and are performed with a Losenhausenwerk pendulum impact tester with 294 J test capacity. The effective striker mass was 6.031 kg and the initial velocity of the striker at the point of impact was 3.8 m/s. Charpy test samples are injection moulded lengthwise test bars type 1eU (specimen type 1, edgewise hit and

unnotched) of 80 mm long with a cross-section of 4 mm by 10 mm. A minimum of 10 tests per material was performed. Test samples are placed on supports 62 mm apart and rest on their wider side, and are impacted edgewise by a single swing of the pendulum with the line of impact midway between the supports.

Drop weight impact tests comply with standards ASTM D5420 and are conducted with a Rosand instrumented falling weight impact tester type 5 (Figure 4-c). The tests performed drop a 3170 g weight assembly to which is attached a 10 mm hemi-spherical impactor. The impact energy is ranged from 2 to 5 J corresponding to an impact velocity range from 1.1 to 1.8 m/s. The incident velocity of the falling mass is measured just before striking the test sample. The dropping weight is instrumented and measure force and displacement. It is also fitted with a pneumatic rebound brake so as to prevent multiple impacts.

Gas gun impact tests are conducted with a low velocity gas gun (Figure 4-d) manufactured by Sabre Ballistics Ltd with up to 8 bars of effective low pressure. The tests performed propel a 22 g projectile with a 10 mm hemi-spherical profile to the centre of the plate. The desired projectile velocity is obtained by adjusting the pressure of the gas before firing. It obtains velocity by using a solenoid valve that releases a set volume of gas into a chamber within the gun. The gun is positioned thanks to a laser beam. The distance of firing is set to 400 mm and kept constant.

This distance is chosen for being not to close to the target avoiding rebound damage on the barrel and not too far minimising the loss of velocity of the projectile due to gravity and air friction. The projectile velocity is recorded at the muzzle of the barrel via two fibre optic sensors. The impact energy of the impact is ranged from 2 to 7 J corresponding to an impact velocity range from 13.5 to 25.2 m/s. The impactor and projectile chosen in

Figure 4-e correspond to an average 10 mm dart profile road stone. Test samples for the drop weight and gas gun tests are square panels or plates of 70 mm in length and 4 mm in thickness, injection moulded from one edge. In both situations, a clamping frame constrains the edges of the plate leaving an exposed surface to impact of 50 by 50 mm. A minimum of 5 tests per energy per material were performed at 90° to surface.

a. Electromechanical Tester

b. Charpy Impact Pendulum

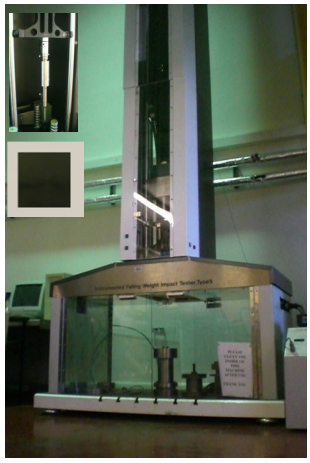

c. Drop Weight Tower

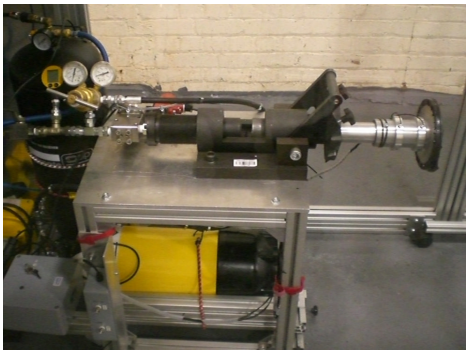

d. Low Velocity Gas Gun

e. Road Stone, Projectile, Impactor

Figure 4 – Mechanical Testing Machines, fixtures and samples

The damage assessment after an impact test is made by visual inspection on the external surfaces of the impacted sample. However sometimes it can be difficult to determine whether or not the sample has failed. This is particularly true when the intensity of the impact is near the failure threshold that the structure can withstand. For that reason, the recourse of a non-destructive testing is needed to inspect and eventually determine the extent of the damage. Therefore, the ultrasonic C-Scan

technique is used to detect any damage by the attenuation or reflexion of ultrasonic waves across the impacted sample.

3.3. Finite element analysis

The assessment of the material impact resistance in different configurations with varying parameters has driven the need to employ finite element simulations to approach, benchmark and predict strength and fracture behaviour of stressed parts. The finite element method is used as a tool for its predictive capabilities to solve numerically and represent analytically the behaviour of a physical system. This system is divided in elements linked together by nodes forming a mesh to which properties and relations of interactions are allocated. This method gives an approximate solution to a problematic. When considering building a model of a physical system it is particularly important to employ a consistent system of units as shown in Table 5, the units used.

Table 5 - Homogeneous system of units

Length	Time	Mass	Loads	Velocity	Mass Density	Force	Energy
mm	s	Tonne	MPa	mm/s	Tonne/mm^3	N	mJ

The test samples were directly designed and meshed within the computer using HyperMesh from Altair HyperWorks 9.0 with LS-DYNA

interface. Once the geometries are ready, the pre-processing begins assigning sections, materials properties and configuring behaviours, interactions and boundary conditions in the environment. The pre-processing was completed with LS-PrePost 2.4 whilst the simulations were processed with LS-DYNA solver version 970 both from LSTC. LS-DYNA was selected for its analysis capabilities (non-linear dynamics, failure analysis, crack propagation and more) and also its comprehensive library of materials models and contact algorithms. LS-PrePost 2.4 was also used to complete the post-processing analyses.

The simulations are based on the stress-strain relations obtained from the experimental work with fixed conditions to describe a specific situation. The representation of the material uses elasto-plastic material law [126; 127]. The elastic Young's modulus defines the stress-strain relation up to the yield stress. Above yield stress, the plastic behaviour is described by the effective stress and effective plastic strain coordinates. The effective plastic strain is the unrecoverable portion of the true strain beyond the yield limit. When defining the effective stress versus effective plastic strain curve, the first plastic strain value would be zero and the first stress value would be the initial yield stress, see material card in Figure 5-a. The material failure is set using strain failure criterion. If the calculated effective plastic strain for any element exceeds the predefined value, the element is removed from the model and the simulation continues with the eroded model. For simulating

the behaviour of a rate-depend material, the stress versus effective plastic strain curve implemented in the material card is adjusted in correlation with the strain rate applied to the model. Therefore, the failure criterion is updated in relationship with the strain rate.

Tensile and flexural models (Figure 5-b and Figure 5-c) are meshed in 3D quads with respectively 3,440 and 2,000 solids elements in where 1 element represents 1 mm in the thickness and 2 mm in the length. As being quasi-static, an implicit card is implemented in the model. Material type 24 piecewise linear plasticity is used. The tensile model is constrained on one end and a displacement is applied to a set of nodes on the other end. The flexural model is placed on constrained cylinders and displacement is set to a third cylinder on the top.

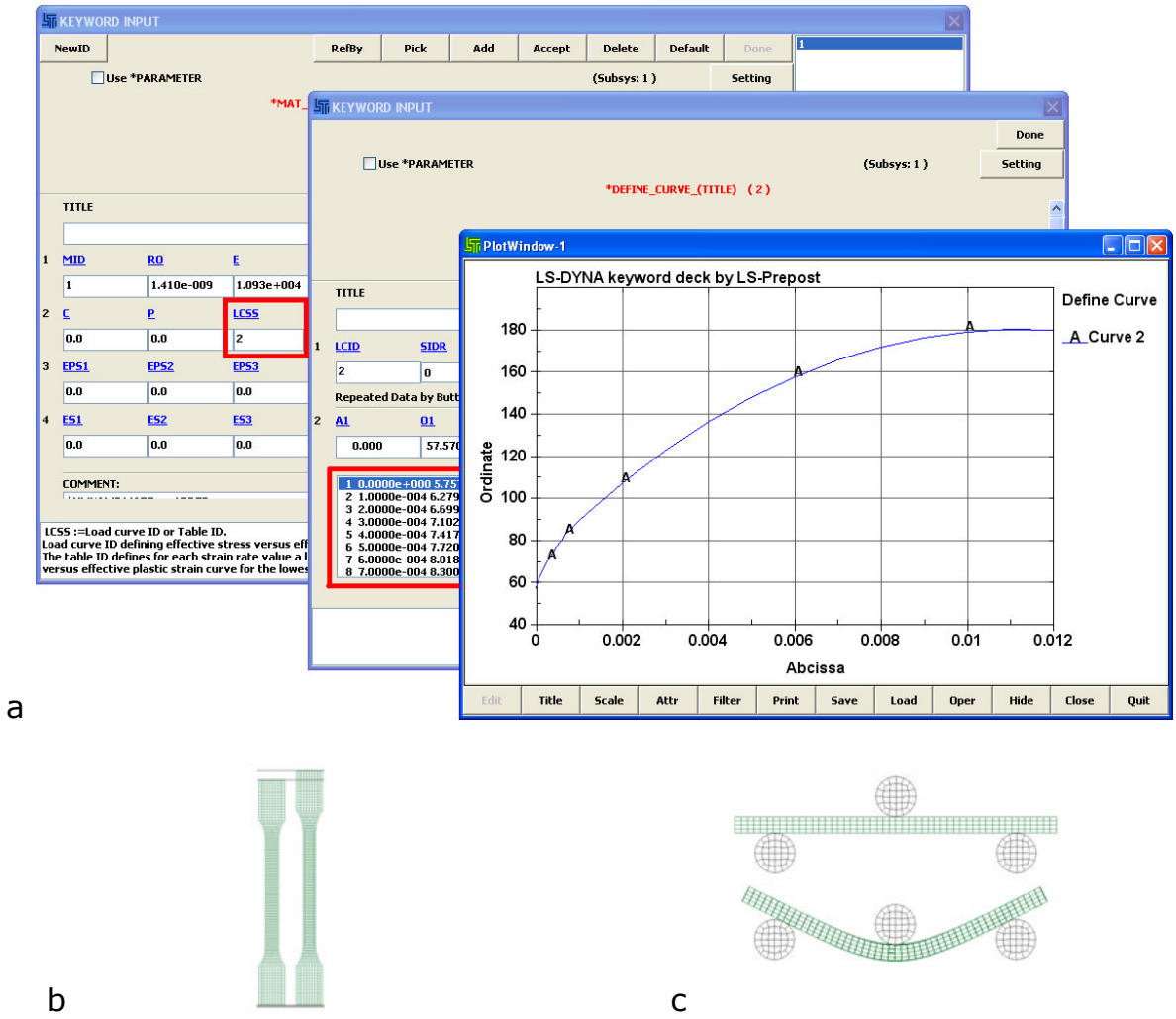

a

b

c

Figure 5 - Implementation on material card (a) and tensile (b) and flexural (c) models

A model of the plate was defined for the simulations using loaded curves of effective stress versus effective plastic strain relations at different strain-rate in order to describe the material nonlinear behaviour. Another way that can be used it to defined the load curve as force versus deflection function. The material used is the type 24, piecewise linear plasticity, with a strain failure flag. The plate model has 9800 3D quads solid elements. The

projectile impacting the plate is defined as a rigid material and hits the centre of the plate. The plate is constrained around its edges, like in the experiment, leaving a free to deflect area of 50 by 50 mm (Figure 6).

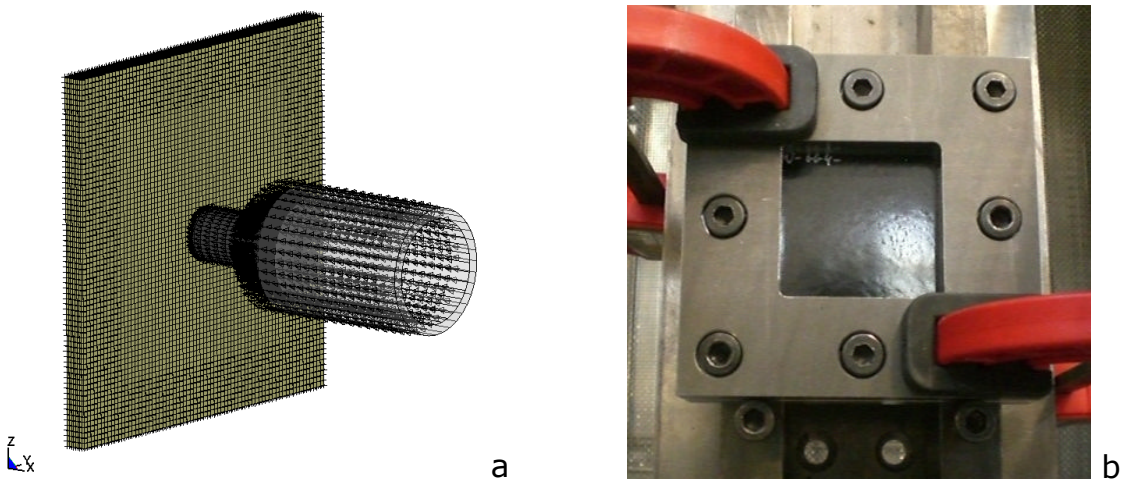

Figure 6 - Constrained plates in simulation (a) and experiment (b)

A contact algorithm is formulated to prevent interpenetration between the projectile and the impacted surface or self-contact during the impact. In LS-DYNA, a contact is defined by identifying what locations are to be checked for a potential penetration of a slave node through a master segment [166]. When a penetration is found a force proportional to the penetration depth is applied to resist and ultimately eliminate the penetration. Automatic contact options are used, as these contacts are non-oriented meaning that they can detect penetration coming from either side of a shell element. The contact surfaces are determined by projecting normally from the shell mid-plane a distance equal to one-half the contact thickness and at the exterior edge of a shell surface, the contact surface

wraps around the shell edge with a radius equal to one-half the contact thickness thus forming a continuous contact surface. The contact treatment allows for compression and tangential loads to be transferred between the slave nodes and the master segments. The choice of the master and slave surfaces is arbitrary when the symmetric penalty treatment is employed. Otherwise, the most coarsely meshed surface should be chosen as the master surface unless there is a large difference in mass densities in which case the side corresponding to the material with the highest density is recommended. In this study, the projectile is taken as master and the impacted sample is taken as slave.

3.4. Results and discussion

3.4.1. Quasi-static tests

Tensile and three-point flexural tests on PA66-GF35 and PA66-i-GF35 were performed to assess the mechanical properties for each material and also to collect relevant data for the simulations.

Figure 7 shows the tensile load versus the extension for materials PA66-GF35 and PA66-i-GF35. These data are collected directly from the testing machine. PA66-GF35 tensile samples undergone a maximum tension force of 7 kN and extended by 5.2 mm. PA66-i-GF35 tensile samples

undergone a maximum tension force of 5.2 kN and extended by 7.1 mm. The transition between elastic to plastic domain is noticeable in both materials at around 2kN below 1 mm extension. PA66-GF35 material is able to withstand a higher tensile load by around 35% more than PA66-i-GF35. However in return, PA66-i-GF35 material extends 37% more than PA66-GF35.

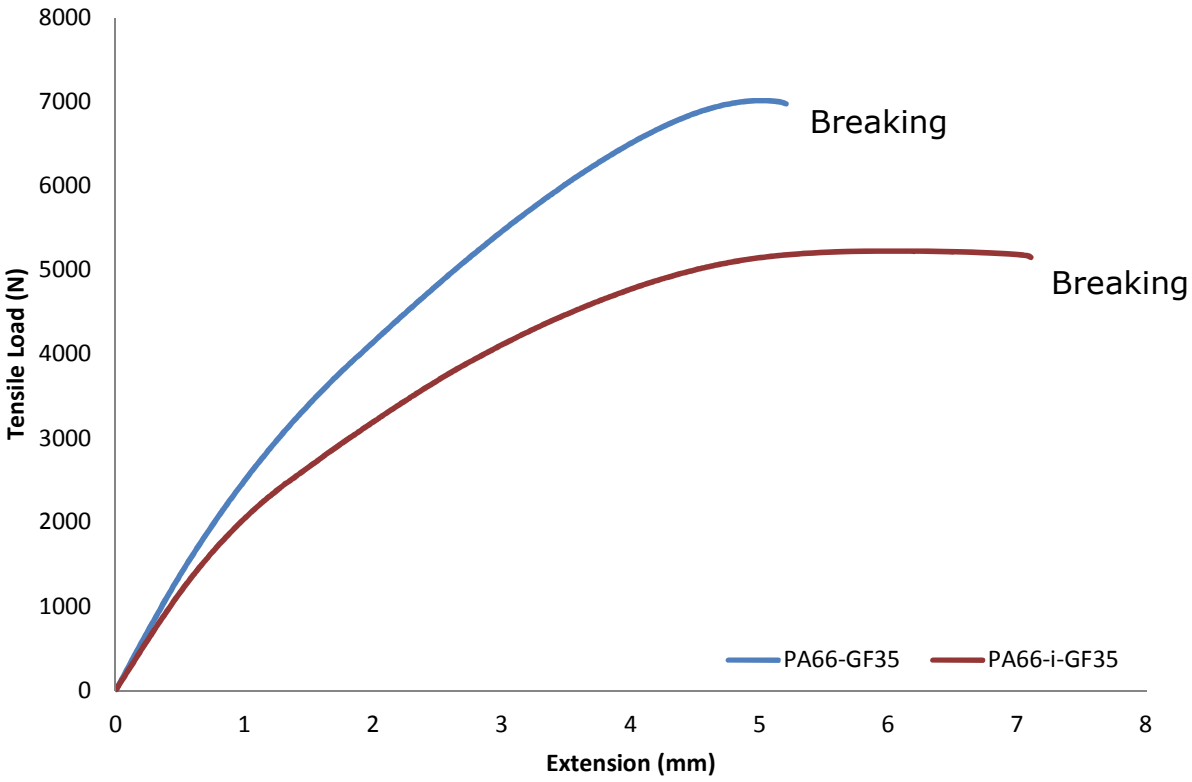

Figure 7 - Tensile load versus extension

Figure 8 shows the flexural load versus the deflection for materials PA66-GF354 and PA66-i-GF35. These data are collected directly from the

testing machine. PA66-GF35 flexural samples undergone a maximum flexion force of 340 N and extended by 9.1 mm. PA66-i-GF35 flexural samples undergone a maximum tension force of 250 N and extended by 13 mm. PA66-GF35 material is able to withstand a higher flexural load by around 36% more than PA66-i-GF35. However in return, PA66-i-GF35 material extends 43% more than PA66-GF35.

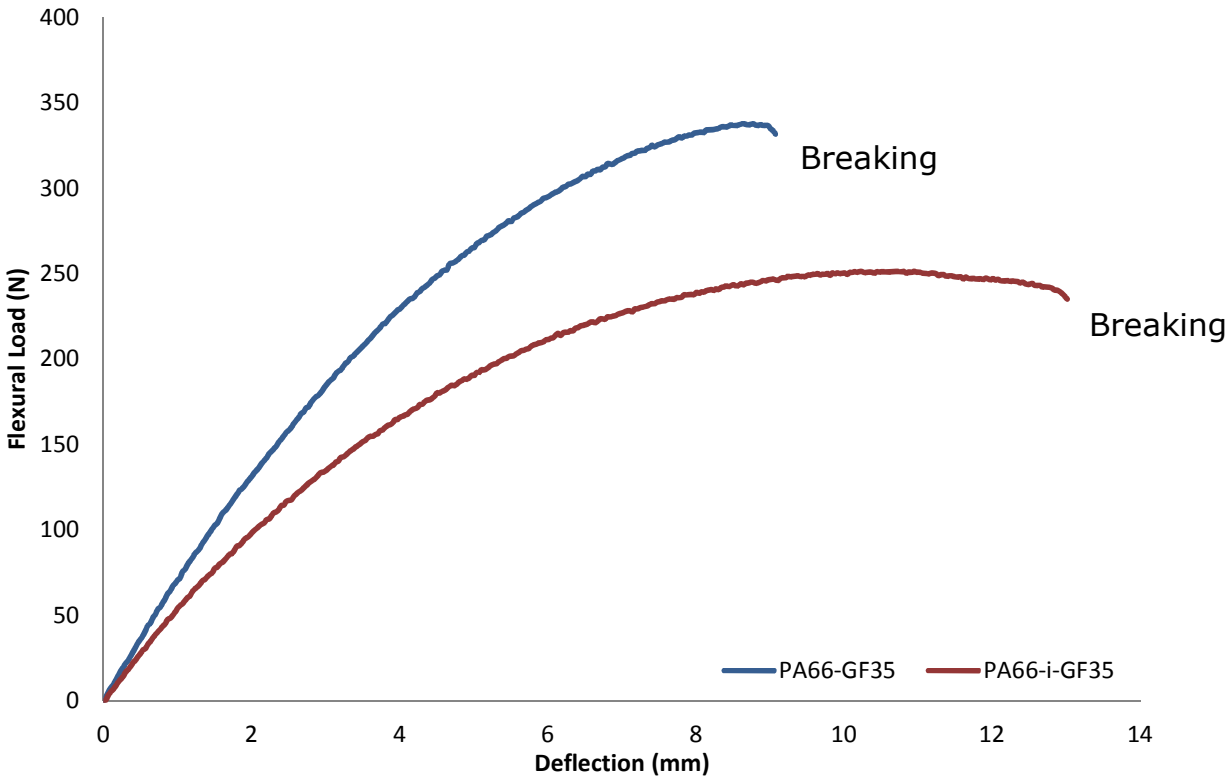

Figure 8 - Flexural load versus deformation

Plastics are complex materials to describe, performing in a non-linear way that is not easily accessible by conventional material models with roots

in metals theory [126]. The plastic strain begins prior to yield and the elastic behaviour is non-linear. Their behaviour is rate-dependent and another problem arises with the glass reinforcement. In addition to increasing stiffness, fibres also change the way plastics fail and often from ductile to brittle [127]. The material is anisotropic since the fibres are oriented by the flow during the injection moulding process. Despite fully dedicated material laws, it is possible to conduct meaningful analyses.

Figure 9 shows the stress-strain relations of PA66-GF35 and PA66-i-GF35 in tension stress conditions. These relations are calculated from the tensile load and extension of Figure 7. All stress values are calculated on the basis of the initial cross-sectional area of the test specimen: $\sigma = \frac{F}{A}$ where σ is the tensile stress value expressed in megapascal, F is the measured force concerned expressed in newton and A is the initial cross-sectional area of the specimen expressed in square millimetre. All strain values are calculated on the basis of the gauge length: $\varepsilon = 100 * \frac{\Delta L_0}{L_0}$ where ε is the strain value expressed in percentage, L_0 is the gauge length of the test specimen expressed in millimetre and ΔL_0 is the increase in the specimen length between the gauges marks expressed in millimetre. The modulus of elasticity is calculated on the basis of two specified strain values: $E_t = \frac{\sigma_2 - \sigma_1}{\varepsilon_2 - \varepsilon_1}$ where E_t is the Young's modulus of elasticity expressed in megapascal, σ_1 is the stress in megapascal measured at the strain value ε_1=0.0005 and σ_2 is

the stress, in megapascal, measured at the strain value ε_2=0.0025. The cross-section was measured during and after each test and there was no necking.

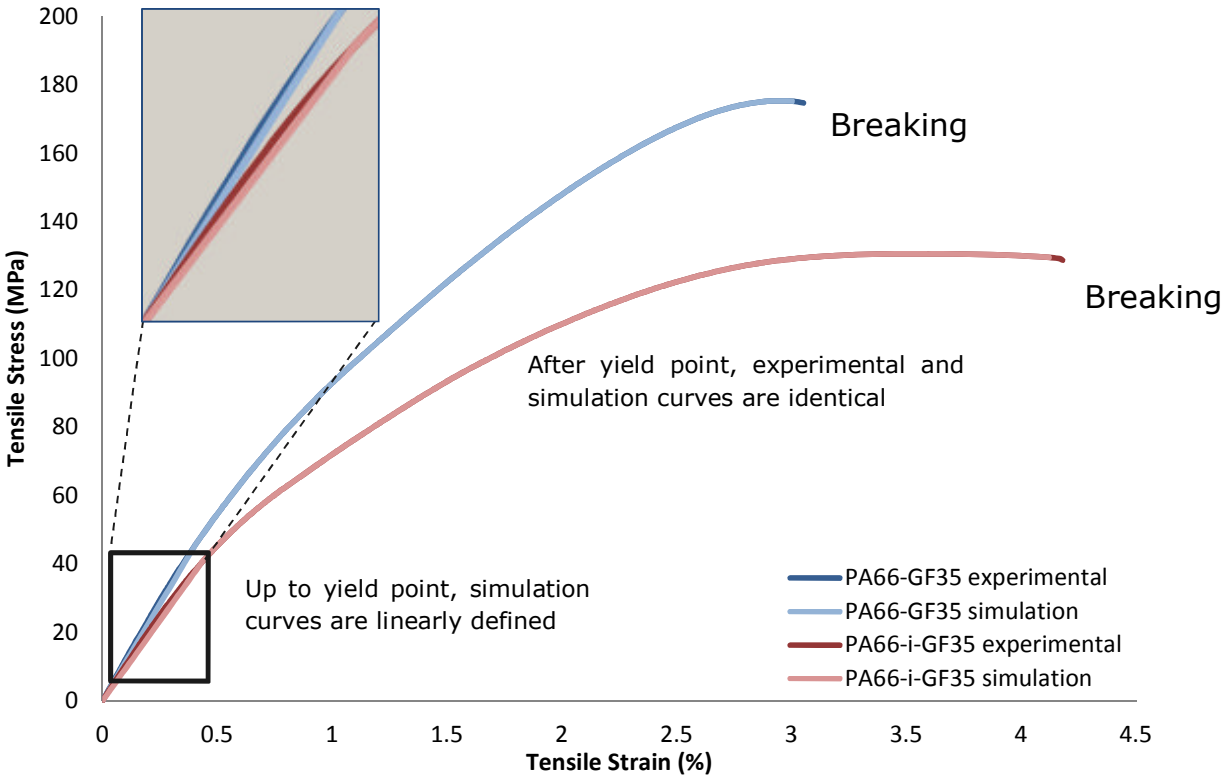

Figure 9 - Experimental and simulated tensile stress-strain relations

Table 6 provides relevant mechanical properties of PA66-GF35 and PA66-i-GF35 in tension condition. PA66-GF35 has its Young's modulus 20% higher than PA66-i-GF35 and its tensile strength is 34% superior. On the other hand, PA66-i-GF35 has its strain to failure 36% extended than PA66-

GF35. This means that PA66-i-GF35 is more ductile than PA66-GF35 with a larger plastic deformation permitted.

Table 6 - Mechanical properties in tension

Materials	Young's modulus (MPa)	Maximum tensile stress (MPa)	Maximum strain to failure (%)
PA66-GF35	11848	175	3.05
PA66-i-GF35	9950	131	4.16

Figure 10 shows the stress-strain relations of PA66-GF35 and PA66-i-GF35 in flexion stress conditions. These relations are calculated from the flexural load and deflection of Figure 8. The flexural stress parameters are calculated using the following equation: $\sigma_f = \frac{3\,F\,L}{2\,b\,h^2}$ where σ_f is the flexural stress parameter expressed in megapascal, F is the applied force expressed in newton, L is the span, b the width and h the thickness of the specimen all expressed in millimetre. The flexural strain parameter is defined using the following equation: $\varepsilon_f = 100 * \frac{6\,s\,h}{L^2}$ where ε_f is the flexural strain parameter expressed as a percentage, s is the deflection expressed in millimetre and h is the thickness of the specimen also expressed in millimetre. The flexural modulus is determined by calculating the deflections s_1 and s_2 corresponding to the given values of the flexural strain ε_{f1}=0.0005 and ε_{f2}=0.0025 using the following equation: $s_i = \frac{\varepsilon_{fi}\,L^2}{6\,h}$ (i=1; 2) then the flexural modulus is given by: $E_f = \frac{\sigma_{f2}-\sigma_{f1}}{\varepsilon_{f2}-\varepsilon_{f1}}$ where E_f is the flexural modulus expressed in megapascal and

σ_{f1} and σ_{f2} are the flexural stresses, in megapascal, measured at deflection s_1 and s_2.

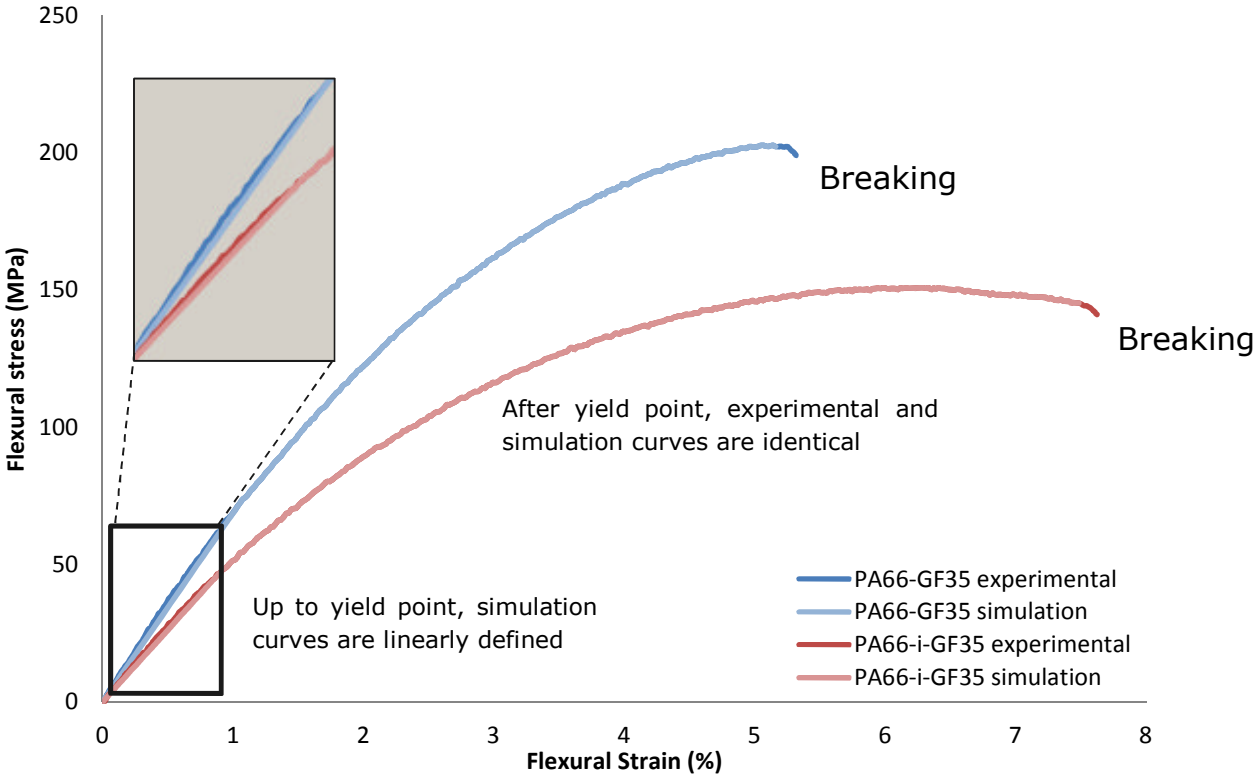

Figure 10 - Experimental and simulated flexural stress-strain relations

Table 7 provides relevant mechanical properties of PA66-GF35 and PA66-i-GF35 in flexion condition. PA66-GF35 has its flexural modulus 23% higher than PA66-i-GF35 and its flexural strength is 35% superior. On the other hand, PA66-i-GF35 has its strain to failure 44% extended than PA66-GF35. As in the tensile tests, PA66-i-GF35 exhibits a larger plastic deformation. This means that PA66-i-GF35 is less brittle than PA66-GF35.

Table 7 - Mechanical properties in flexion

Materials	Flexural modulus (MPa)	Maximum flexural stress (MPa)	Maximum strain to failure (%)
PA66-GF35	7168	202	5.27
PA66-i-GF35	5819	150	7.57

The single curves of each material represents the average behaviour observed made after at least 10 tests. Superimposed on the graphs are the curves obtained from the simulations. The simulations use the data from the experiments with the effective plastic stress-strain relation implemented into the model (refer to section 3.3. and Figure 5-a). The elastic domain is defined by the Young's modulus for the tensile test and flexural modulus for the three-point flexural test up to the set yield point arbitrarily chosen since there is no clear transition between the elastic and the plastic domain with thermoplastics. On the graphs, it is noticed that the simulated behaviour slightly under-predicts the elastic domain. This is due to the difficulty to determine or define the yield transition in these materials. The results obtained after the calibration of the model correlate the findings in the experiments [127]. Despite the fact that short glass fibre reinforced thermoplastics are anisotropic, the material model is considered as homogeneous and simulations gave good approach of their behaviours in these conditions. The model accommodates the strain rate dependency using appropriate stress versus effective plastic strain curves in relation to the strain rate applied [126].

3.4.2. Dynamic tests

Charpy impact strength of unnotched samples a_{cU} is expressed in kilojoules per square meter: $a_{cU} = \frac{W}{h.b} * 10^3$ where W is the energy absorbed in joules by breaking the test sample, h is the thickness and b the width in millimetres of the test sample. All the tests led to a complete break, in which the samples are separated into two pieces. The type of failure observed, when performing impact tests, is a tension failure that is to say when the opposite side of impact fails first. Both materials break in two ways. On the tension side, the breakage has jagged edges, shear lips typical of a ductile fracture. On the compression side, the breakage is on flat plane characteristic to a brittle fracture. Table 8 shows the Charpy impact strength of PA66-GF35 and PA66-i-GF35 in dry as moulded condition.

Table 8 - Charpy impact strength in dry as moulded condition

Materials	Energy absorbed (J)	Impact strength (kJ/m^2)
PA66-GF35	4.14	103.38
PA66-i-GF35	4.07	101.69

Force versus displacement graphs from drop weight impact tests on plates are presented to describe and analyse the resistance to impact of PA66-GF35 and PA66-i-GF35 in dry as moulded condition. Figure 11 and Figure 12 show the lower and upper limit of impact energy resistance of

PA66-GF35 and PA66-i-GF35 in dry as moulded condition. This also allows the assessment of the maximum impact strength to failure for each material. PA66-GF35 samples fail between 2.5 and 3 J. The maximum deflection prior to failure is around 1.14 mm (28.5%), and the maximum force prior to failure is between 1360 and 1480 N. PA66-i-GF35 samples fail between 3 and 3.5 J. The maximum elongation prior to failure is around 1.32 mm (33%), and the maximum force prior to failure is between 1240 and 1320 N. All materials start to deflect at just above 900 N. PA66-i-GF35 has slightly lower impact strength than PA66-GF35 but in return it deflects more before the first failure.

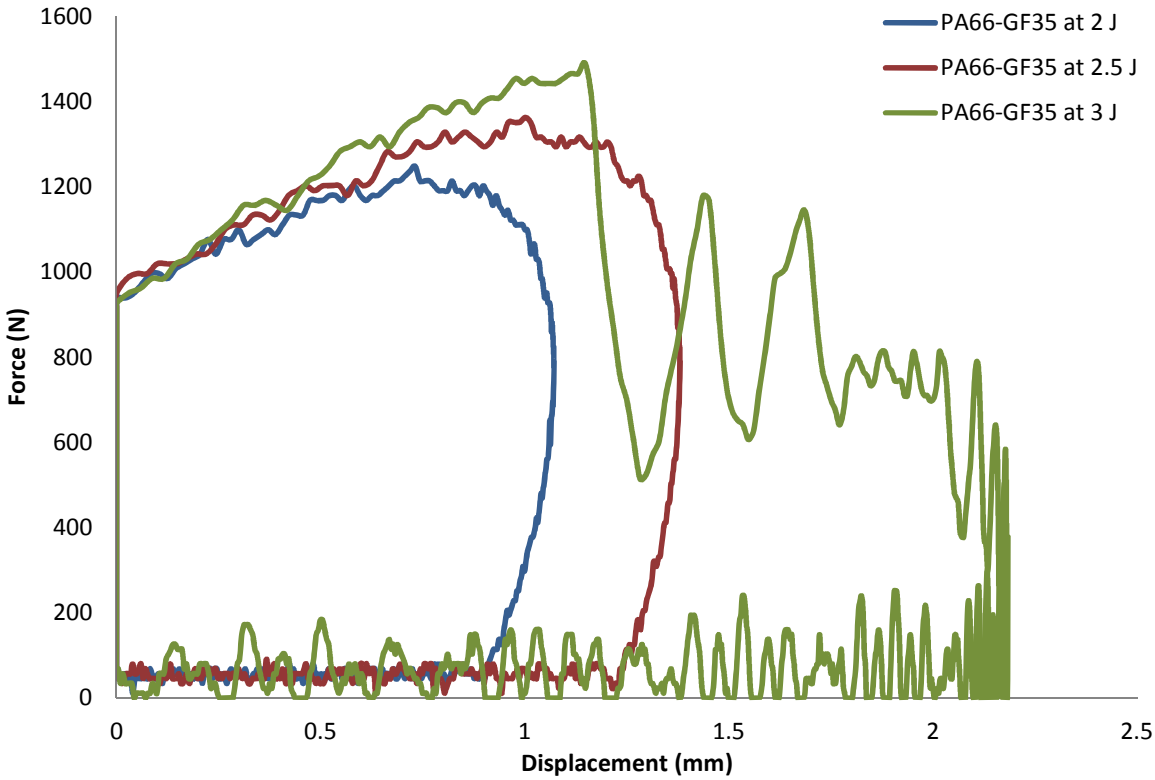

Figure 11 - PA66-GF35 impacted at 2, 2.5 and 3 J

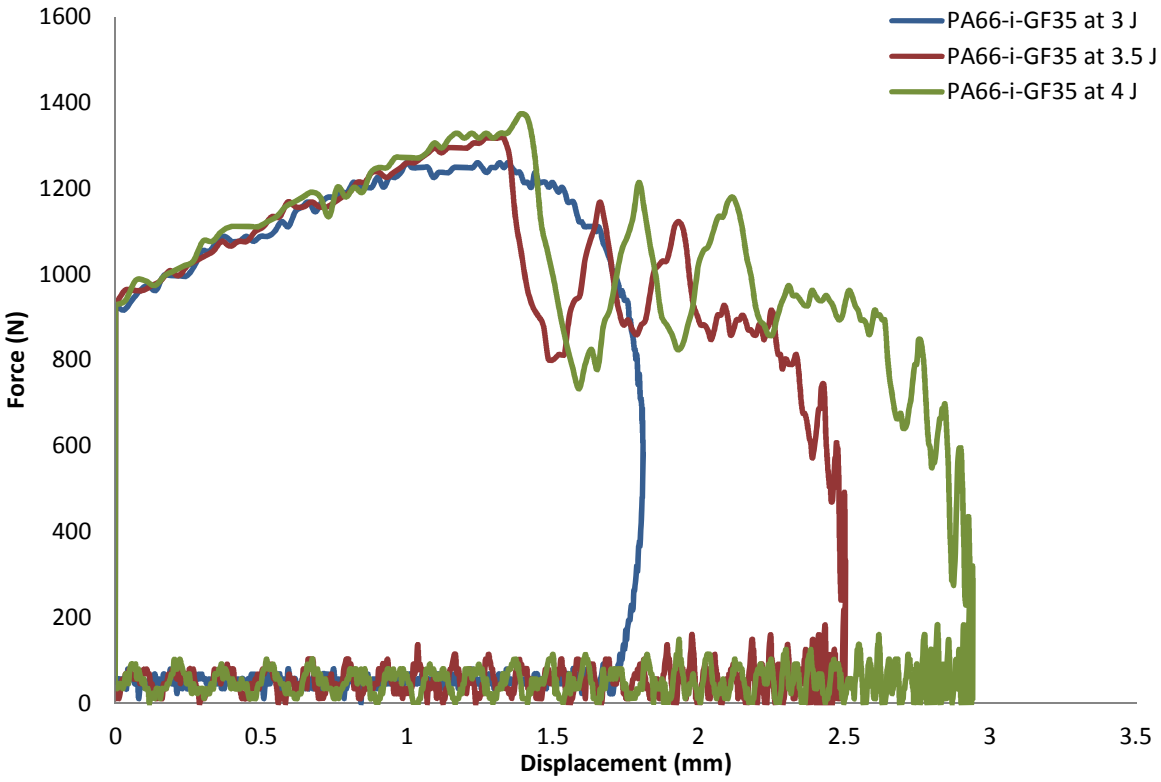

Figure 12 - PA66-i-GF35 impacted at 3, 3.5 and 4 J

Figure 13 compares both materials at 3 J in dry as moulded condition, and shows their differences in terms of impact resistance and behaviour. PA66-GF35 fails at 1480 N after a 1.14 mm deflection (28.5%). Its resistance drops to 520 N, which accelerate the damage and the deflection up to 2.19 mm (55%). Nonetheless, the PA66-GF35 plates recover their initial positions after the impact. On the other hand, PA66-i-GF35 withstands the impact despite starting to deflect at the same force and displaying a

lower strength. At the end, its deflection is lower and reaches 1.8 mm (45%).

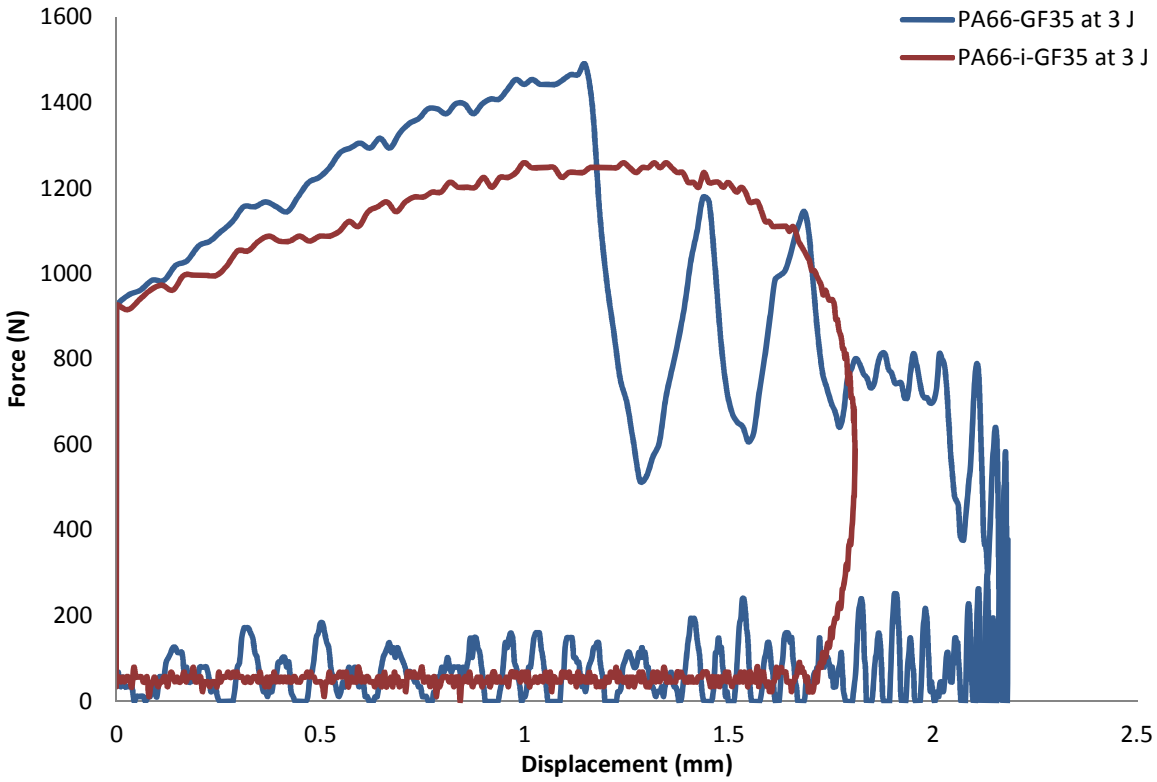

Figure 13 - PA66-GF35 and PA66-i-GF35 impacted at 3 J

The gas gun impact tests show that PA66-GF35 and PA66-i-GF35 plates fail between 3.45 and 4.05 J corresponding to a velocity of 17.70 to 19.18 m/s. At first sight, there is no distinction between them. However, the major difference comes from the scale and the shape of the failure and this is verified up to 6.5 J or 24.31 m/s. PA66-GF35 tends to fail with a cross-shaped crack whereas PA66-i-GF35 fails with a linear crack (failure within

one direction). The scale of the damage increases with the energy but it is more pronounced for PA66-GF35 than PA66-i-GF35.

Table 9 presents the impact energies and their corresponding velocities to which PA66-GF35 and PA66-i-GF35 plates in dry as moulded condition were subjected by the air gun impact tester and Table 10 provides the assessment of their damage, post-impact, characterised by the shape and the size of the failure.

Table 9 - Gas gun impacts on plates in dry as moulded condition

Sample ID test	Kinetic Energy (J)	Velocity (m/s)	Result
PA66-GF35_01	2.00	13.51	OK
PA66-GF35_02	3.45	17.70	OK
PA66-GF35_03	4.05	19.18	Crack_01
PA66-GF35_04	4.65	20.55	Crack_03
PA66-GF35_05	6.20	23.75	Crack_05
Sample ID test	Kinetic Energy (J)	Velocity (m/s)	Result
PA66-i-GF35_01	2.04	13.61	OK
PA66-i-GF35_02	3.57	18.02	OK
PA66-i-GF35_03	3.93	18.90	Crack_02
PA66-i-GF35_04	4.32	19.81	Crack_04
PA66-i-GF35_05	5.90	23.16	Crack_06

Table 10 - Damage assessment on gas gun impacted plates in dry as moulded condition

Crack ID	Size (mm)	Shape
Crack_01	22*22	Y
Crack_02	19	I
Crack_03	28*21	X
Crack_04	20	I
Crack_05	28*26	X
Crack_06	22	C

The damage was assessed by visual inspection but sometimes this can be difficult. In this situation, the use of an ultrasonic C-Scan is useful.

Figure 14 shows PA66-i-GF35 impacted with the gas gun at 3.5 J with no visual damage but only the impact mark of the projectile. The echo image of the C-Scan reveals the extent of the impacted area. The red colour indicates full reflexion of the ultrasonic waves. The more heterogeneous or damaged the material is the less ultrasonic waves are reflected with a C-Scan colour legend going from orange to blue. In the impacted area, the speed of the ultrasonic waves is slightly attenuated. Their reflections against the material are lower than outside of the impact (from 10 to 20% less) but no failure is encountered. The surface of the sample was crushed and the material was plastically deformed.

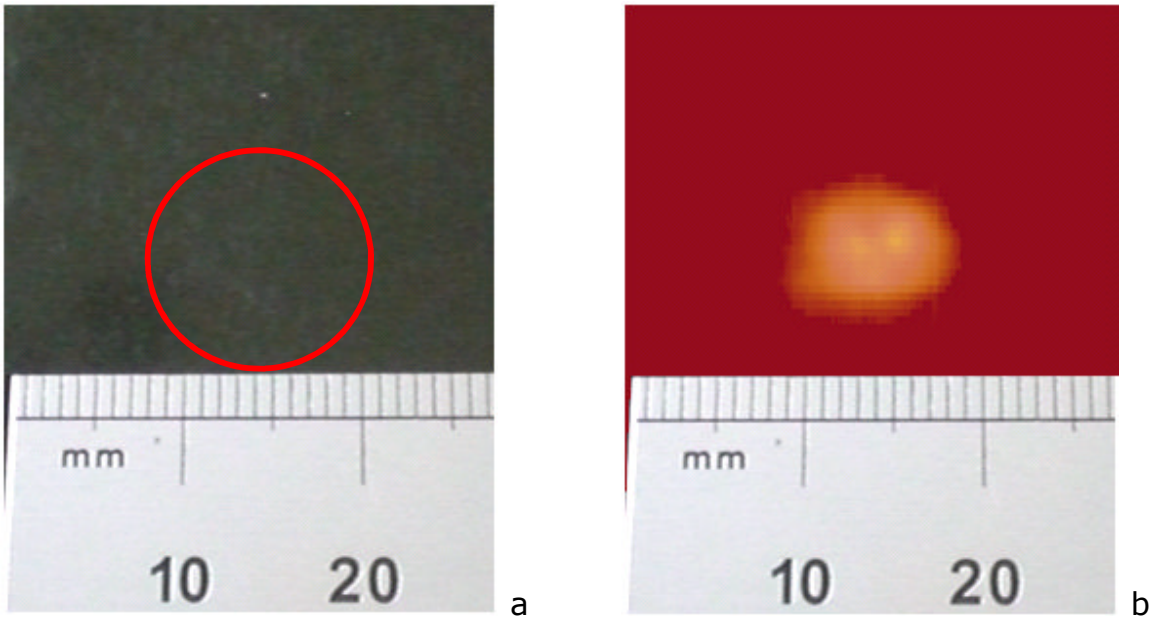

a b

Figure 14 - PA66-i-GF35 plate impacted at 3.5 J, visual inspection (a), C-Scan image (b)

Figure 15 shows PA66-i-GF35 impacted with the gas gun at 4 J. The visual inspection indicates a tiny white mark in the centre of the impacted area, which is possibly the sign of glass fibres detached from the matrix but cannot distinguish between a scratch and a crack. The echo image of the C-Scan reveals that the sample has failed by cracking in a linear way. The reflection of ultrasonic waves is dramatically attenuated in the middle of the crack as shown by the fading colours from orange (10% less) to blue (70% less). The extent of the crack (length) can be measured.

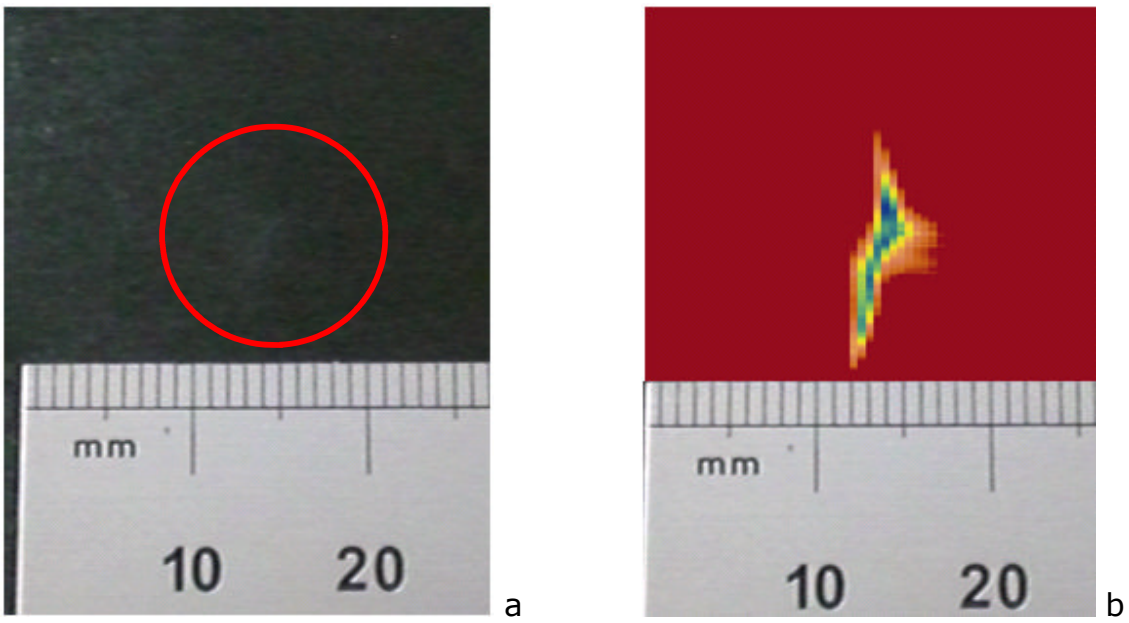

a b

Figure 15 - PA66-i-GF35 plate impacted at 4 J, visual inspection (a), C-Scan image (b)

Figure 16 shows the force versus displacement on a PA66-GF35 plate impacted at 5 J experimentally and simulated. It comes from one test against one replica. The experimental impact is measured from a 5 J drop

weight impact and the 5 J simulated impact is measured from the elements of the plate in the impact point area. There are some variations on the forces, and particularly half way into the deflection. However, the general behaviour of the simulated impact is correlating to some extent with the experimental impact. Both impacts start to deflect at approximately an equivalent force of 1200 N, and fail after 0.5 mm deflection. From then on, the increase of the damage is arbitrary, the forces fluctuate but augment. The maximum deflections are matching at around 2.88 mm. The recovering rate to the initial position follows a comparable slope [126; 166; 167].

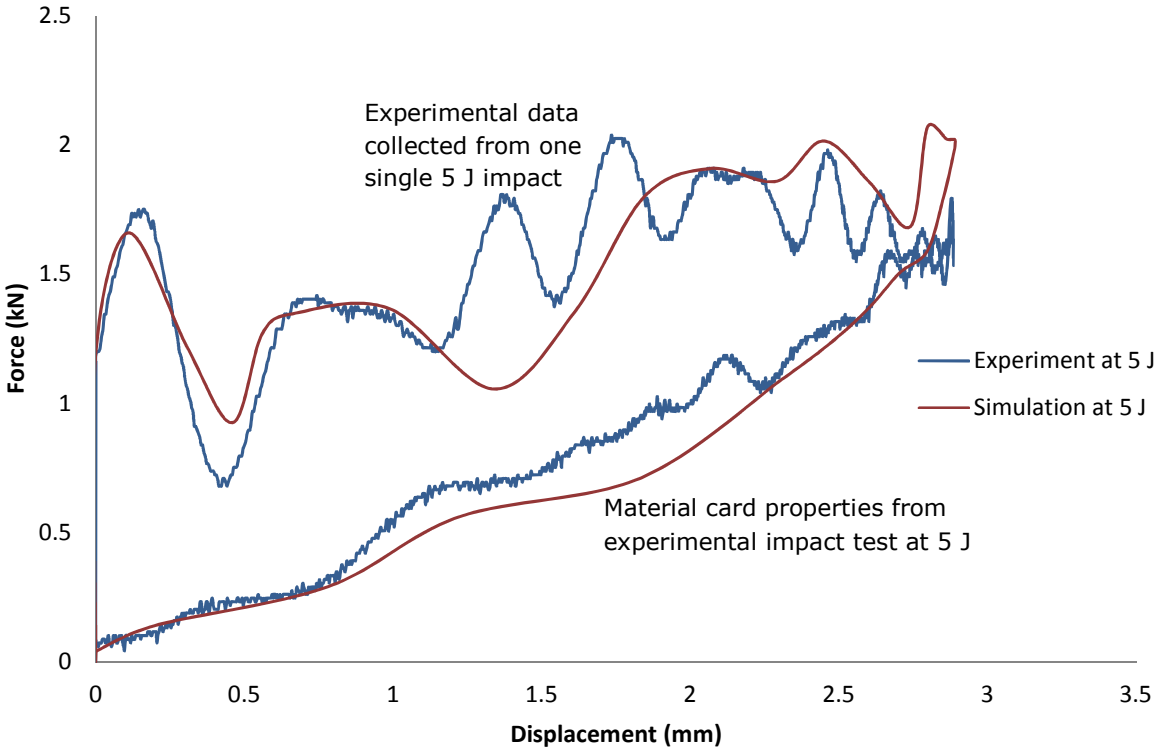

Figure 16 - Experimental and simulation impact at 5 J on PA66-GF35

3.5. Conclusions

In this study, glass reinforced polyamide 66 (PA66-GF35) and rubber toughened glass reinforced polyamide 66 (PA66-i-GF35) were examined in dry as moulded conditions in terms of tensile, flexion properties and impact strength.

The incorporation of a rubber additive (copolymer) lowered the Young's modulus and flexural modulus by around 20% with maximal strengths 35% inferior than PA66-GF35 making PA66-i-GF35 less stiff. On the other hand, PA66-i-GF35 is more ductile with a strain to failure 40% superior than PA66-GF35. In Charpy test, both materials are very much comparable in terms of fracture toughness. Injection moulded plates of PA66-GF35 and PA66-i-GF35 materials were impacted at different energies with a dropped impactor and a propelled projectile. In comparable impact energy, the rubber toughened polyamide has a better resistance to impact despite displaying lower impact strength by 20%. This is explained by a greater plastic deformation which allows the rubber toughened material to better withstand the impact. PA66-GF35 fails earlier due to its stiffness and shorter plastic deformation. The measurement of the damage extent has shown that the rubber toughened material fails in a linear way (straight crack line) whereas the PA66-GF35 grade fails in all directions (star shaped

crack). The rubbery particles of the additive blended with the matrix create a more toughened matrix absorbing more energy and reducing the matrix failure type by inducing yielding processes in the matrix. As a consequence, the interface between the matrix and the fibres is where the crack propagates. Without the rubber-based additive, the crack propagates not only in the interface matrix-fibres but also through the matrix [89; 90]. The finite element analyses were performed using data collected from the experiments. The behaviour to impact of each material was implemented in the model using stress-strain relations and the failure defined by strain criterion. The drawback of this method is in the strain-rate dependency of these materials and therefore changing the impact energy requires affecting the corresponding behaviour of the material. However, the simulated impact behaviours correlate with the experiments in terms of maximum deflection and failure predictions.

Chapter 4. Influence of moisture and aqueous $CaCl_2$ uptakes on mechanical properties of short glass fibre reinforced polyamide 66s

4.1. Introduction

Polyamides are known to absorb large amounts of moisture especially PA6 and PA66. Water molecules are absorbed into the polyamide molecular matrix, resulting in swelling that causes strength property deterioration and part size increase [168]. However, the addition of reinforcements reduces the effect of moisture on the materials by reducing the available space for absorption of water molecules. Some previous investigations have shown that polyamides tend to plasticise in presence of water and that other consequences are a significant drop of their tensile and flexural modulus and also on their stress at yield [27; 45; 110].

Furthermore, the absorption of dissolved salt is another issue that also affects the properties of polyamides. Typical rock de-icer salts used on roads are NaCl, KCl but largely $CaCl_2$.The polyamides exposed to a salt solution and then dried gain in mass [27; 100]. Some studies, predominantly focused on PA6, looked at the molecular scale effects on polyamides, observing the decrease in crystallinity of polyamides with the increase of $CaCl_2$, changing from mainly crystal phase to mainly amorphous phase [169-171]. The coordination of $CaCl_2$ with amide groups in the polyamide molecules disrupts

and breaks the hydrogen bonding networks which are the major reason that polyamide has an ordered structure. Other investigations have shown that salt solutions can cause stress cracking of polyamides 6 and 66 but aqueous salt solutions have not been reported to cause stress cracking at room temperature only when dissolved with methanol [106; 169]. However, at slightly elevated temperature (50°C) polyamides are susceptible to stress cracking [107; 108].

Little is known on how glass reinforced polyamides 66 behaves to impact when subjected to these environmental conditions. In addition, no previous investigation has reported the effects of water and $CaCl_2$ contents on the mechanical properties of the rubber toughened glass reinforced polyamide 66. This chapter therefore focuses on the effects of water and salt exposure on the mechanical and impact properties on glass reinforced PA66. As mentioned earlier, under-the-hood polyamides components are exposed and susceptible to a wide variety of environmental exposures [110]. Most common ones are those of water splash or salt splash, which occur during rain or icy driving conditions [100].

4.2. Experimental testing

4.2.1. Materials, manufacture and treatments of test samples

PA66-GF35 and PA66-i-GF35 samples were prepared as outlined in the previous chapter, refer to section 3.2.1. All injection moulded test samples were immediately sealed after manufacture in antistatic and opaque polyethylene bags [100] to keep them dry as moulded and avoid any exposure or contamination from the environment.

All test samples were then subjected to two different treatments. One set of samples of both polyamides grades (PA66-GF35 and PA66-i-GF35) were subjected to a water treatment and the other set of samples were subjected to a calcium chloride solution treatment. The salt solution was prepared by stirring one volume of rock salt (2,2 kg of Deco-Pak Rocksalt De-icer) into two volumes of tap water in a bucket until the salt completely dissolved. Each set of samples were weighted and then placed at room temperature into tubs containing water or the salt solution. Samples were weighted weekly and treatments lasted 3000 hours until all samples were completely saturated with no further gain in mass. Table 11 shows the average gain in mass measured after treatment for both materials. It shows that the salt slows down the water uptake into the material and therefore its general gain in mass.

Table 11 - Gain in mass after water and aqueous salt solution treatments after 3000 hours

Gain in mass (%)	PA66-GF35	PA66-i-GF35
Water uptake	2.94	2.83
Aqueous $CaCl_2$ uptake	1.62	1.36

4.2.2. Mechanical testing

The mechanical testing used in this study was already outlined in the previous chapter, refer to section 3.2.2.

4.3. Results and discussion

4.3.1. Quasi-static tests

Effect of water uptake

Figure 17 shows the tensile load versus the extension for materials PA66-GF35 and PA66-i-GF35 when dry as moulded and after water uptake. These data are collected directly from the testing machine. PA66-GF35 tensile samples that have been subjected to water uptake have undergone a maximum tensile force of 4.8 kN and extended by 7.2 mm. Compared to PA66-GF35 in dry as moulded condition that is a loss of 46% of strength but a gain of 38% of extension. PA66-i-GF35 tensile samples that have been subjected to water uptake have undergone a maximum tensile force of 3.8 kN and extended by 10 mm. Compared to PA66-i-GF35 in dry as moulded condition that is a loss of 37% of strength but a gain of 41% of extension. In

both materials, PA66-GF35 and PA66-i-GF35, the water uptake affects the strength in tension but increases the elongation. PA66-GF35 seems to be slightly more affected by the water uptake than PA66-i-GF35.

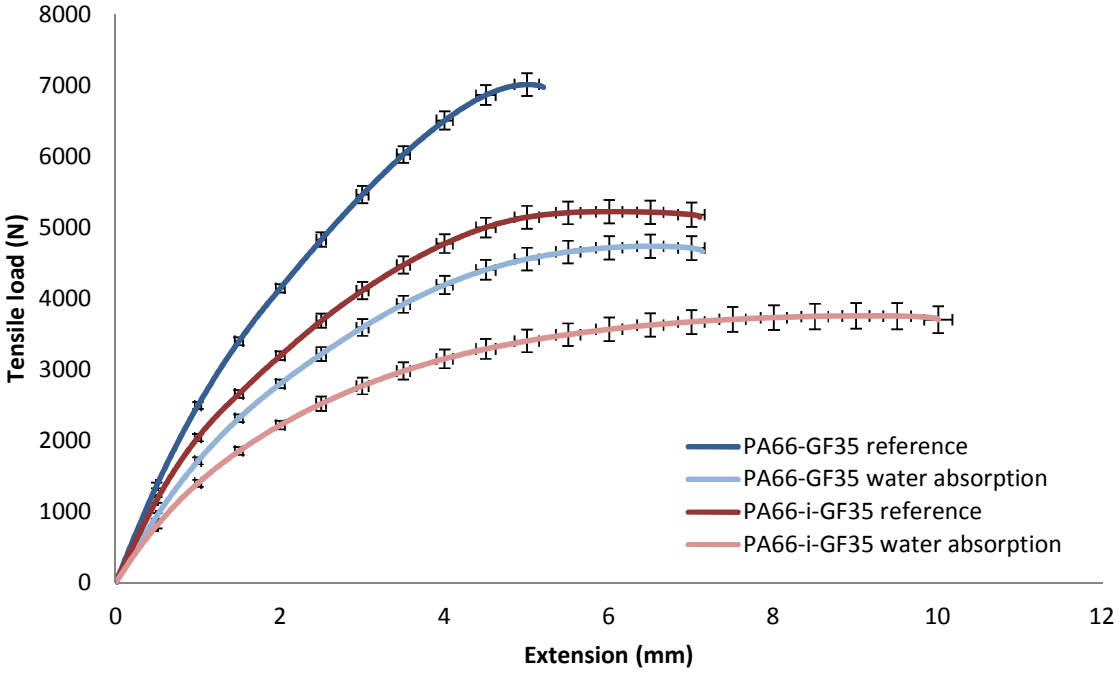

Figure 17 - Tensile load versus extension up to breaking point in dry as moulded and water uptake conditions (with standard deviation)

Figure 18 shows the flexural load versus the deflection for materials PA66-GF354 and PA66-i-GF35. These data are collected directly from the testing machine. PA66-GF35 flexural samples that have been subjected to water uptake have undergone a maximum flexural force of 395 N and deflected by 10.4 mm. Compared to PA66-GF35 in dry as moulded condition that is a gain of 16% of strength and 10% of deflection. PA66-i-GF35

flexural samples that have been subjected to water uptake have undergone a maximum flexural force of 280 N and deflected by 15 mm. Compared to PA66-i-GF35 in dry as moulded condition that is a gain of 12% of strength and 15% of deflection. In both materials, PA66-GF35 and PA66-i-GF35, the water uptake increases the strength in flexion and the deflection.

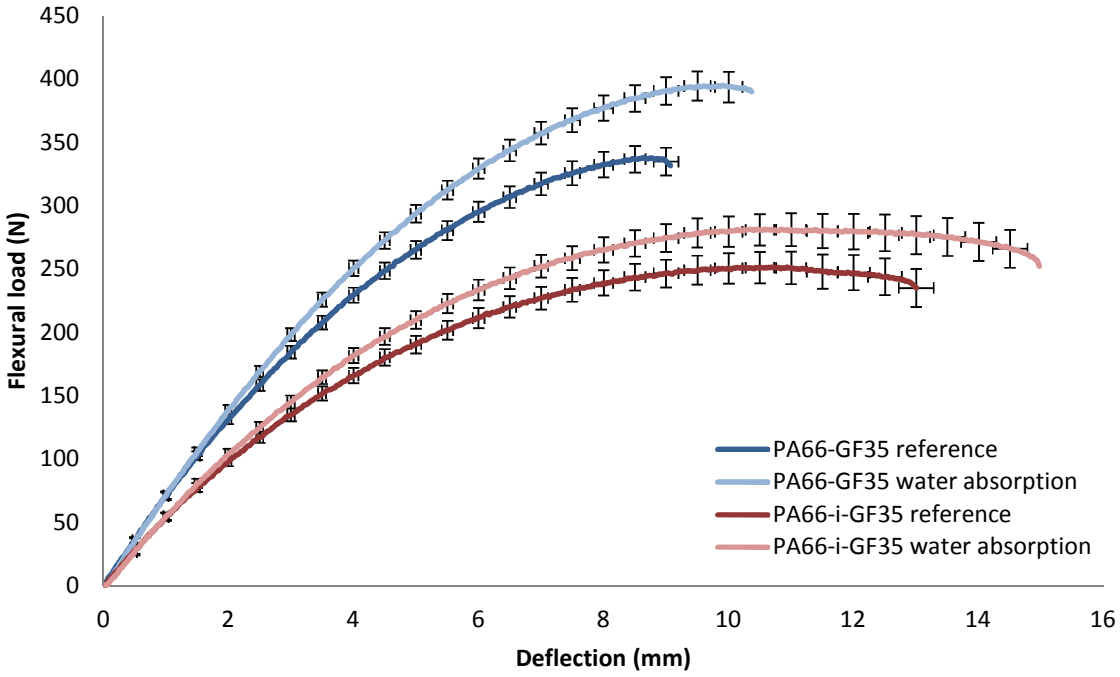

Figure 18 - Flexural load versus deflection up to breaking point in dry as moulded and water uptake conditions (with standard deviation)

Figure 19 shows the stress-strain relations of PA66-GF35 and PA66-i-GF35 when dry as moulded and after water uptake in tension stress conditions. These relations are calculated from the tensile load and extension of Figure 17. PA66-GF35 samples that have absorbed water are affected in

their Young's modulus and tensile strengths. Compared to PA66-GF35 dry as moulded samples, the loss is 47% on the Young's modulus and 48% on the tensile strength. However, there is a gain in their strain to failure of 36%. PA66-i-GF35 samples that have absorbed water are also affected in their Young's modulus and tensile strengths. Compared to PA66-i-GF35 dry as moulded samples, the loss is 45% on the Young's modulus and 39% on the tensile strength. On the other hand, there is a gain in their strain to failure of 40%.

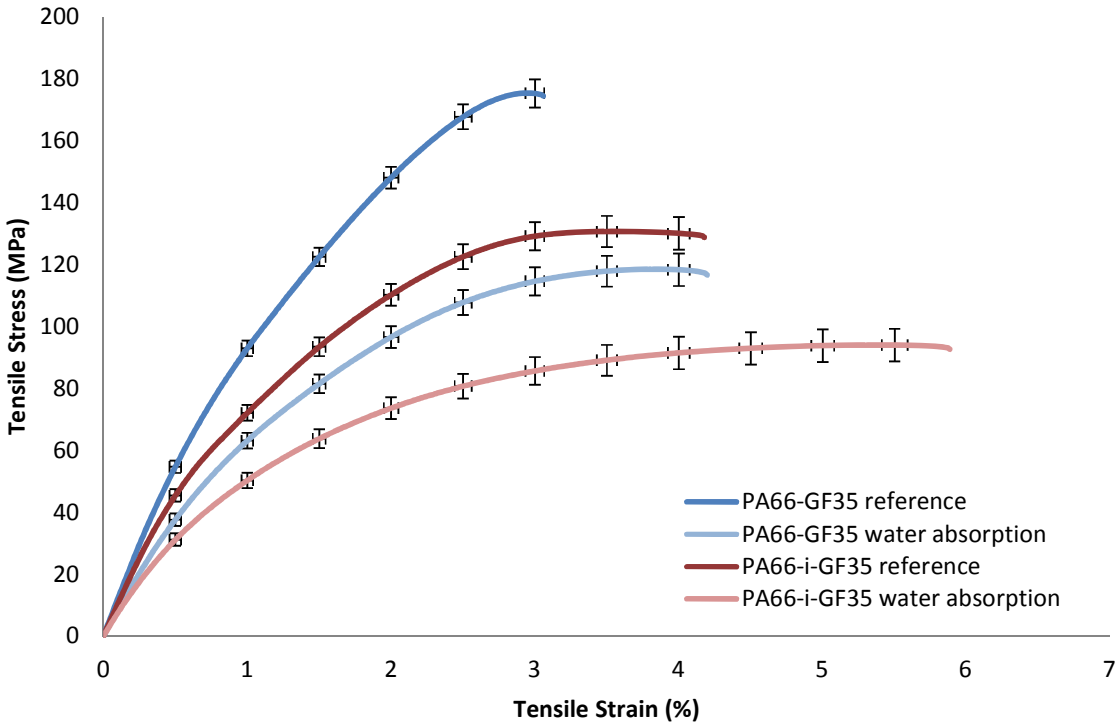

Figure 19 - Tensile stress-strain relations up to breaking point in dry as moulded and water uptake conditions (with standard deviation)

Table 12 summarises the tensile mechanical properties of PA66-GF35 and PA66-i-GF35 in dry as moulded and water uptake conditions.

Table 12 – Tensile mechanical properties in dry as moulded and water uptake conditions after 3000 hours

Properties/ Materials	PA66-GF35 reference	PA66-GF35 water uptake	PA66-i-GF35 reference	PA66-i-GF35 water uptake
Young's modulus (MPa)	11848	8053	9950	6842
Maximum tensile stress (MPa)	175	118	131	94
Maximum strain to failure (%)	3.05	4.16	4.16	5.83

Figure 20 shows the stress-strain relations of PA66-GF35 and PA66-i-GF35 when dry as moulded and water uptake in flexion stress conditions. These relations are calculated from the flexural load and deflection of Figure 18. PA66-GF35 samples that have absorbed water have their mechanical properties improved. Compared to PA66-GF35 dry as moulded samples, the gain is 9% on the flexural modulus, 17% on the flexural strength and 14% on the strain to failure. PA66-i-GF35 samples that have absorbed water have also their mechanical properties improved. Compared to PA66-i-GF35 dry as moulded samples, the gain is 5% on the flexural modulus, 13% on the flexural strength and 16% on the strain to failure.

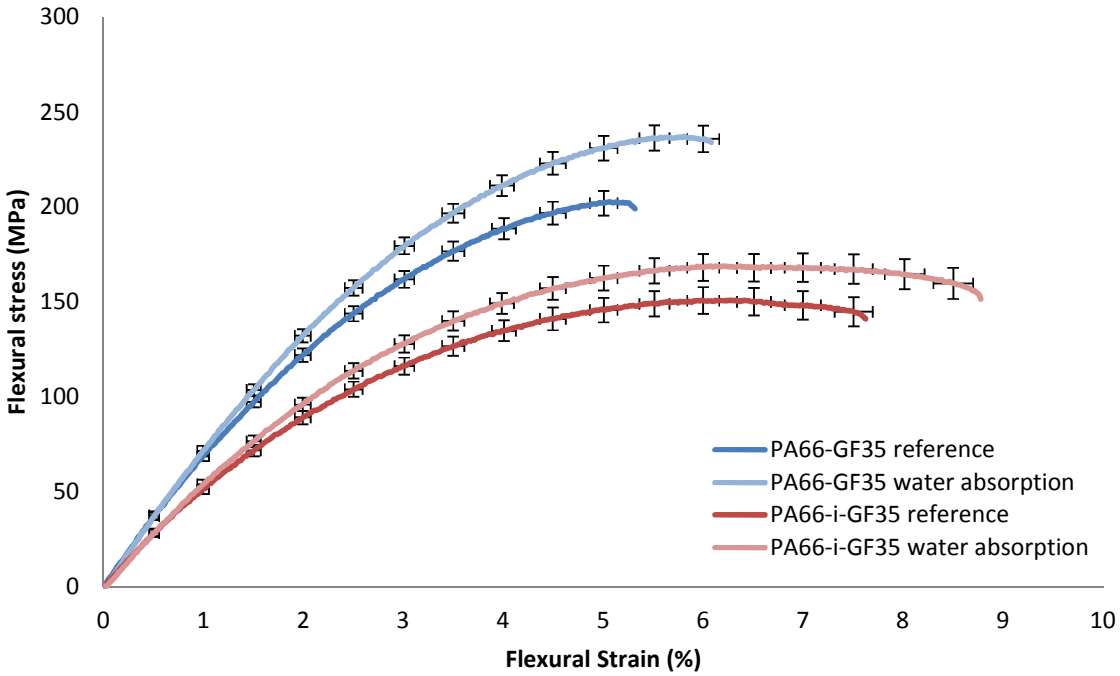

Figure 20 - Flexural stress-strain relations up to breaking point in dry as moulded and water uptake conditions (with standard deviation)

Table 13 summarises the flexural mechanical properties of PA66-GF35 and PA66-i-GF35 in dry as moulded and water uptake conditions.

Table 13 - Flexural mechanical properties in dry as moulded and water uptake conditions after 3000 hours

Properties/ Materials	PA66-GF35 reference	PA66-GF35 water uptake	PA66-i-GF35 reference	PA66-i-GF35 water uptake
Flexural modulus (MPa)	7218	7880	5823	6105
Maximum flexural stress (MPa)	202	236	150	169
Maximum strain to failure (%)	5.27	6.02	7.56	8.77

Effect of aqueous $CaCl_2$ uptake

Figure 21 shows the tensile load versus the extension for materials PA66-GF35 and PA66-i-GF35 when dry as moulded and after aqueous calcium chloride uptake. These data are collected directly from the testing machine. PA66-GF35 tensile samples that have been subjected to aqueous calcium chloride uptake have undergone a maximum tension force of 5.8 kN and extended by 6.1 mm. Compared to PA66-GF35 in dry as moulded condition that is a loss of 21% of strength but a gain of 17% of extension. PA66-i-GF35 tensile samples that have been subjected to aqueous calcium chloride uptake have undergone a maximum tension force of 4.4 kN and extended by 9.8 mm. Compared to PA66-i-GF35 in dry as moulded condition that is a loss of 18% of strength but a gain of 38% of extension. In both materials, PA66-GF35 and PA66-i-GF35, the aqueous calcium chloride uptake affects the strength in tension but increases the elongation. PA66-GF35 seems to be slightly more affected by the aqueous calcium chloride uptake than PA66-i-GF35.

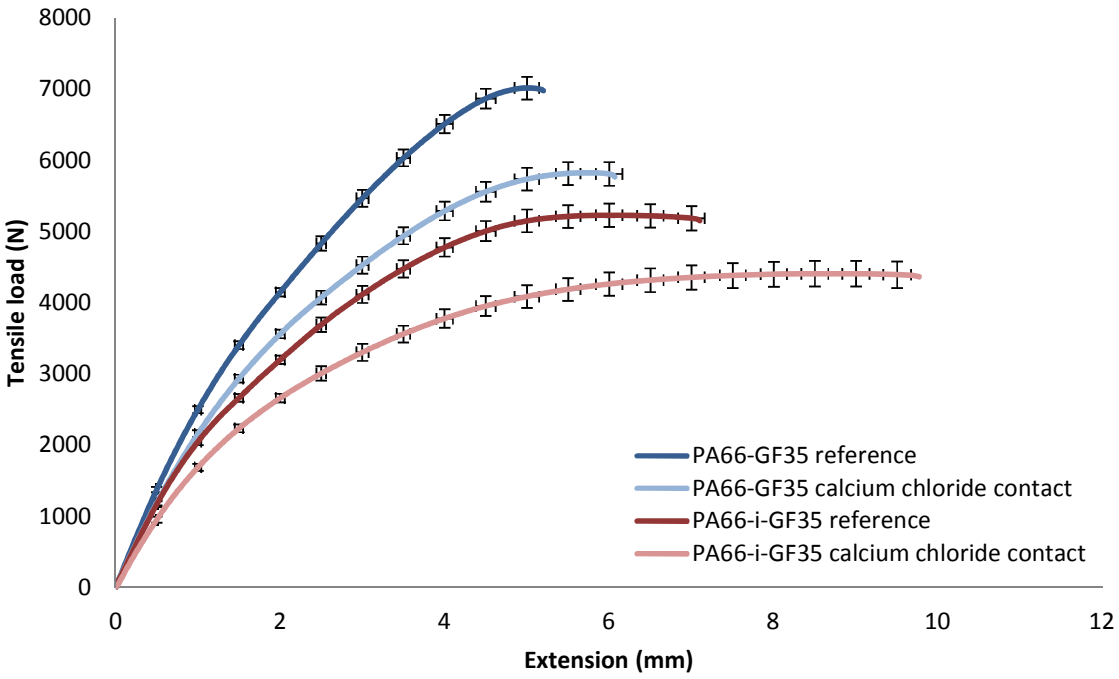

Figure 21 - Tensile load versus extension up to breaking point in dry as moulded and aqueous $CaCl_2$ uptake conditions (with standard deviation)

Figure 22 shows the flexural load versus the deflection for materials PA66-GF354 and PA66-i-GF35. These data are collected directly from the testing machine. PA66-GF35 flexural samples that have been subjected to aqueous calcium chloride uptake have undergone a maximum flexural force of 370 N and deflected by 9.8 mm. Compared to PA66-GF35 in dry as moulded condition that is a gain of 9% of strength and 8% of deflection. PA66-i-GF35 flexural samples that have been subjected to aqueous calcium chloride uptake have undergone a maximum flexural force of 275 N and

deflected by 14.1 mm. Compared to PA66-i-GF35 in dry as moulded condition that is a gain of 10% of strength and 8% of deflection. In both materials, PA66-GF35 and PA66-i-GF35, the aqueous calcium chloride uptake increases the strength in flexion and the deflection.

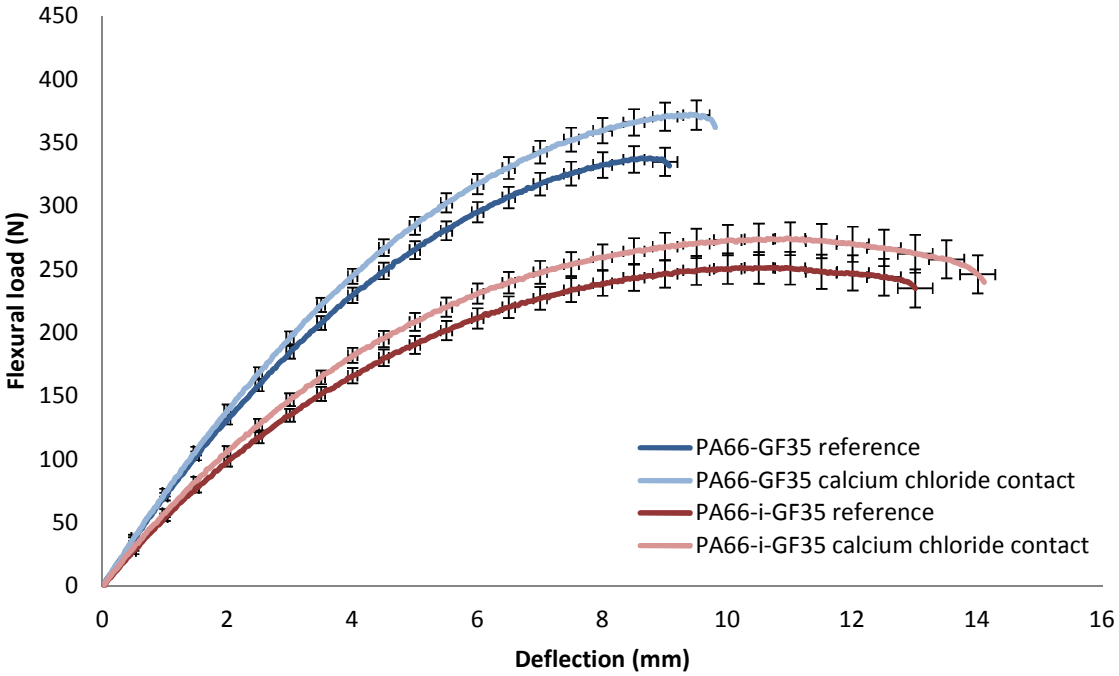

Figure 22 - Flexural load versus deflection up to breaking point in dry as moulded and aqueous $CaCl_2$ uptake conditions (with standard deviation)

Figure 23 shows the stress-strain relations of PA66-GF35 and PA66-i-GF35 when dry as moulded and after aqueous calcium chloride uptake in tension stress conditions. These relations are calculated from the tensile load and extension of Figure 21. PA66-GF35 samples that have absorbed the aqueous mixture with calcium chloride are affected in their Young's modulus

and tensile strengths. Compared to PA66-GF35 dry as moulded samples, the loss is 17% on the Young's modulus and 21% on the tensile strength. However, there is a gain in their strain to failure of 16%. PA66-i-GF35 samples that have absorbed the aqueous mixture with calcium chloride are also affected in their Young's modulus and tensile strengths. Compared to PA66-i-GF35 dry as moulded samples, the loss is 20% on the Young's modulus and 19% on the tensile strength. On the other hand, there is a gain in their strain to failure of 37%.

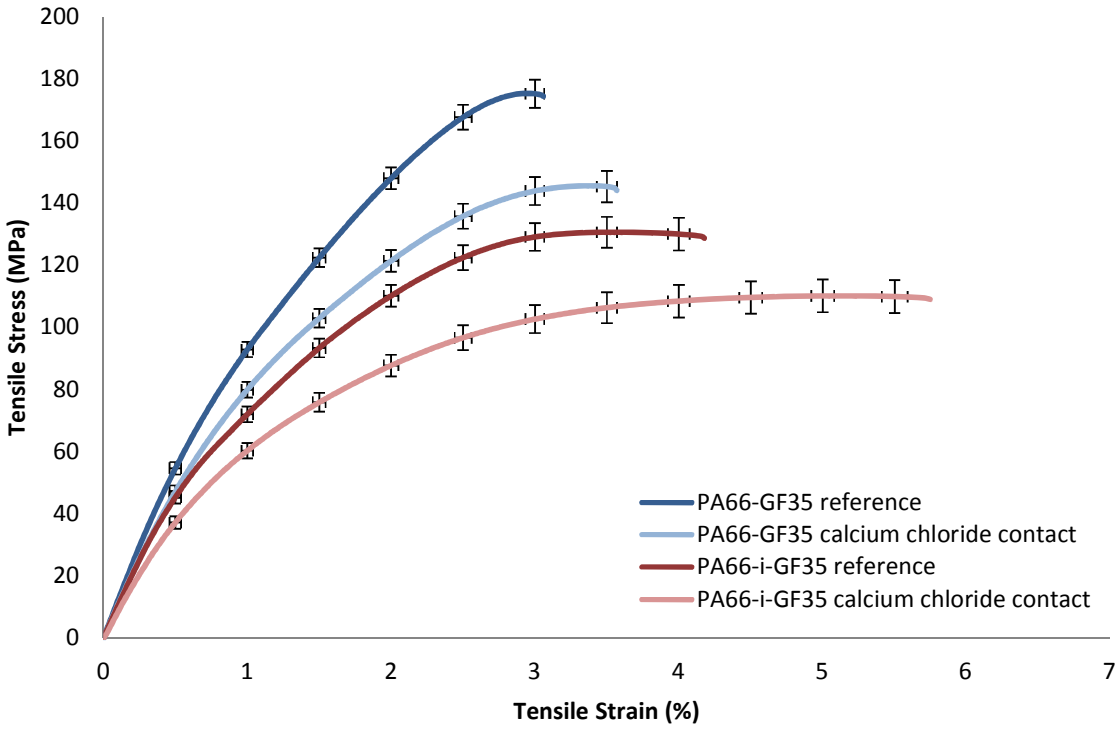

Figure 23 - Tensile stress-strain relations up to breaking point in dry as moulded and aqueous $CaCl_2$ uptake conditions (with standard deviation)

Table 14 summarises the tensile mechanical properties of PA66-GF35 and PA66-i-GF35 in dry as moulded and aqueous calcium chloride uptake conditions.

Table 14 - Tensile mechanical properties in dry as moulded and aqueous $CaCl_2$ uptake conditions after 3000 hours

Properties/ Materials	PA66-GF35 reference	PA66-GF35 aqueous salt uptake	PA66-i-GF35 reference	PA66-i-GF35 aqueous salt uptake
Young's modulus (MPa)	11848	10106	9950	8315
Maximum tensile stress (MPa)	175	145	131	110
Maximum strain to failure (%)	3.05	3.53	4.16	5.71

Figure 24 shows the stress-strain relations of PA66-GF35 and PA66-i-GF35 when dry as moulded and after aqueous calcium chloride uptake in flexion stress conditions. These relations are calculated from the flexural load and deflection of Figure 22. PA66-GF35 samples that have absorbed the aqueous mixture with calcium chloride have their mechanical properties improved. Compared to PA66-GF35 dry as moulded samples, the gain is 9% on the flexural modulus, 10% on the flexural strength and 9% on the strain to failure. PA66-i-GF35 samples that have absorbed the aqueous mixture with calcium chloride have also their mechanical properties improved. Compared to PA66-i-GF35 dry as moulded samples, the gain is 9% on the flexural modulus, 9% on the flexural strength and 10% on the strain to failure.

Table 15 summarises the flexural mechanical properties of PA66-GF35 and PA66-i-GF35 in dry as moulded and aqueous calcium chloride uptake conditions.

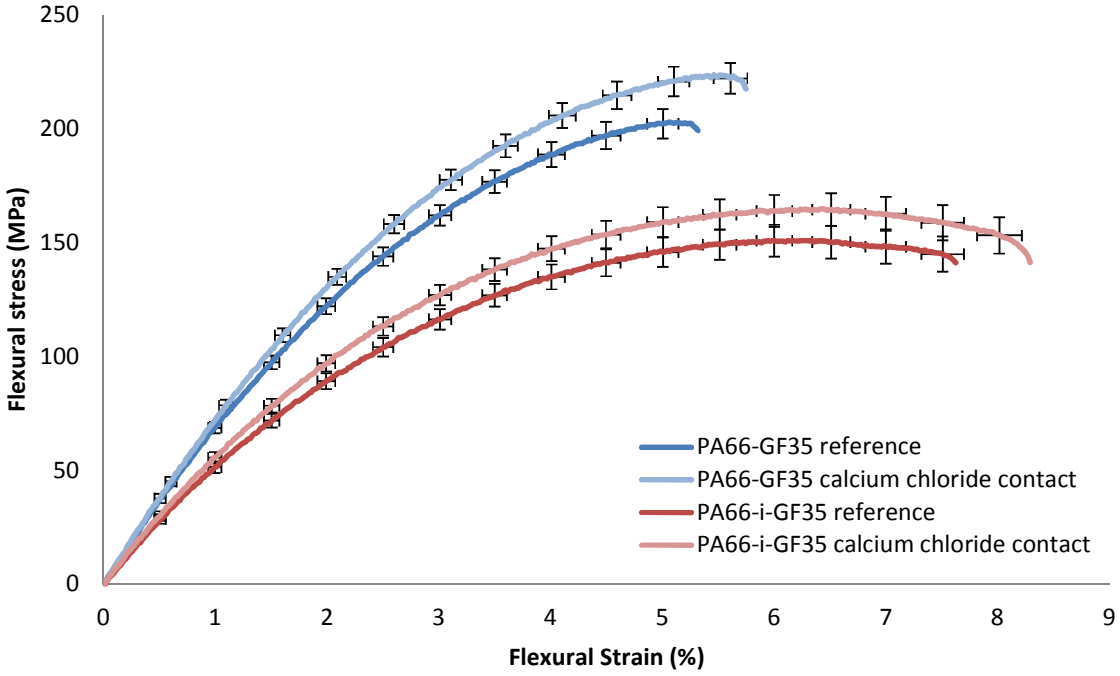

Figure 24 - Flexural stress-strain relations up to breaking point in dry as moulded and aqueous $CaCl_2$ uptake conditions (with standard deviation)

Table 15 - Flexural mechanical properties in dry as moulded and aqueous $CaCl_2$ uptake conditions after 3000 hours

Properties/ Materials	PA66-GF35 reference	PA66-GF35 aqueous salt uptake	PA66-i-GF35 reference	PA66-i-GF35 aqueous salt uptake
Flexural modulus (MPa)	7218	7867	5823	6330
Maximum flexural stress (MPa)	202	223	150	164
Maximum strain to failure (%)	5.27	5.72	7.56	8.28

4.3.2. Dynamic tests

Effect of water uptake

Table 16 shows the Charpy impact strength for PA66-GF35 and PA66-i-GF35 subjected to water uptake and compares them to those in dry as moulded condition. The Charpy test is conducted to determine the Charpy impact strength of PA66-GF35 and PA66-i-GF35 subjected to water uptake. All the tests led to a complete break, in which the samples are separated into two pieces. The type of failure observed is a tension failure where the opposite side of impact fails first. Both materials break in two ways. On the tension side, the breakage has jagged edges, shear lips typical of a ductile fracture. On the compression side, the breakage is on flat plane characteristic to a brittle fracture.

Table 16 - Charpy impact strength in dry as moulded and water uptake conditions

Materials	Energy absorbed (J)	Impact strength (kJ/m^2)
PA66-GF35 reference	4.14	103.38
PA66-GF35 water uptake	4.20	105.07
PA66-i-GF35 reference	4.07	101.69
PA66-i-GF35 water uptake	4.20	105.07

Figure 25 and Figure 26 show the lower and upper limit of impact energy resistance of PA66-GF35 and PA66-i-GF35 subjected to water uptake. This also allows the assessment of the maximum impact strength to

failure for each material. PA66-GF35 samples fail between 2.5 and 3 J. The maximum deflection prior to failure is around 1.1 mm (27.5%), and the maximum force prior to failure is around 1260 N. PA66-i-GF35 samples fail between 3.5 and 4 J. The maximum force before showing a sign of weakness is around 1140 N after 1.14 mm deflection (28.5%). The drop is not huge only by 60 N but enough to display at tiny crack (1 mm line). All materials start to deflect at just above 900 N. PA66-i-GF35 has slightly lower impact strength than PA66-GF35 but in return it deflects more before the first failure.

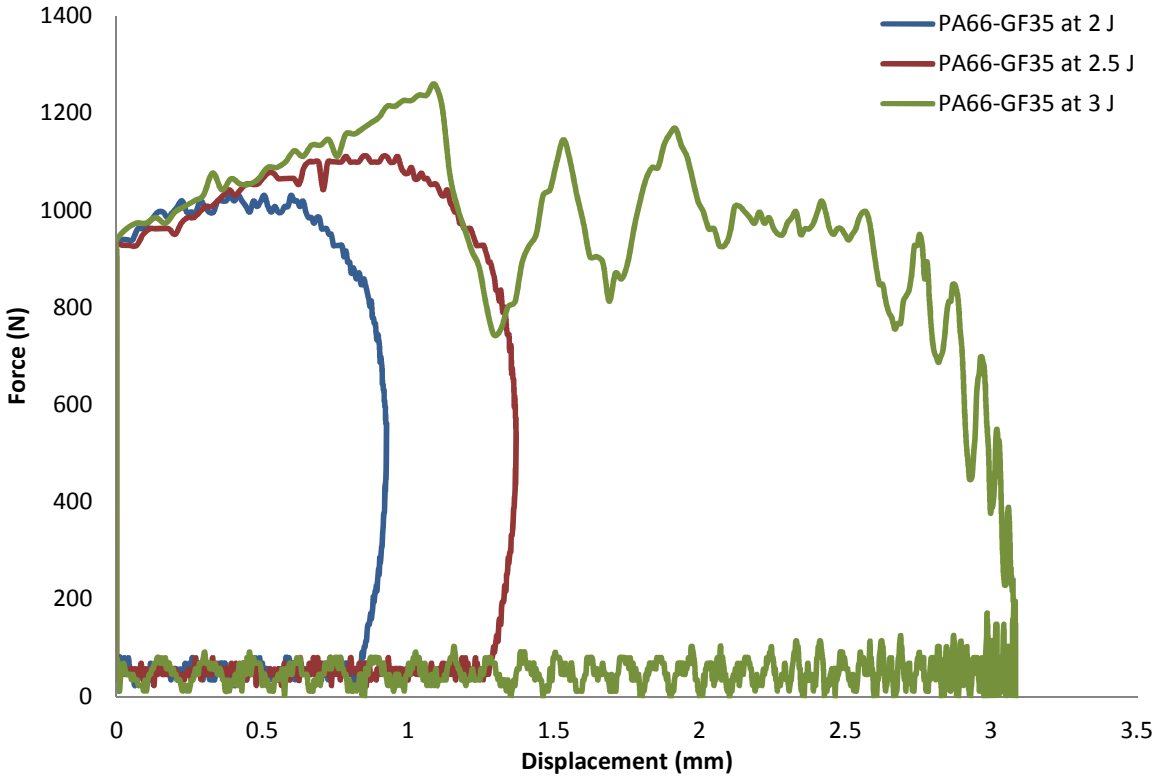

Figure 25 - PA66-GF35 subjected to water uptake impacted at 2, 2.5 and 3 J

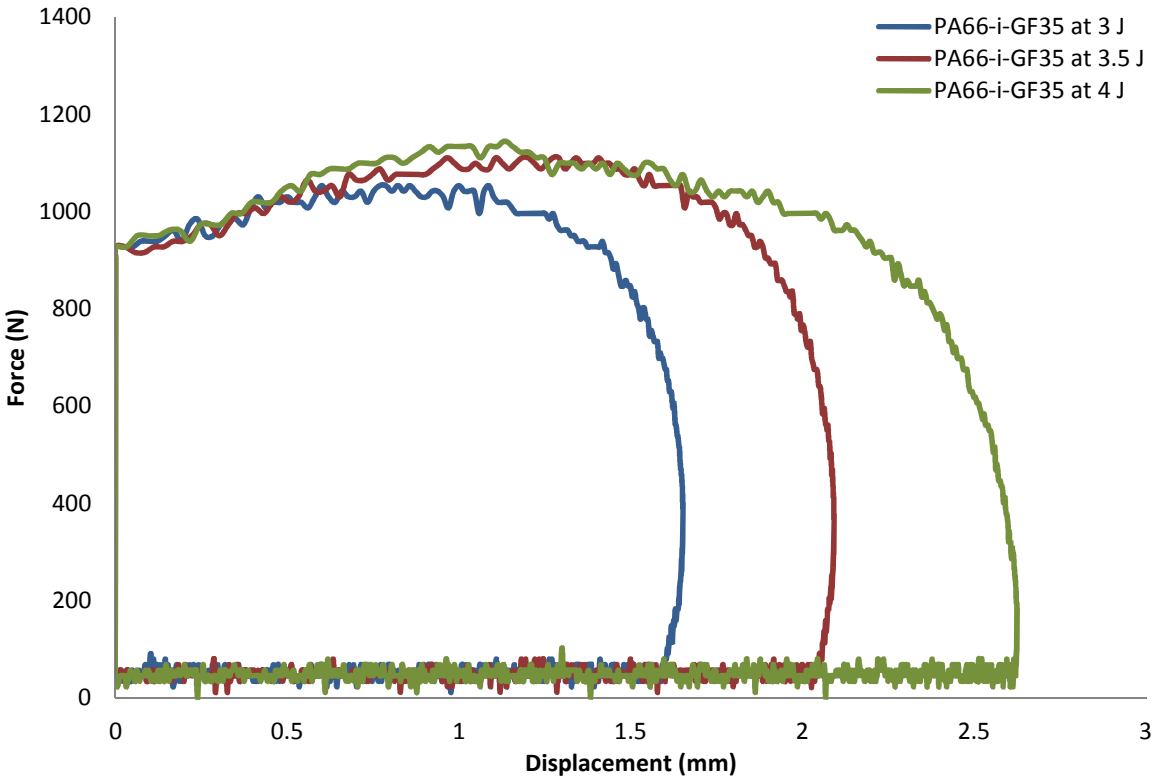

Figure 26 - PA66-i-GF35 subjected to water uptake impacted at 2, 2.5 and 3 J

Figure 27 compares both materials at 3 J subjected to water uptake showing their differences in terms of impact resistance and behaviour. PA66-GF35 fails at 1260 N after a 1.1 mm deflection (27.5%). Its resistance drops to 740 N, which accelerate the damage and the deflection up to 3.09 mm (77%). Nonetheless, the PA66-GF35 plates recover their initial positions after the impact. On the other hand, PA66-i-GF35 withstands the impact despite starting to deflect at the same force and displaying a lower strength. At the end, its deflection is lower and reaches 1.65 mm (41%).

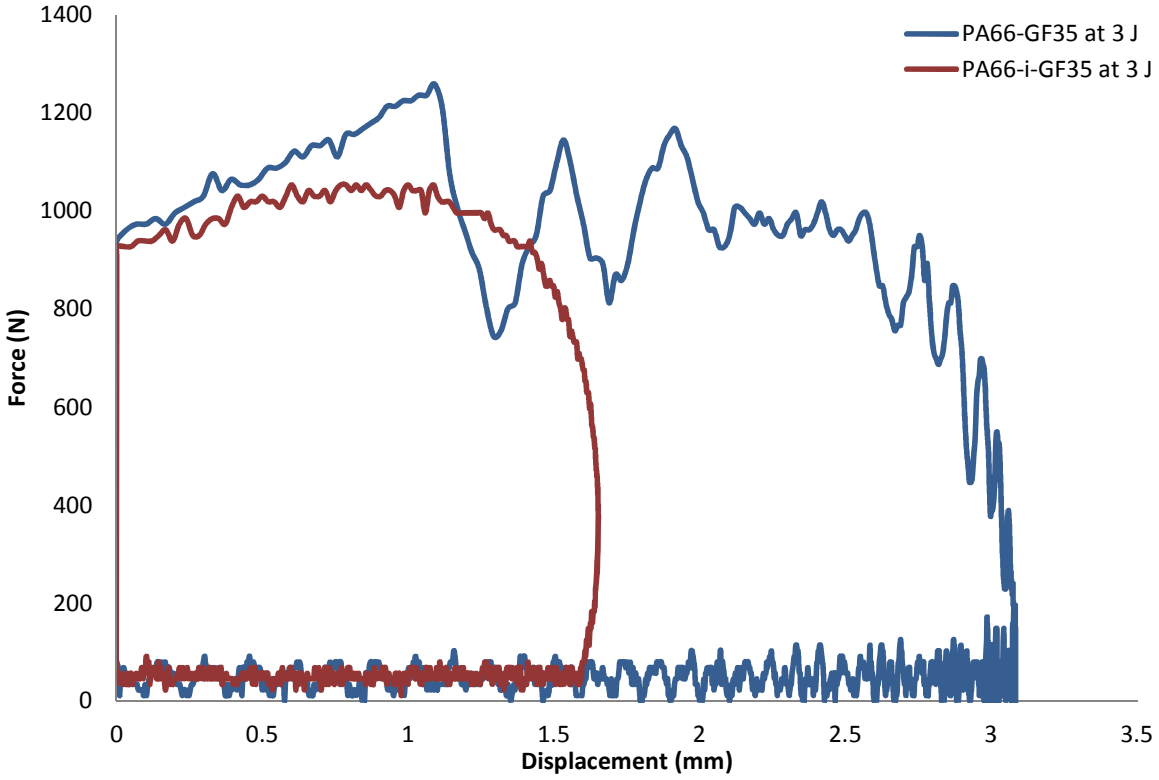

Figure 27 - PA66-GF35 and PA66-i-GF35 subjected to water uptake impacted at 3 J

Table 17 presents the impact energies and their corresponding velocities to which PA66-GF35 and PA66-i-GF35 plates exposed to water uptake were subjected by the air gun impact tester. Table 18 provides the assessment of their damage, post-impact, characterized by the shape and the size of the failure. PA66-GF35 plates fail at 3.66 J (18.25 m/s) whereas PA66-i-GF35 plates survived the same impact (3.67 J – 18.27 m/s). PA66-i-GF35 fails at 4.08 J (19.25 m/s). PA66-i-GF35 is then slightly more impact resistant than PA66-GF35. The major difference becomes obvious when

comparing the scale and the shape of the failure and this is verified up to 6.5 J or 24.31 m/s. PA66-GF35 tends to fail with a Y-shaped crack whereas PA66-i-GF35 fails with a linear crack. The scale of the damage increases with the energy but it is a lot more pronounced for PA66-GF35 than PA66-i-GF35.

Table 17 - Gas gun impacts on plates subjected to water uptake condition

Sample ID test	Kinetic Energy (J)	Velocity (m/s)	Result
PA66-GF35_w1	2.16	14.00	OK
PA66-GF35_w2	3.66	18.25	Crack_w1
PA66-GF35_w3	4.20	19.53	Crack_w2
PA66-GF35_w4	4.35	19.89	Crack_w4
PA66-GF35_w5	5.92	23.20	Crack_w6
Sample ID test	Kinetic Energy (J)	Velocity (m/s)	Result
PA66-i-GF35_w1	2.05	13.64	OK
PA66-i-GF35_w2	3.67	18.27	OK
PA66-i-GF35_w3	4.08	19.25	Crack_w3
PA66-i-GF35_w4	4.96	21.23	Crack_w5
PA66-i-GF35_w5	6.24	23.82	Crack_w7

Table 18 - Damage assessment on gas gun impacted plates subjected to water uptake condition

Crack ID	Size (mm)	Shape
Crack_w1	19*19	Y
Crack_w2	22*21	Y
Crack_w3	3	I
Crack_w4	24*22	Y
Crack_w5	18	I
Crack_w6	29*23	Y
Crack_w7	19	I

Effect of aqueous $CaCl_2$ uptake

Table 19 shows the Charpy impact strength for PA66-GF35 and PA66-i-GF35 subjected to aqueous calcium chloride uptake and compares them to those in dry as moulded condition. The Charpy test is conducted to determine the Charpy impact strength of PA66-GF35 and PA66-i-GF35 subjected to aqueous calcium chloride uptake. All the tests led to a complete break, in which the samples are separated into two pieces. The type of failure observed is a tension failure where the opposite side of impact fails first. Both materials break in two ways. On the tension side, the breakage has jagged edges, shear lips typical of a ductile fracture. On the compression side, the breakage is on flat plane characteristic to a brittle fracture

Table 19 - Charpy impact strength in dry as moulded and aqueous $CaCl_2$ uptake conditions

Materials	Energy absorbed (J)	Impact strength (kJ/m^2)
PA66-GF35 reference	4.14	103.38
PA66-GF35 aq. $CaCl_2$ uptake	4.20	105.07
PA66-i-GF35 reference	4.07	101.69
PA66-i-GF35 aq. $CaCl_2$ uptake	3.93	98.30

Figure 28 and Figure 29 show the lower and upper limit of impact energy resistance of PA66-GF35 and PA66-i-GF35 subjected to aqueous calcium chloride uptake. This also allows the assessment of the maximum impact strength to failure for each material. PA66-GF35 samples fail between 3 and 3.5 J. The maximum deflection prior to failure is around 1.14 mm (28.5%), and the maximum force prior to failure is between 1360 and

1480 N. PA66-i-GF35 samples fail between 3 and 3.5 J. The maximum force before showing a sign of weakness is between 1180 and 1200 N after 1.05 mm deflection (26.3%). The drop is not obvious in that area, the material resistance fluctuates by 80 N but it is enough to display at tiny crack (1 mm line). All materials start to deflect at just above 900 N.

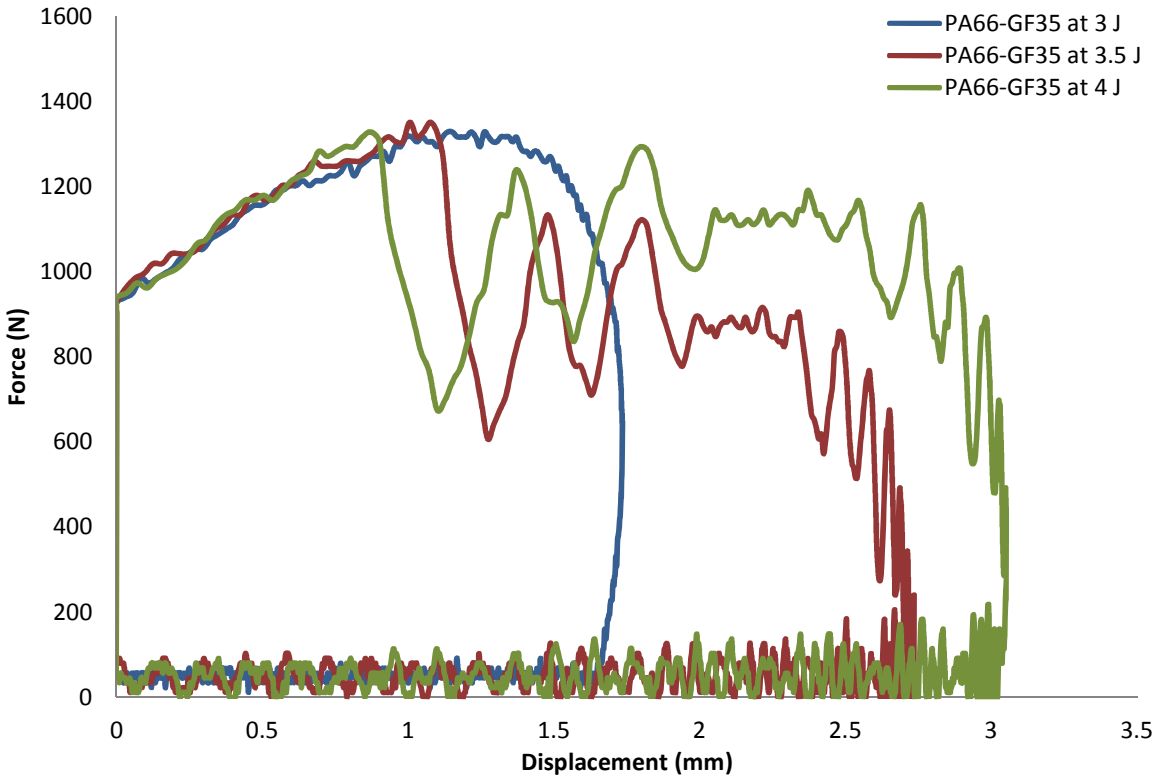

Figure 28 - PA66-GF35 subjected to aqueous $CaCl_2$ uptake condition impacted at 3, 3.5 and 4 J

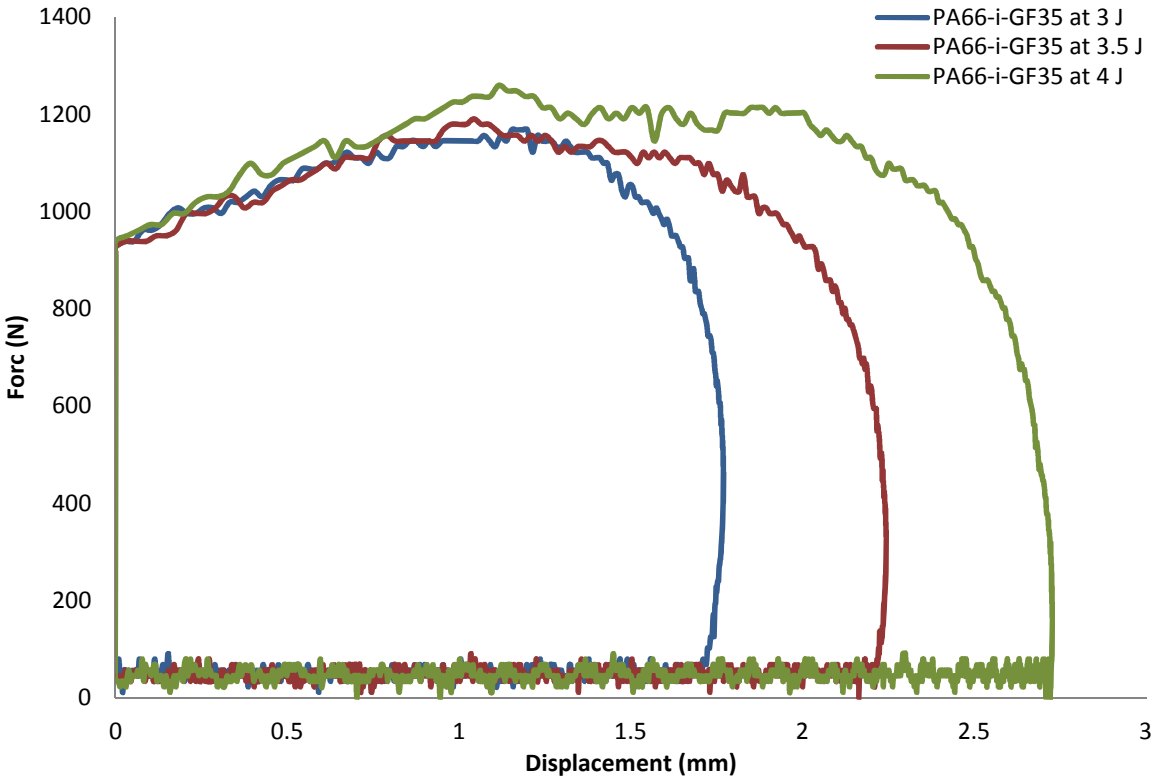

Figure 29 - PA66-i-GF35 subjected to aqueous $CaCl_2$ uptake condition impacted at 3, 3.5 and 4 J

Figure 30 compares both materials at 3 J subjected to aqueous calcium chloride uptake showing their differences in terms of impact resistance and behaviour. At 3 J, PA66-GF35 and PA66-i-GF35 withstood and survived the impact but each in a different way. PA66-GF35 has higher impact strength than PA66-i-GF35, respectively 1320 and 1180 N. In return, PA66-i-GF35 deflects slightly more than PA66-GF35, respectively 1.76 and 1.73 mm.

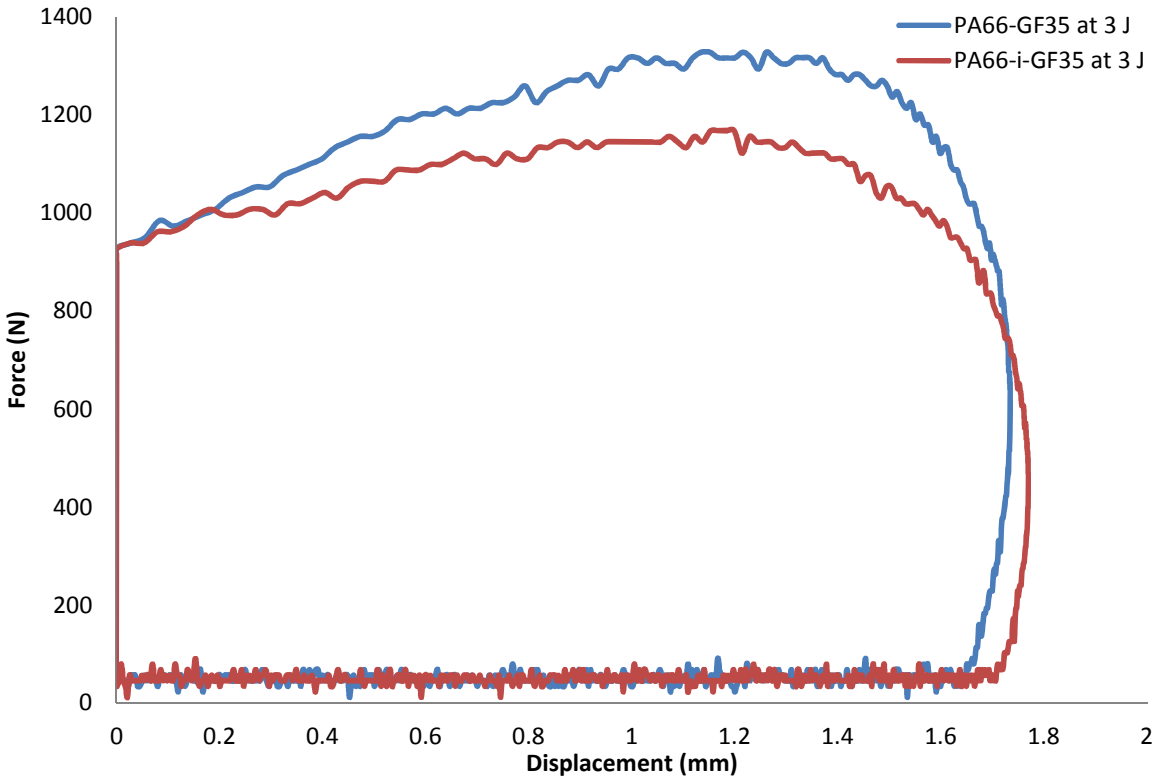

Figure 30 - PA66-GF35 and PA66-i-GF35 subjected to aqueous $CaCl_2$ uptake condition impacted at 3 J

Table 20 presents the impact energies and their corresponding velocities to which PA66-GF35 and PA66-i-GF35 plates exposed to aqueous calcium chloride uptake were subjected by the air gun impact tester. Table 21 provides the assessment of their damage, post-impact, characterised by the shape and the size of the failure. PA66-GF35 and PA66-i-GF35 plates fail between 3.66 and 4.20 J corresponding to a velocity of 18.25 to 19.53 m/s. At first sight, there is no distinction between them. However, the major difference comes from the scale and the shape of the failure and this is verified up to 6.5 J or 24.31 m/s. PA66-GF35 tends to fail with a cross-

shaped crack whereas PA66-i-GF35 fails with a linear crack. The scale of the damage increases with the energy but it is more pronounced for PA66-GF35 than PA66-i-GF35.

Table 20 - Gas gun impacts on plates subjected to aqueous $CaCl_2$ uptake condition

Sample ID test	Kinetic Energy (J)	Velocity (m/s)	Result
PA66-GF35_s1	2.10	13.82	OK
PA66-GF35_s2	3.56	18.99	OK
PA66-GF35_s5	4.18	19.49	Crack_s1
PA66-GF35_s4	4.32	19.81	Crack_s3
PA66-GF35_s3	5.96	23.28	Crack_s5
Sample ID test	Kinetic Energy (J)	Velocity (m/s)	Result
PA66-i-GF35_s1	2.11	13.85	OK
PA66-i-GF35_s2	3.69	18.32	OK
PA66-i-GF35_s5	4.05	19.19	Crack_s2
PA66-i-GF35_s4	4.92	21.15	Crack_s4
PA66-i-GF35_s3	6.15	23.65	Crack_s6

Table 21 - Damage assessment on gas gun impacted plates subjected to aqueous $CaCl_2$ uptake condition

Crack ID	Size (mm)	Shape
Crack_s1	22*21	X
Crack_s2	12	I
Crack_s3	26*21	X
Crack_s4	14	I
Crack_s5	29*23	X
Crack_s6	15	I

4.4. Conclusions

In this study, glass reinforced polyamide 66 (PA66-GF35) and rubber toughened glass reinforced polyamide 66 (PA66-i-GF35) subjected to water and aqueous $CaCl_2$ were examined in terms of tensile, flexion properties and impact strength.

Water uptake led to an increase of mass of 3% in each material. The absorption of water affects the tensile properties of both material, lowering Young's modulus and reducing strength by 45% for PA66-GF35, a little less for the rubber toughened PA66-i-GF35 by 40%. On the other hand, the elongation in tension is increased in both materials by 40%. The flexural properties are also changed with increased modulus, increased strength by 15% in all materials and deflection by 10% for PA66-GF35 and 15% for PA66-i-GF35. In comparison, the water uptake affects all material in the same proportion, with PA66-i-GF35 still more ductile and less stiff than PA66-GF35. Impacts on PA66-GF35 plates have shown that the material has lower impact strength. Moreover, the failure occurred at lower impact energy than compared to when it is dry when impacted with a projectile. PA66-i-GF35 has its impact strength increased with an improved impact resistance benefiting from a larger plastic deformation and above the failure threshold the extent of the damage is reduced.

Aqueous calcium chloride uptake led to an increase of mass of 1.6% for PA66-GF35 and 1.4%for the rubber toughened PA66-i-GF35. The tensile properties and flexural properties are affected in the same way as when subjected to water absorption. In tension, Young's modulus is lowered and strength is reduced by 20% but the extension is increased by 20% for PA66-GF35 and 40% for PA66-i-GF35. Flexural modulus is increased and so is strength augmented by 10% and deflection by 8% in both materials. The

Charpy tests show that PA66-i-GF35 is affected by the calcium chloride with lowered impact strength whilst PA66-GF35 has similar impact strength compared when subjected to water uptake only. However, when the impact is localised, the outcomes are different. PA66-i-GF35 compared to when it is saturated with water has slightly higher impact strength and deflects more for similar impact energy. Meanwhile, it reaches its failure threshold sooner. Compared when saturated with water, PA66-GF35 has better impact resistance. Nevertheless, subjected to the same conditions PA66-i-GF35 has in overall a better impact resistance and a greater deflection compared to PA66-GF35.

The effect of water and aqueous calcium chloride uptakes are similar. The water is not only absorbed and diffused into the material but it also plasticises the matrix [98]. The aqueous calcium chloride plasticises the matrix as well because of the aqueous solution but at the same time this process enters in competition with the complexation of the calcium chloride with the polymer [107] that induces the crazing of the matrix [108]. This was found when observing the shape and size of the cracks between each sample. The cracks in the aqueous calcium chloride treated samples are more radially dispersed with the material being even less homogeneous.

Chapter 5. Influence of temperature on mechanical properties of short glass fibre reinforced polyamide 6/66s

5.1. Introduction

The properties of thermoplastics are temperature dependent due to the fact that they are soft when heated and hard when cooled [110]. The increase of temperature reduces the Young's modulus and tensile strength but increases the failure strain leading to a material more ductile and less stiff [5; 64]. Thomason [61] found that additional energy dissipation mechanisms are activated thanks to the addition of fibres. Lhymn et al. [43] and Chevali et al. [110] mentioned that the moisture absorption can also be increased with the temperature [43; 110]. On the other hand, the effect of thermal ageing on unreinforced and glass reinforced polyamide 66 was reported by Eriksson et al. [41] and Rudzinski et al. [111] to cause oxidative degradation on the surface region resulting in a decreased elongation at break and embrittlement of the material. Of particular concern are the under-the-hood thermoplastics parts that are required to be functional at elevated temperatures (around 80°C) encountered in and around the engine. The thermoplastic oil pan is subjected to the heat created by the engine which is transferred via its connection by contact, the circulating oil and the surrounding air.

5.2. Experimental testing

5.2.1. Materials

Materials used in this study are the two materials outlined in the previous chapter PA66-GF35 and PA66-i-GF35, refer to section 3.2.1. Another material is also studied: Ultramid B3ZG8 which is a rubber modified SGFR Polyamide 6 with 35 wt% of fibre and manufactured by Basf (data sheet available in Appendix 3). This material is henceforth named PA6-i-GF35. PA6-i-GF35 was used in some experiments and compared against PA66-GF35 when PA66-i-GF35 was not yet available. PA66-GF35 and PA66-i-GF35 are based on the same polymer PA66 but the latter is rubber toughened. PA6-i-GF35 is based on another polyamide, PA6, and is rubber toughened as well. For more information on the rubber toughened material to improve impact resistance, refer to section 3.2.1. Finally, pieces are then cut off from the ribbing of each oil pan to make test samples.

5.2.2. Characterisation

Two thermal analysis techniques were conducted:

The DSC (Differential Scanning Calorimetry) measures heat exchanges during physical transformations between a sample and a reference. The DSC

instrument used is a DSC 200 from NETZSCH. The temperature is linearly increased at a rate of 10°C per minute in a range from ambient to 300°C. The reference used is air, which has a constant heat capacity in the range of temperature studied. Analyses are performed under argon, an inert gas, to avoid any reaction of the sample with the atmosphere of the furnace. This test also determines the maximum operating temperature for each material.

The TGA (Thermogravimetric Analysis) measures mass variation of a sample which is linked to phase transitions and thermal degradation during a thermal cycle of heating. This test is performed to assess the temperature of decomposition and the rate of degradation of each sample. The TGA instrument used is a TG 209 from NETZSCH. The temperature is set at 30°C and then linearly increased by 10°C per minute until 610°C.

5.2.3. Ageing tests in oil and air

Ageing tests have been conducted in collaboration with industrialists (BASF and Eaton Corporation) to assess the heat ageing effect in oil and air [138]. Tensile samples of PA66-i-GF35 and PA6-i-GF35 were aged in chambers at 150°C immersed in oil (Shell Helix Plus SAE 5W-40) or at 150°C in air for a period of up to 3000 hours. Weekly, five tensile samples per conditions were taken off from their chambers and tensile tests were

performed as describe in section 3.2.2. Evolutions of tensile strength and tensile strain of each material were measured.

5.3. Finite element analysis

Low velocity impact tests were performed on 2D ribbed structure (11286 shells elements, 1 mm per element) to assess the impact performance of PA66-GF35 and PA6-i-GF35 with the influence of the temperature. The ribbed structure was constrained on its edges. The impact locations are on the ribs and between the ribs. PA6-i-GF35 is used instead of PA66-i-GF35 because of the available data under different temperatures and similar impact response. Therefore, the purpose of this study is to investigate the influence of the rubber modifier on the impact performance. Single impact tests are performed with a 10 mm diameter and 22 g projectile (defined as rigid part) shot at 90° to surface at 26 m/s so as to achieve the impact energy of 7.5 J. For more information on simulation settings, refer to section 3.2.2.

Figure 31 and Table 22 illustrate the temperature dependency of PA66-GF35 and PA6-i-GF35 and the stress-strain relations at -20°C, 23°C and 120°C implemented into the simulations.

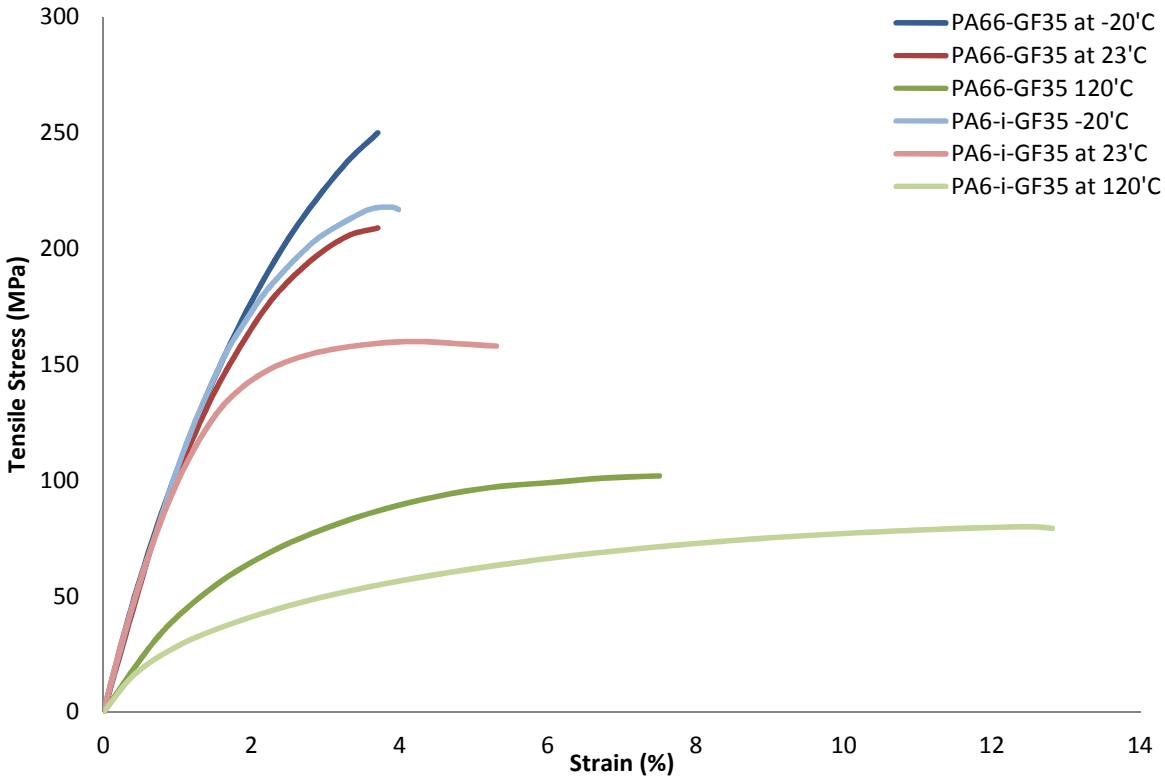

Figure 31 – Temperature dependency of tensile stress-strain relations up to breaking point of PA66-GF35 and PA6-i-GF35 [49]

Table 22 - Strain to failure PA66-GF35 and PA6-i-GF35 at -20, 23, 120°C [49]

Materials	Temperatures	Maximum Strain at Break (%)	Effective Plastic Strain at Break (%)
PA66-GF35	-20°C	4.1 at 262 MPa	1.64
PA6-i-GF35	-20°C	3.98 at 217 MPa	2.04
PA66-GF35	23°C	3.8 at 213 MPa	1.90
PA6-i-GF35	23°C	5.3 at 158 MPa	3.64
PA66-GF35	120°C	7.4 at 104 MPa	5.18
PA6-i-GF35	120°C	12.8 at 79.3 MPa	11.06

5.4. Results and discussion

5.4.1. DSC results

Figure 32 shows the DSC of PA66-GF35. The mass of the sample studied is 4.3 mg. The graph shows heat flow on the left and the variation of heat flow on the right versus the temperature. A negative peak related to an endothermic transition is observed at 260.9°C that corresponds to the temperature of fusion of the PA66-GF35 material. The peak begins at 234°C and finishes at 269°C. The integration of the area under the peak determines the enthalpy of this endothermic transition, $\Delta H_{PA66\text{-}GF35}$ = -45.16 J/g. This refers to the consumption of heat needed for the sample to melt. At 234°C, the organised structure of the sample starts to dislocate and the chains of polymers move about. From this point, the temperature of the sample will not increase further until all the organised areas have melted. That is the reason why at the same time, the variation of the heat flow fluctuates. Indeed, the DSC instrument has to keep up and maintain the temperature ramp set. A lot of heat is absorbed by the sample. After 269°C, less heat is required to increase the temperature of the sample and the variation of heat flow is back to null.

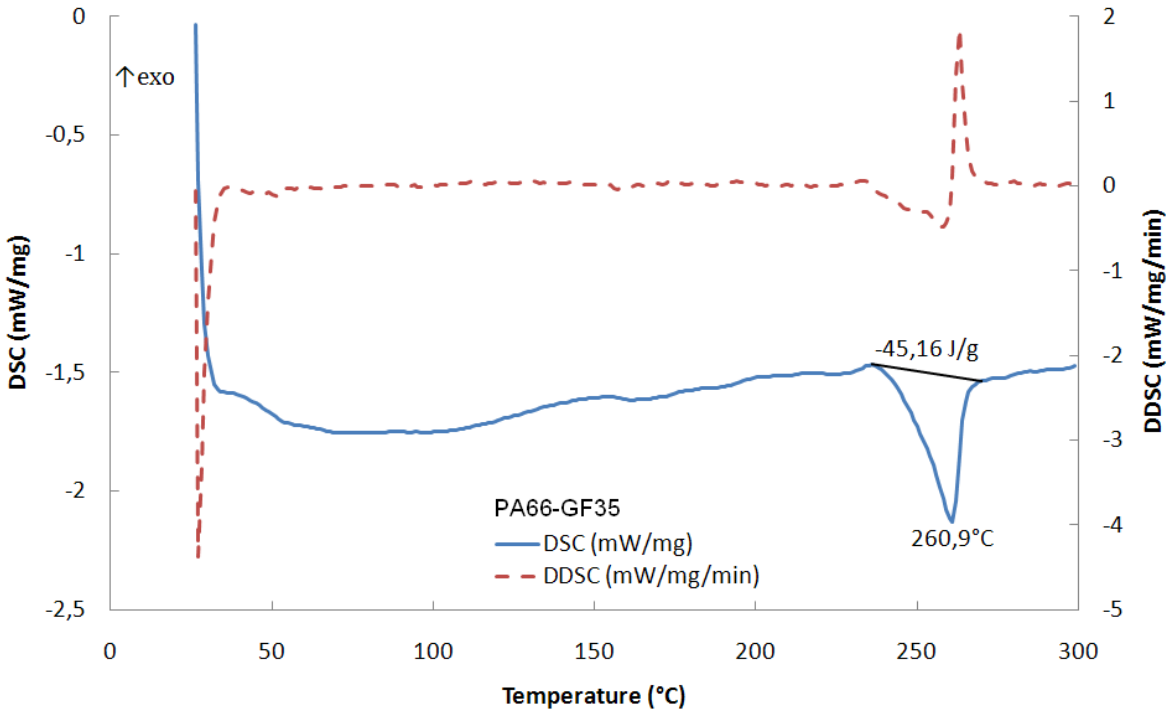

Figure 32 – DSC results of PA66-GF35

Figure 33 shows the DSC of PA66-i-GF35. The mass of the sample studied is 4.4 mg. In this analysis, the endothermic transition is characterised with two peaks. The main peak is at 258.1°C stretched from 230°C to 264°C followed by a small one at 268°C from 264°C to 274°C. The possible explanation is that two different entities have reached their melting points. The first peak is the melting transition of the polyamide polymer but the second peak could result from the melting point of the rubber additives or its effects. The curve of the variation of the heat flow helps us to spot changes of phases when matched with the heat flow curve. The enthalpy of the first transition is $\Delta H_{PA66\text{-}i\text{-}GF35}$ = -36.8 J/g.

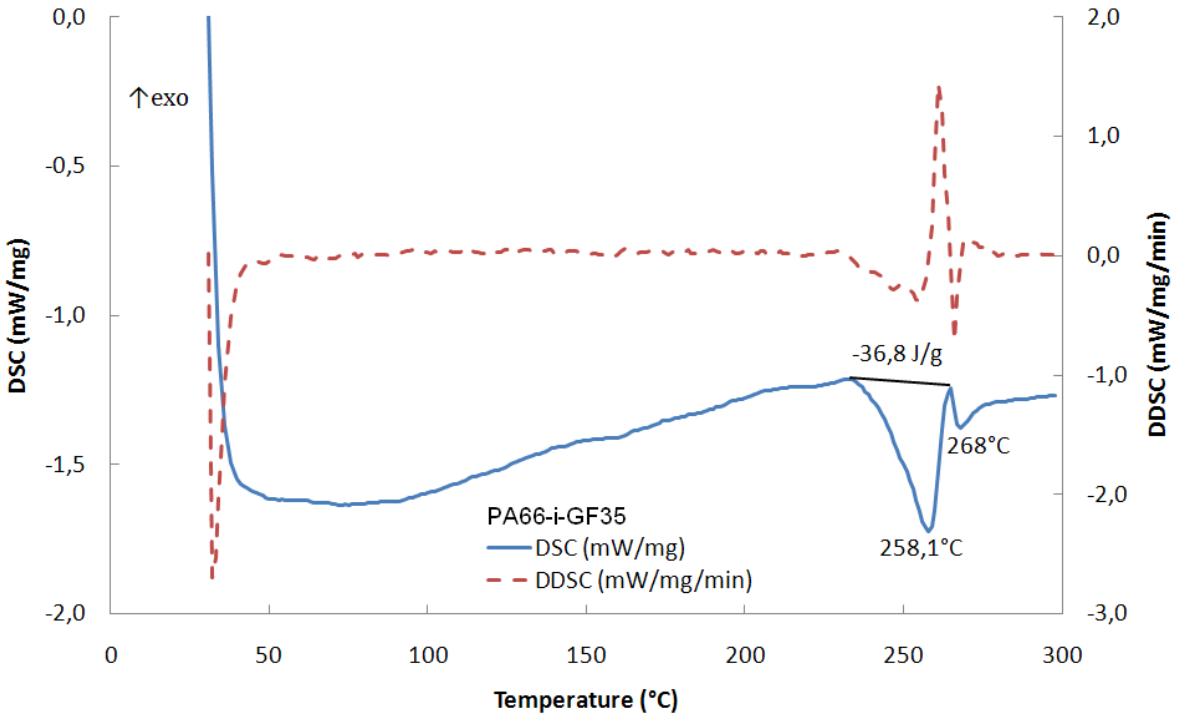

Figure 33 - DSC results of PA66-i-GF35

Figure 34 shows the DSC of PA6-i-GF35. The mass of the sample studied is 4.4 mg. PA6-i-GF35, like PA66-i-GF35, presents two peaks. The big peak from 191°C to 227°C has its maximum at 219.4°C. The second peak is detached from the first one, it is small and weaken from 238°C to 262°C and reaches its maximum at 249.4°C. A comparable statement as previously given can explain each peak. The enthalpy of the first transition is $\Delta H_{PA6\text{-}i\text{-}GF35}$ = -38.05 J/g and that is comparable to $\Delta H_{PA66\text{-}i\text{-}GF35}$.

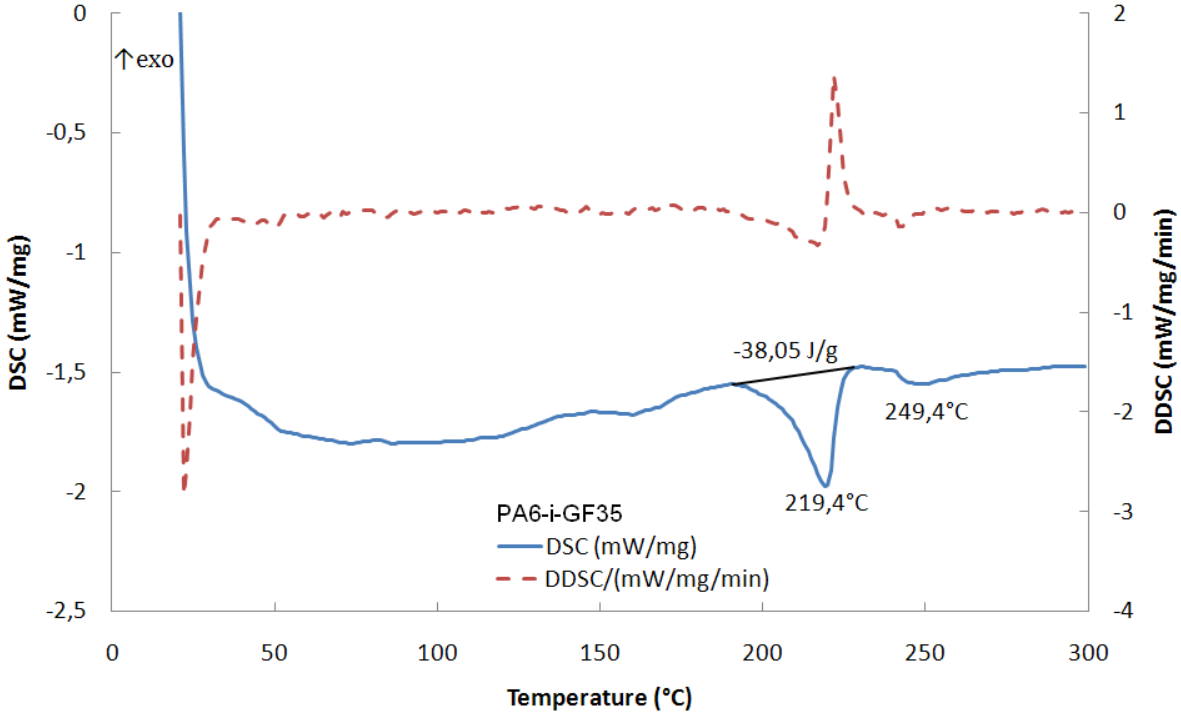

Figure 34 – DSC results of PA6-i-GF35

The difference between PA66-GF35 and PA66-i-GF35 is the rubber-based additive. These thermoplastics have the same PA66 polyamide grade which can be spotted by the similar peak at about 206°C. The PA66-i-GF35 and PA6-i-GF35 materials are respectively PA66 and PA6 polymers. Therefore their temperatures of fusion are different. However, the DSC graphs illustrate that they have practically the same enthalpy. Thus, the only correlation is the rubber content that levels this energy. The hypothesis is that the rubber additive spaces the polymer chains from each other by

getting in between them. The consequence is that the energy linking the chains is lowered. Table 23 compares relevant DSC data findings.

Table 23 - Material comparison of relevant DSC data

Materials	Literature values of melting point (°C) [49]	Recorded melting point (°C)	Enthalpy of fusion (J/g)	Glass transition (°C)
PA66-GF35	260	260.9	-45.16	155
PA66-i-GF35	260	258.1	-36.8	155
PA6-i-GF35	220	219.4	-38.05	155

These three materials exhibit a barely noticeable smooth glass transition at just about the same temperature of 155°C. However there is no distinctive sign of crystallisation peaks. All materials have faced a phase transition when heated which has changed their heat capacities (Table 24). The polymer in solid state has a lower heat capacity than when melted. That is to say with a minor elevation of the temperature, the polymer in a melted state absorbs more heat.

Table 24 - Specific heat capacities

Materials	Literature values of specific heat capacity (J) – endothermic [49]	Recorded data of specific heat capacity (J) - endothermic (Solid state - Melted state)
PA66-GF35	1500	1750 - 1470 average 1610
PA66-i-GF35	1500	1640 - 1220 average 1430
PA6-i-GF35	-	1790 - 1480 average 1635

5.4.2. TG results

Figure 35 shows the TG of PA66-GF35. The mass of the sample at the start is 5.1 mg. The graph illustrates the variation of mass in percentage on the left and its time derivative on the right. The increase of mass at the start may be a sign of oxidation that is translated as a gain of mass in the curve. The material at 270°C, which is over its melting point, has lost just 1% of its original mass. The temperature of degradation is reached at 446°C after having lost, since the beginning, 47% in mass and at 459°C it has lost 50% of its mass. Over 600°C, the mass seems to stabilise after 65.3% of mass lost.

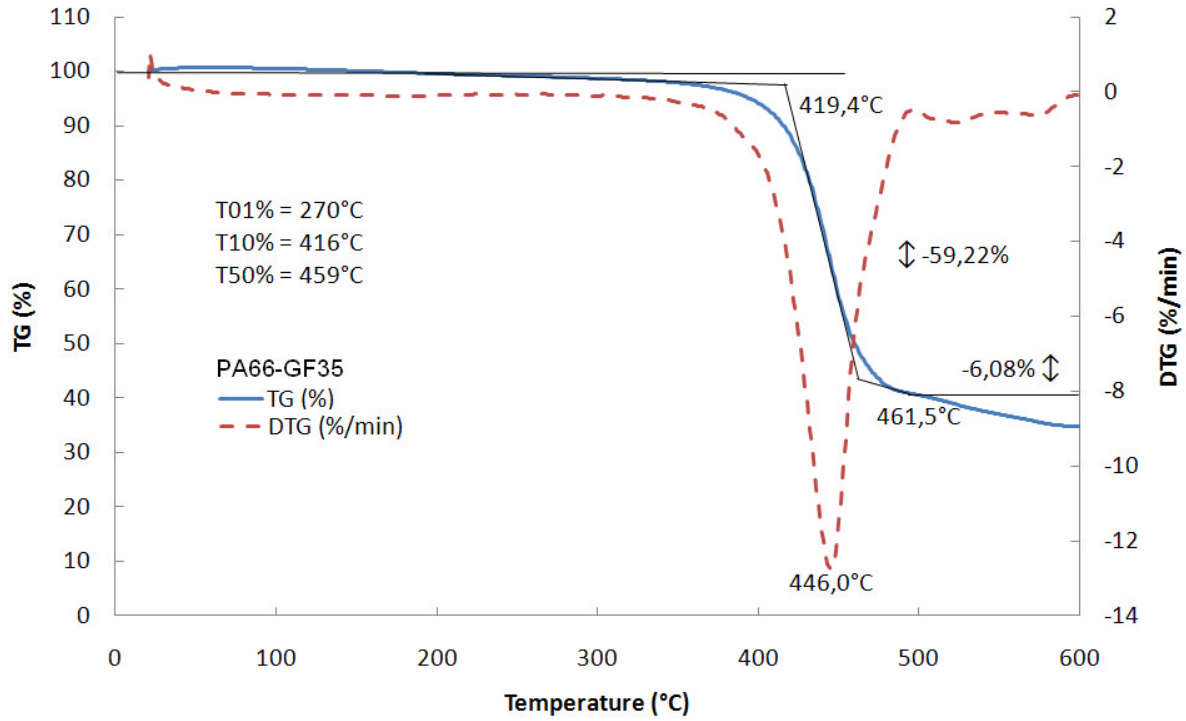

Figure 35 – TG results of PA66-GF35

Figure 36 shows the TG of PA66-i-GF35. The mass of the sample at the start is 5.1 mg. The same comment can be used concerning the increase of mass at the beginning as a sign of oxidation. The material at 221°C has lost 1% of its original mass. The temperature of degradation is reached at 444.3°C after having lost, since the beginning, 33% in mass and at 467°C it has lost 50% of its mass. Over 600°C, the mass does not seem to stabilise but the rate of mass lost decreases after 68.3%.

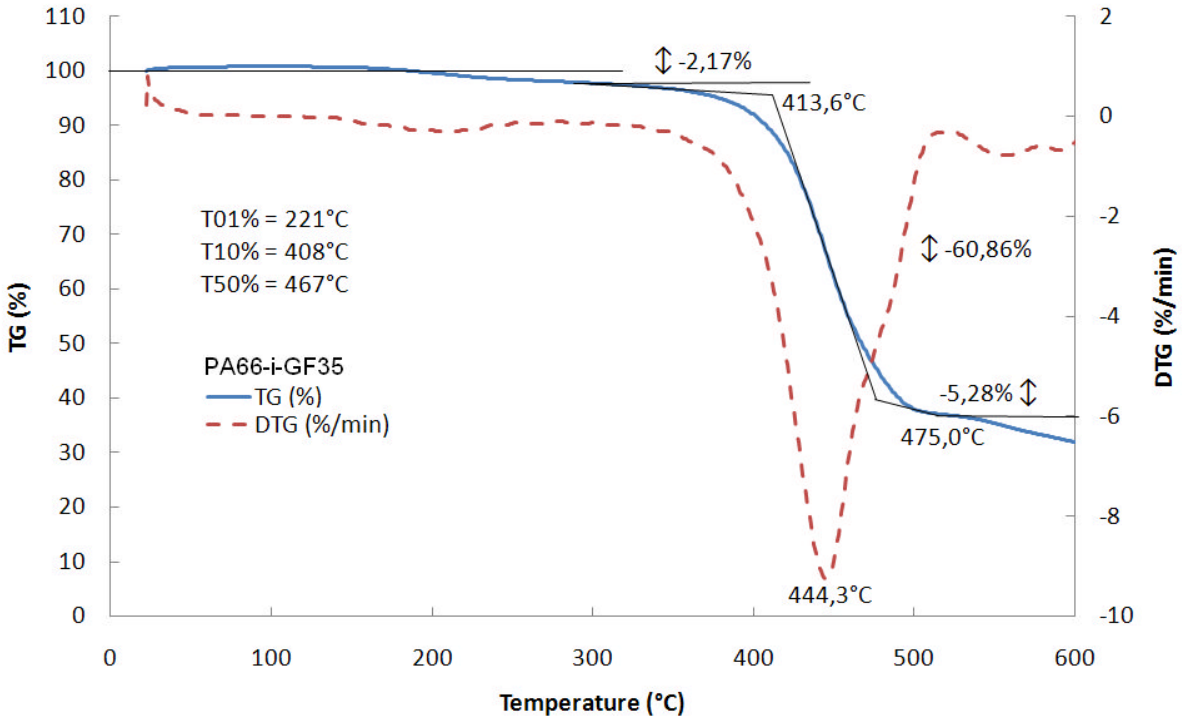

Figure 36 – TG results of PA66-i-GF35

Figure 37 shows the TG of PA6-i-GF35. The mass of the sample at the start is 5.2 mg. The same comment can be used concerning the increase of mass at the beginning as a sign of oxidation. The material at 174°C has lost 1% of its original mass. The temperature of degradation is reached at 459.8°C after having lost, since the beginning, 34.2% in mass and at 464°C it has lost 50% of its mass. Over 600°C, the mass seems to stabilise with a very small slope after 68.2% of mass lost.

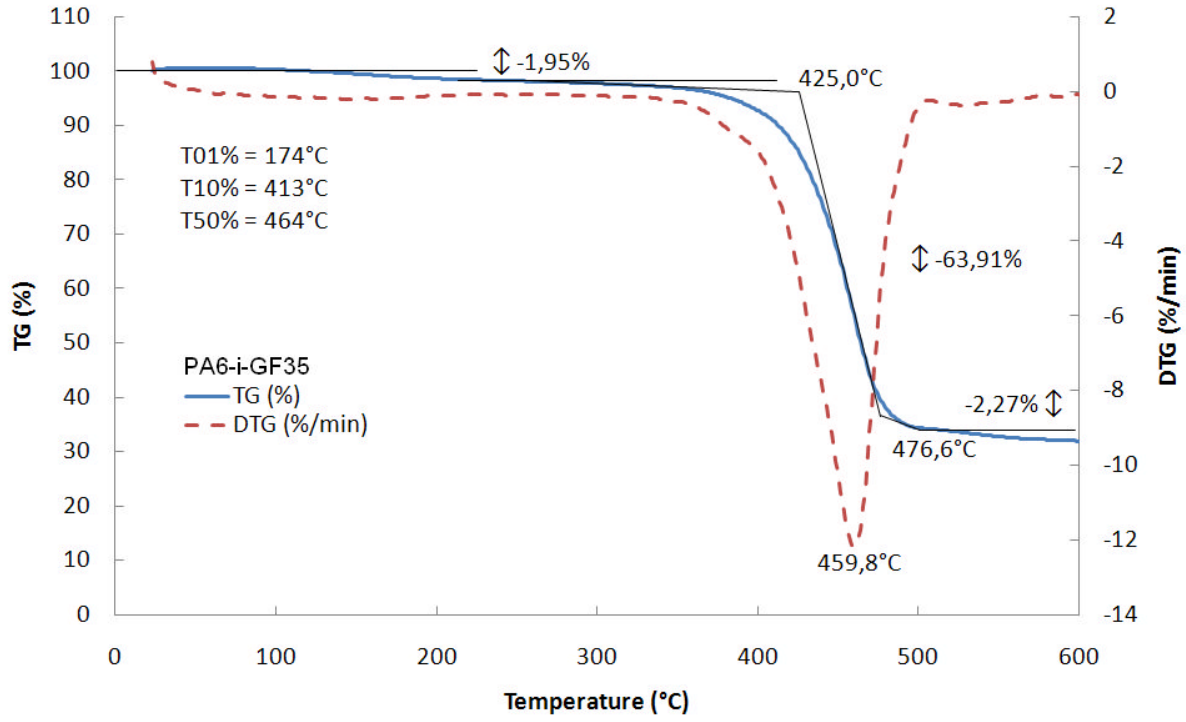

Figure 37 - TG results of PA6-i-GF35

The temperatures of degradation of PA66-GF35 and PA66-i-GF35 are nearly identical within 1,7°C since they are based on the same polyamide (PA66). PA66-i-GF35 and PA6-i-GF35 have lost a very similar amount of weight of 2% before the degradation at respectively around 250°C and 270°C. This correlates with the peaks suspected to be due to the additives in the DSC analysis, which are similar in each material. The evaporation of these additives has for a consequence a loss of weight. The fact that it is not at the same temperature is explained by their divergent arrangements with the different polyamides.

Table 25 gathers temperatures of degradation and masses lost by each material.

Table 25 - Temperature of degradation and mass lost

Materials	Original masses (mg)	Temperature of degradation (°C) and mass lost (% and mg)	Total mass lost (% and mg)
PA66-GF35	5.1	446.0°C – 47% Ξ 2.40 mg	65.3% Ξ 3.33mg
PA66-i-GF35	5.1	444.3°C – 33% Ξ 1.68 mg	68.3% Ξ 3.48mg
PA6-i-GF35	5.2	459.8°C – 34.2% Ξ 1.69 mg	68.2% Ξ 3.55mg

5.4.3. Ageing test results

Figure 38 shows the consequence of heat ageing in oil Shell Helix Plus SAE 5W-40 on the properties of two rubber toughened polyamide grades PA66-i-GF35 and PA6-i-GF35 (ASTM 105). The effect of oil on polyamides may be slightly different depending on the composition of the oil. Some oils have the tendency to strengthen the material and some others to weaken it [138]. However in this particular case, short-term tensile properties are increased up to 1000 hours and then after 1000 hours in a long-term are unchanged or stabilised. The exception is for the tensile strain of PA6-i-GF35 that seems affected and decreases during the first 1000 hours of heat ageing.

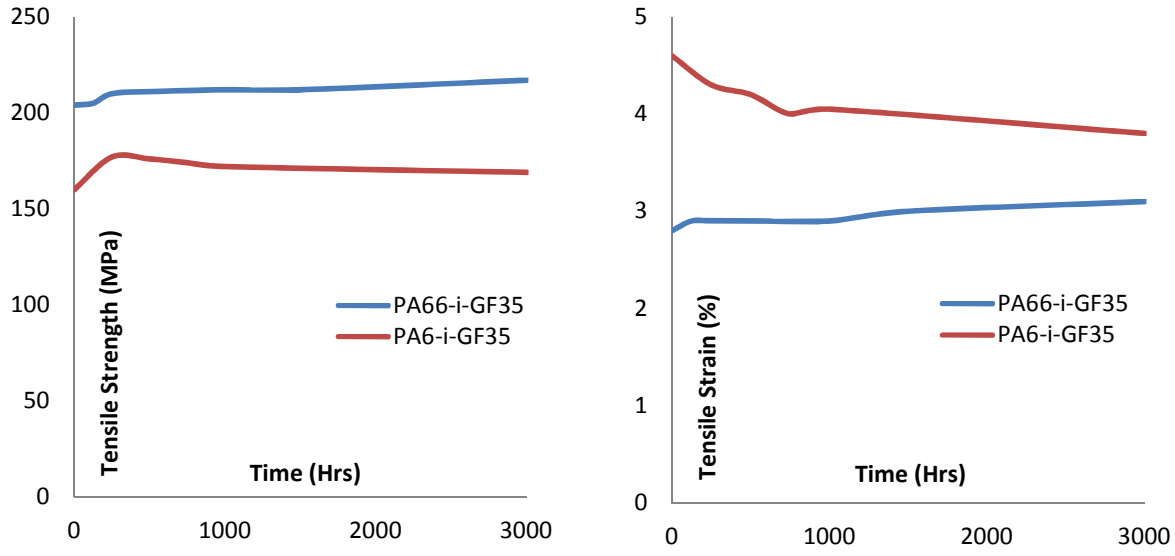

Figure 38 - Heat ageing in oil at 150°C [138]

Figure 39 shows the consequences of heat ageing in the air on the properties of two rubber toughened polyamide grades PA66-i-GF35 and PA6-i-GF35. The oxidation appears to have more dramatic effects on the material mechanical properties in such a way that heat ageing in air is more problematic to those with different types of oil. Tensile strength and strain decline significantly whilst under heat ageing in air [4]. Even after 3000 hours in hot air, which represents more than 4 months, this degradation of properties does not seem to end if tests were continued.

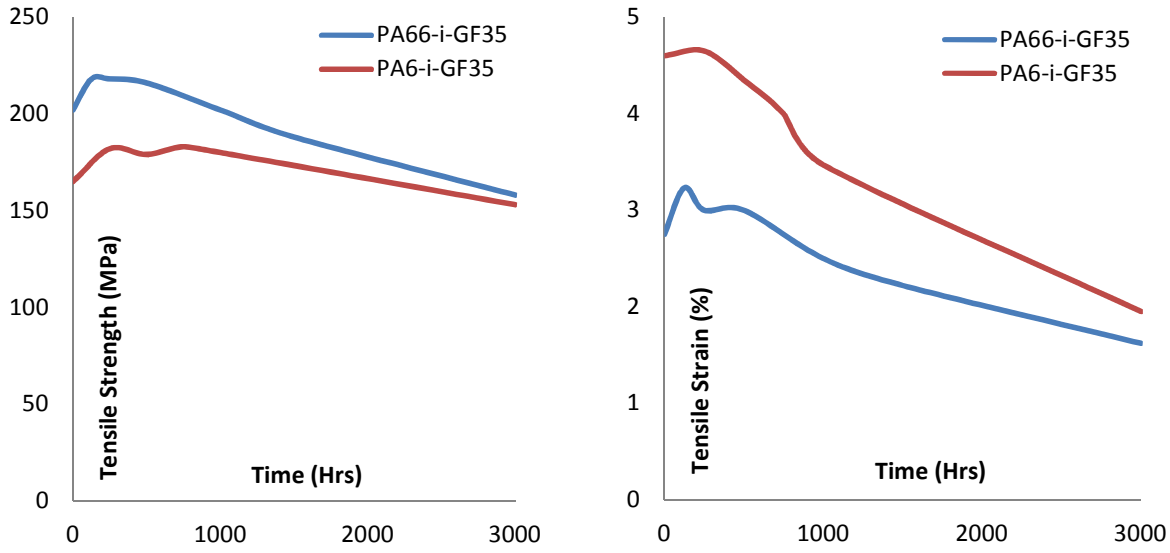

Figure 39 - Heat ageing in air at 150°C [138]

5.4.4. Simulated impact response (-20°C, 23°C, 120°C)

As seen in Figure 31, each material reacts differently with an increase in temperature. Figure 40 illustrates the impact performance on a ribbed structure with the increase of temperature between PA66-GF35 and PA6-i-GF35 and gives the outcomes in each situation.

At -20°C, both materials are rigid and have higher strengths than at 23°C, +23% for PA66-GF35 and +74% for PA6-i-GF35. However, they become essentially brittle, with their strains reduced by -14% for PA66-GF35 and -44 for PA6-i-GF35. At 120°C, both materials have their ductility considerably increased, +173% for PA66-GF35 and +204% for PA6-i-GF35 than at 23°C. Their impact strengths on the other hand are significantly reduced, -51% for PA66-GF35 and -50% for PA6-i-GF35.

At the range of temperatures tested (-20°C, 23°C, 120°C), PA6-i-GF35 has a better impact performance at 7.5 J than PA66-GF35 thanks to its toughness that allows larger deformation. PA66-GF35 has constantly failed when impacted between the ribs especially at low temperature and at the base section of the rib. Its brittleness makes the rib crack whilst exercising pressure on the base wall because the deformation is reduced. On the other hand, PA6-i-GF35 allows more deformation at the range of temperature tested which spreads the impact loading undertaken by the structure.

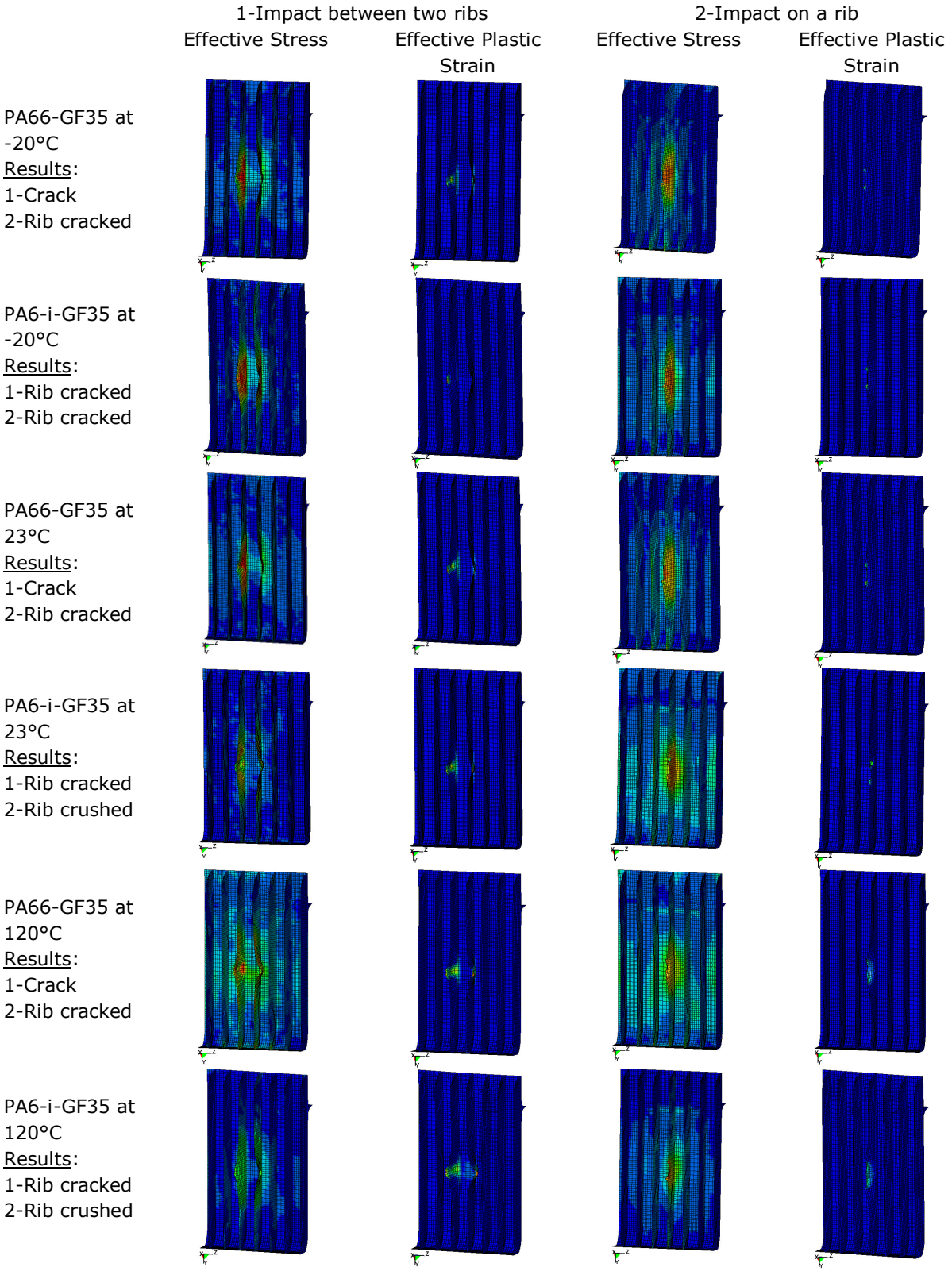

Figure 40 – Impact performance on a ribbed structure at -20, 23 and 120°C at 7.5 J

Figure 41 shows the variation of the peak load with the temperature for each material impacted at 7.5 J. An increase of temperature reduces the peak load response significantly. The rubber modified polyamide grade, PA6-i-GF35, exhibits a lower load level by -30% at 7,5 J compared to the non-rubber modified material, PA66-GF35, throughout the range of -20°C to 120°C. The rubber content in the modified polyamide makes it tougher. The brittle to ductile transition temperature is decreased thus improving the impact behaviour at low temperatures. My findings agree with Borggreve et al. [151].

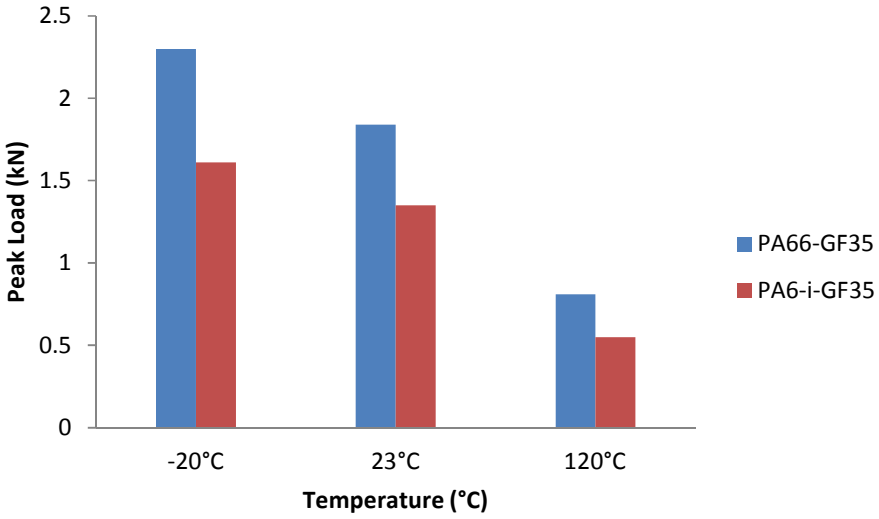

Figure 41 - Variation of the peak load with the temperature at 7.5 J

5.5. Conclusions

DSC and TG analyses conducted on PA66-GF35, PA66-i-GF35 and PA6-i-GF35 permitted to distinguish polyamide grades, the fibre glass and more importantly to reveal the presence of the impact modifier and its effect on the material in terms of heat exchange and temperature degradation. The polymers have their characteristic melting point temperature, which is around 260°C for PA66 and 220°C for PA6. The impact modifier interferes by lowering the consumption of heat needed for the polymer to melt. In the case of PA66-GF35 and PA66-i-GF35, this difference is 8 J/g. When subjected to heat degradation, the materials having the impact modifier lose 2% of their masses before reaching the temperature of degradation of their polymer.

Ageing effects in hot oil and in hot air revealed some disparity between PA66-i-GF35 and PA6-i-GF35. PA66-i-GF35 has a better tensile strength but a lower tensile strain than PA6-i-GF35. The oil (Shell Helix Plus SAE 5W-40) tends to slightly increase strength and strain except the strain of PA6-i-GF35, which is regularly affected over time. The hot air, however, is the parameter that affects both materials strengths and strains very dramatically and constantly over the time.

The simulated influence of the temperature on PA66-GF35 and PA6-i-GF35 on a ribbed structure illustrates their impact resistance and their temperature dependency. The increase of temperature softens each material which absorbs more impact energy in deformation. The rubber modified material PA6-i-GF35 absorbs more energy in deflection and deformation compared to PA66-GF35. The brittleness of PA66-GF35 at -20°C contributes in broken wall and ribs whereas the toughness of PA6-i-GF35 allows progressive damage on the structure with ribs that absorb the impact energy by crushing. PA6-i-GF35 also allows larger distribution of the impact loading which results in a reduced peak load compared to PA66-GF35 in the range of temperature studied (-20 to 120°C).

Chapter 6. Influence of structural configuration on impact performance of short glass fibre reinforced polyamide 66s

6.1. Introduction

When designing a part with dimensional stability it is important to have a robust and optimised the design with good strength to loadings likely to occur and even taking into consideration the characteristics of the impacting object. Particular geometrical patterns must be developed in response to certain stresses.

Corrugated design is frequently used for applications to resist external pressure loads undergone by buried plastic PVC (polyvinyl chloride), PE (polyethylene) and PP (polypropylene) cables or drainage pipes [172]. Corrugations in tubular structures were found to increase the maximum buckling resistance, whilst reducing wall thickness by nearly 60% in some cases [173]. Tubular structures are found to provide efficient stiffness against bending loads in the directions of the corrugations and also deliver good flexibility perpendicularly to the directions of the corrugations. However, it is also found that different plastics for pipes require different corrugation designs in terms of curvature, pitch and depth of the corrugations and that attention must be paid to balance good resistance to bending and impact strength [172; 174]. Finite element analyses performed on the structure capacity on corrugated metal box culverts found that small

variation in the culvert geometry has noticeable but not severe effect on deflections and moments [175; 176] but experimental testing are required to assess the accuracy of the predictions. Corrugated design is also found in corrugated metal sheets as load bearing structure of roofs of industrial buildings or corrugated box culverts providing good stiffness over long span and durability compared to asphalt shingles. However, metal roof sheeting is prone to thermal elongation / contraction movement and potentially susceptible to corrosion or rusting through bolts [177]. Multi-layered corrugated paperboard, used for protection of products against mechanical shocks and vibration during transportation and handling, was investigated under shock loading or equivalent drop [178; 179] and it was found that inserting layers of sacrificial crumple elements of corrugated paperboard dramatically increases the overall level of protection to products in terms of expected edgewise crush strength [180]. Finite element analysis was also developed to determine the strength under compression in corrugated fibreboard structure [181] but it is based on linear isotropic elasticity properties. Furthermore, as this structure is voluntarily designed to be sacrificial, the number of shocks or drops is limited and therefore their protective performance.

The ribbing pattern is also another protective feature well developed along corrugations in underground infrastructure pipe work, but also in a lot of plastic vehicle parts to stiffen a flat area [182]. The drive towards

miniaturisation and lightness has led to a constant decrease in the wall thickness of enclosure applications necessitating the use of ribs to enhance the impact resistance. Furthermore, several simulations studies looked into prediction of the material behaviour and the effect of wall thickness and rib optimised dimensions [63; 183; 184]. Numerical explorations indicated that the ratio of wall thickness to rib height is the predominant factor to determine impact failure energy, and then followed by rib thickness and centre to centre ribs spacing [184; 185]. It was shown that load versus displacement behaviour of impacted plastic disk/plate can be accurately described using bi-linear representation of the stress-strain curve and flow theory of plasticity with strain-rate effects implemented [186]. Automobile bumpers can also include ribs. The impact behaviour of an aluminium bumper was investigated in low velocity impacts finite element analysis [182]. It was found that the addition of ribs causes an increase of rigidity, impact force and reduction of bumper deflection compared to an un-ribbed bumper but with a gain in mass as well. Localised impacts on transmission oil pan covered with a ribbing pattern were investigated to simulate stones impacts [187]. It was found that the ribs elastically absorb the impact energy and prevented direct contact between stones and pan base wall. However, the ribs were defined to be sacrificial and were systematically destroyed leaving an unprotected base wall that is susceptible to follow up with impacts occurring in the same location.

In this chapter, the influence of an un-ribbed flat structure is compared against corrugated and ribbed structures on low velocity localised impact performance. The sidewalls of the current thermoplastic oil pan are flat and unprotected (Figure 42). In the past, these areas were considered to be at low risk and were not a design priority prior to an extensive experimental program being undertaken [34]. Besides, the existing ribbing on the bottom section of the part was designed as sacrificial which is not desirable. The ribbing should protect the base wall without being snapped at the first impact.

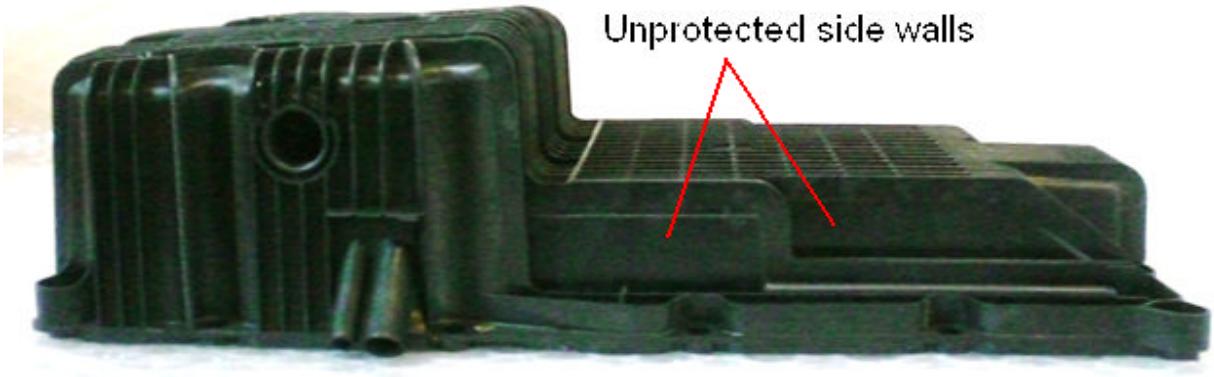

Figure 42 - Unprotected sidewalls on thermoplastic oil pan

6.2. Finite element modelling

6.2.1. Materials and test models

Material employed for the simulations is a PA66-GF35, a 35 wt% of discontinuous glass fibre reinforced polyamide 66 with properties taken at temperature of 23° C. PA66-GF35 was the first material used for the plastic oil pan. For more information on simulation settings, refer to section 3.2.2.

The original 2D CAD model of the oil pan was used as a starting point to build a corrugated and ribbed pattern on the sidewall. In Figure 43, sections of 100 x 100 mm of each pattern are used for impact simulations. These sections were constrained on their edges. In parallel, the effect of the elongation is studied using models with double height (100 x 200 mm).

The effect of the ribbing on a wall is also studied more specifically against an un-ribbed wall. Firstly, the consequence of a 7.5 J impact using 80468 shells ribbed oil pan against 49006 shells un-ribbed oil pan is assessed and then using 100 mm diameter models of 9690 shells flat disk and 12158 shells single ribbed disk impacted at 5 J (Figure 44). The base wall is 3 mm thick (same for all models) and the rib is 2 mm thick and 10 mm tall.

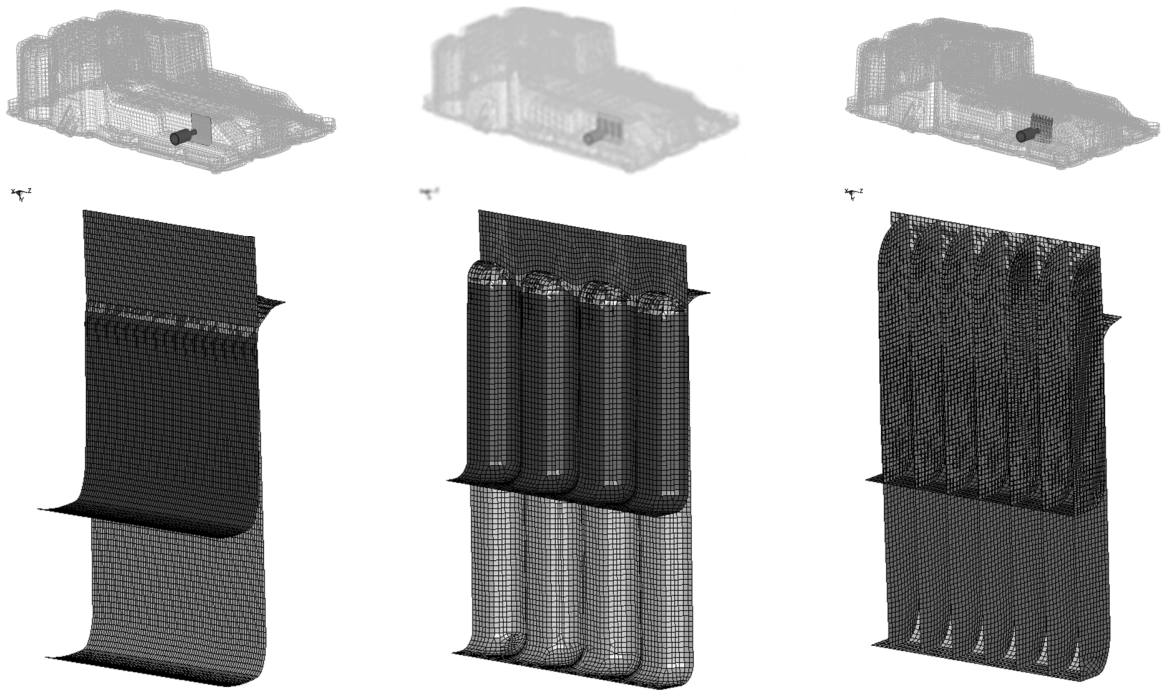

2D Unprotected flat models
5391 & 7480 shell elements

2D Corrugated models
4974 & 7675 shell elements

2D Ribbed models
7253 & 11286 shell elements

Figure 43 – Outer view of three patterns on sidewall with superimposed elongated models

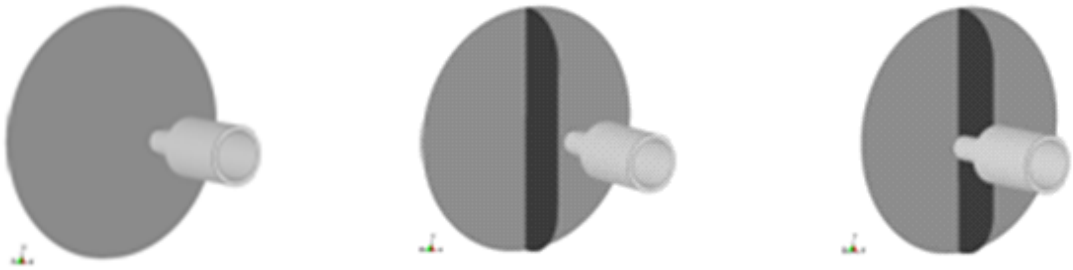

49006 shells
Centre impact

80468 shells
On rib impact

80468 shells
Off-centre impact

Figure 44 - Flat disk and single ribbed disks

6.2.2. Impact conditions

Impact simulations were performed with LS-DYNA. Each section is impacted in its centre with a 10 mm, 22 g projectile 90 degrees to surface. Impacts are located on the centre of flat wall, on and between ribs, and on and between grooves of the corrugations, and between the ribs and the grooves under the following conditions:

1. The comparison between each model is assessed at three impact velocities so as to achieve impact energies of 3 J, 7.5 J and 12.2 J.
2. The effect of the elongation on each model is also studied and compares their impact performances at 7.5 J (26 m/s) impact.
3. Finally, the effect of the ribbing on a wall is performed on a ribbed and un-ribbed oil pan at 7.5 J and at 5 J on disk and single ribbed disk at different impact locations, in the centre, on the rib and off-centre of the rib reducing the deflection. The disk is used so as to avoid or reduce edges effect. The ribbing is expected to act like a shield against the impacting projectile and protect the base wall.

6.3. Results and discussion

6.3.1. Effect of the geometry

Table 26 provides the energies of the system. The kinetic energy history of the projectile allows checking if the impact energy was completely transferred to the target by the return to zero. At this point, the impacted section is at its maximum deflection. Afterwards, the excess of energy accumulated during the deflection is given back to the projectile. The difference between the initial and final kinetic energy of the projectile recorded provides the energy dissipated during the impact in the structure. The more energy dissipated through a large area, the better if the base wall resisted. The manner of how this energy is dissipated is different in each model and impact position. The absorbed energy can lead to failures through cracks or perforations. Table 26 also provides the maximum displacement measured at the base wall. The maximum displacement is reached when the velocity of the projectile is null. Less displacement means that the structure is rigid. Each structure deflects to an extent and some bear the load by deflecting more to resist the impact but some are restricted. For instance, the unprotected flat model deflects 2 to 3 times more than the wall of the ribbed model. The ribbed model benefits of the stiffening ribbing pattern which also reduced the damage on the wall. Therefore the ribbed model is stiffer than the flat wall. The corrugated model sits between the unprotected

flat model and the ribbed model in terms of stiffness and provides more distance or surface to deflect than the two other structures.

Finally, Table 26 provides the resultant forces recorded on the wall of each structure. The higher is the force undergone by the base wall, the more damage occurs. The force created by the base wall to resist the impact is proportional to the effective incoming force endured. The flat model suffers more than the other models. The ribbed model appears to have the best protective feature. The more mass the model has got, the better the model resists. The thickness parameter has not been modified in order to readjust the mass, as it is a relatively fixed parameter for base wall mouldings.

Table 26 - Energies, maximum displacements and resultant forces on each model

Model Impact position	Impact energy (J)	Energy given back (J)	Energy dissipated (J)	Maximum displacement (mm)	Resultant force (kN)
Unprotected flat Centre	12.2 7.5 3	2.6 1.9 1.3	9.6 5.6 1.7	0.27 0.19 0.12	8.5 7.7 5.5
Corrugations Centre convex	12.2 7.5 3	3.8 3.2 2.2	8.4 4.3 0.8	0.44 0.32 0.19	5.6 5.1 3.9
Corrugations Centre concave	12.2 7.5 3	4.5 4.1 2.4	7.7 3.4 0.6	0.36 0.28 0.19	6 5.5 4.3
Ribbing On rib	12.2 7.5 3	0.9 0.5 0.4	11.3 7 2.6	(0.007)* 0.019 0.010	(2)* 3.4 2.4
Ribbing Between ribs	12.2 7.5 3	1.5 1.3 1.0	10.7 6.2 2	0.018 0.014 0.004	4.1 1.9 0.9

()* Low values explained by crushed or shattered rib which has dissipated the energy away of the base wall and therefore reduced displacement and force undergone by the wall.

Table 27 provides the contact and internal energies histories. The contact energy also called the sliding interface energy is the measure of the work done to overcome frictions between the contacting surfaces. The contact energies are almost conversely proportional to the kinetic energies. At the end of contact, the contact energies correspond to the dissipated energies in each structure. For flat and corrugated models having their base wall directly impacted, nearly all of this contact energy is transferred into internal energy. The ribbed model received a small quantity of this contact energy in the base wall. The ribbing consumes a great amount of the incidental energy. Less internal energy in a structure is better [30]. The structure works less therefore the damage is reduced.

Table 27 - Contact energies and internal energies histories on each model

Model Impact position	Energy received (J)	Contact energy (J) at maximum penetration	Internal energy (J) at maximum penetration	Contact energy (J) at end of contact	Internal energy (J) at end of contact
Unprotected flat Centre	12.2 7.5 3	11 6.9 2.5	10.5 6.5 2.4	9.5 5.5 1.6	9 5 1.4
Corrugations Centre convex	12.2 7.5 3	11.4 6.8 2.7	11 6.6 2.6	8.2 4.2 0.8	7.7 3.9 0.8
Corrugations Centre concave	12.2 7.5 3	10 5.5 2	7.6 5.4 1.9	7.2 3.1 0.4	6.9 2.8 0.3
Ribbing On rib	12.2 7.5 3	10.7 7.3 2.6	(0.16)* 0.18 0.13	10 6.8 2.2	0.08 0.05 0.05
Ribbing Between ribs	12.2 7.5 3	9.2 6.3 2.8	0.29 0.20 0.14	8.5 5.4 1.9	0.10 0.07 0.06

()* Low value explained by crushed or shattered rib which has dissipated the energy away of the base wall and therefore reduced internal energy measured on the wall.

Figure 45 illustrates the impact event of the unprotected flat model. The flat model received directly all of the incident energy on its base wall. The wall deflects creating circular waves of deformation towards the edge. At low impact of 3 J, when the initial wave encounters an edge, it goes backwards. When this wave is confronted to the first opposite wave, the wall undergoes a failure at the meeting point. At high impact of 12 J, the intensity is already too high when the wave meets the edge and the failure is initiated from the edge or at the impact point.

Figure 46 pictures the impact event of the corrugated model. As in the unprotected flat model, the incident energy is directly received into the grooves. In the corrugated structures, the deformation wave goes sideways when concavely impacted and upward and downward when convexly impacted. The grooves create pre-constrained areas of tension and compression. As a result, a succession of strong and weak zones is formed and the direction of the wave follows the easy route to propagate. Compared to the unprotected flat model, the corrugation model reduces the damage by an average of 45%.

Figure 47 shows the impact event of the ribbed model. When the impact is between two ribs, the deformation shock wave goes sideways and once it has reached a rib, the rib redistributes the wave all along its length.

When the impact is on a rib, the shock wave goes in line with the rib upward and downward on its length. The ribbing protects the base wall to a large extent but this protective feature design sometimes cost the ribbing to be altered after the first impact. Compared to the unprotected flat model, the ribbed model improves the impact resistance between 56% whilst impacted between ribs to 85% whilst impacted on a rib.

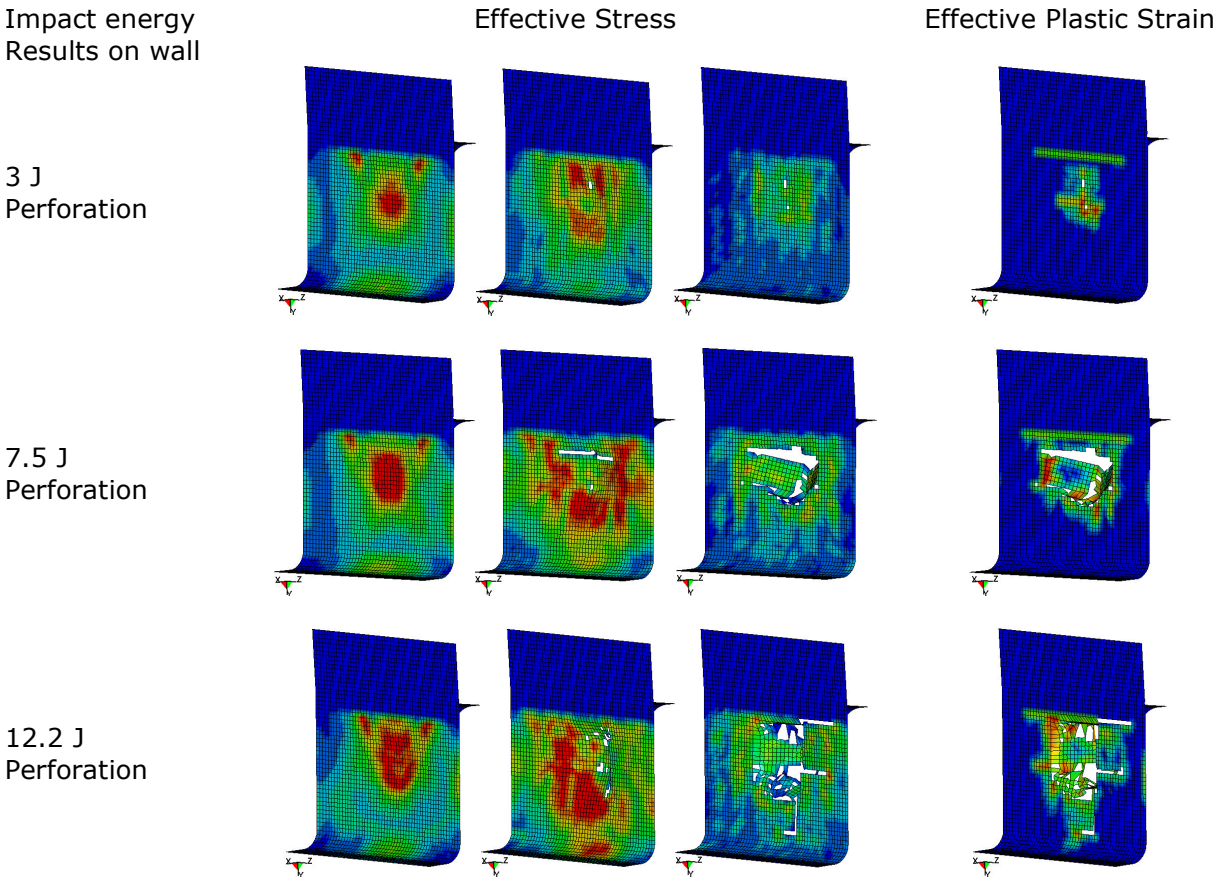

Figure 45 - Impact performance of the unprotected flat model

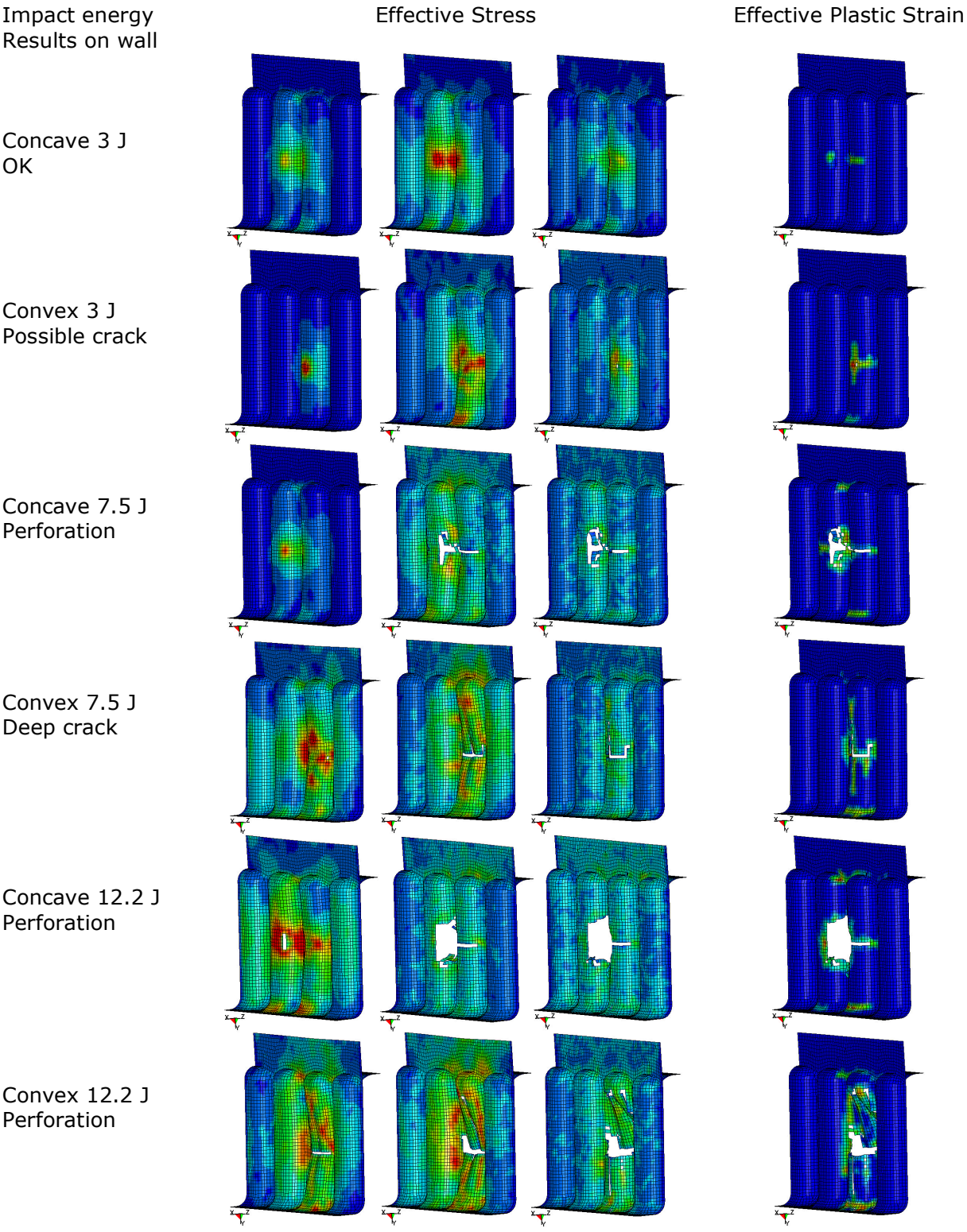

Figure 46 - Impact performance of the corrugated model

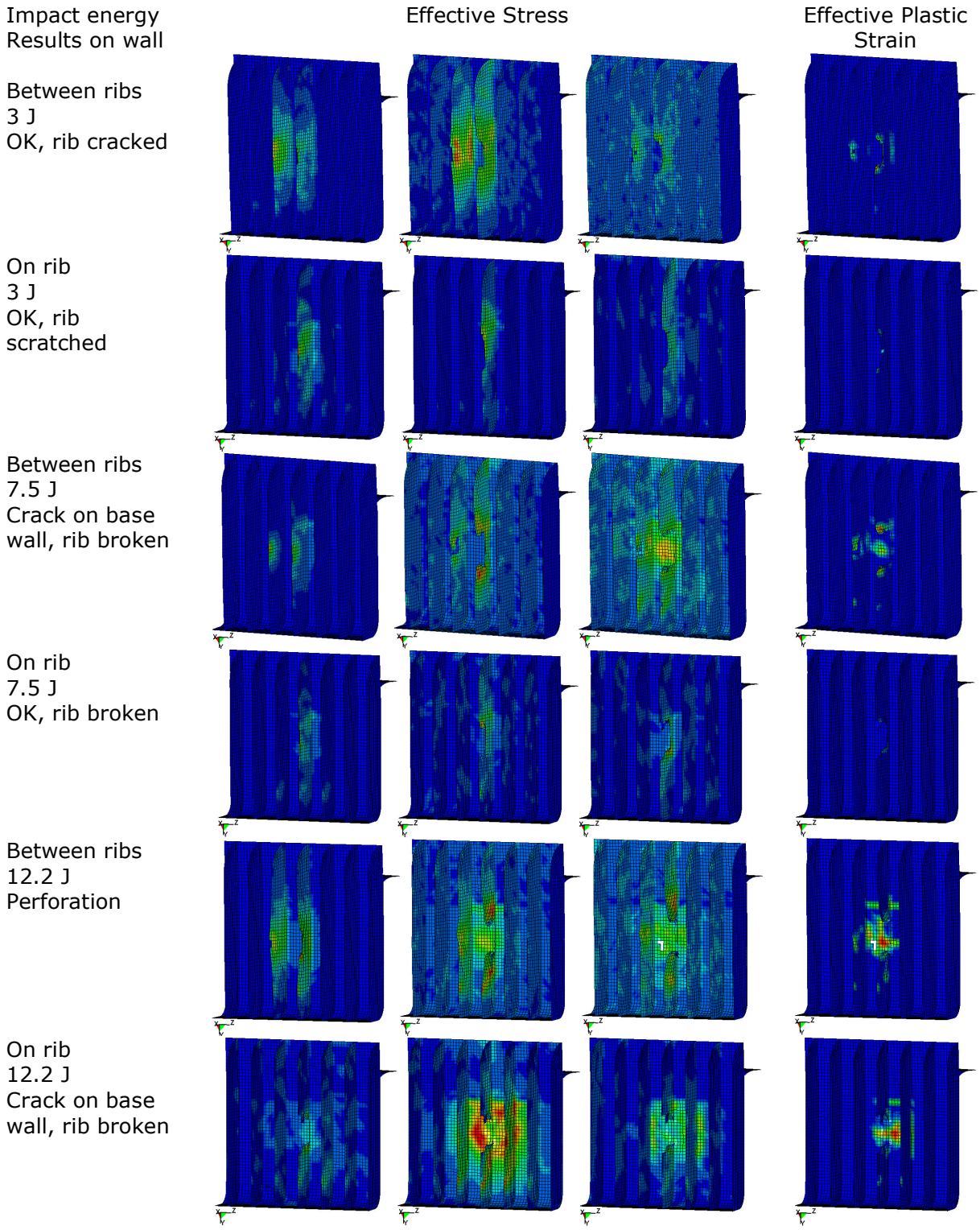

Figure 47 - Impact performance of the ribbed model

6.3.2. Effect of the elongation

Figure 48 illustrates the effect of the elongation after a 7.5 J impact on the unprotected flat model and its double height elongated model. In both models, the base wall is directly touched and both have failed but at different level of damage. The regular size flat model was perforated from the outer side to the inner side and the projectile went almost through it. The elongated model resisted better but was deeply cracked, meaning that the failure reached the neutral axis of the part. The elongated model allows more deflection and therefore has permitted to reduce the extent of the damage by around 65% compared to the non-elongated flat model.

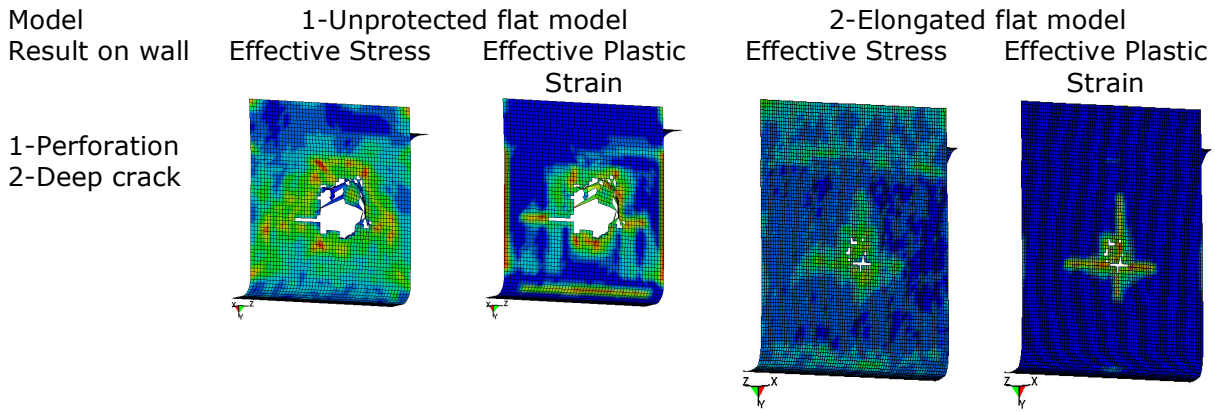

Figure 48 - Unprotected flat pattern and its elongated model at 7.5 J

Figure 49 shows the effect of the elongation after a 7.5 J impact on and between the grooves of the corrugation model and its double height elongated model. In both case, a concave impact is more damaging than a convex one. In a concave impact, tension stresses are found on the inner face of the impact area but also on the outer face on the edge of the nearest convex corrugations and that considerably affect the impact resistance. The increase of deflection did not really improve the impact resistance. The scale of the damage is slightly reduced by 8% on a concave impact and 2 % on a convex impact.

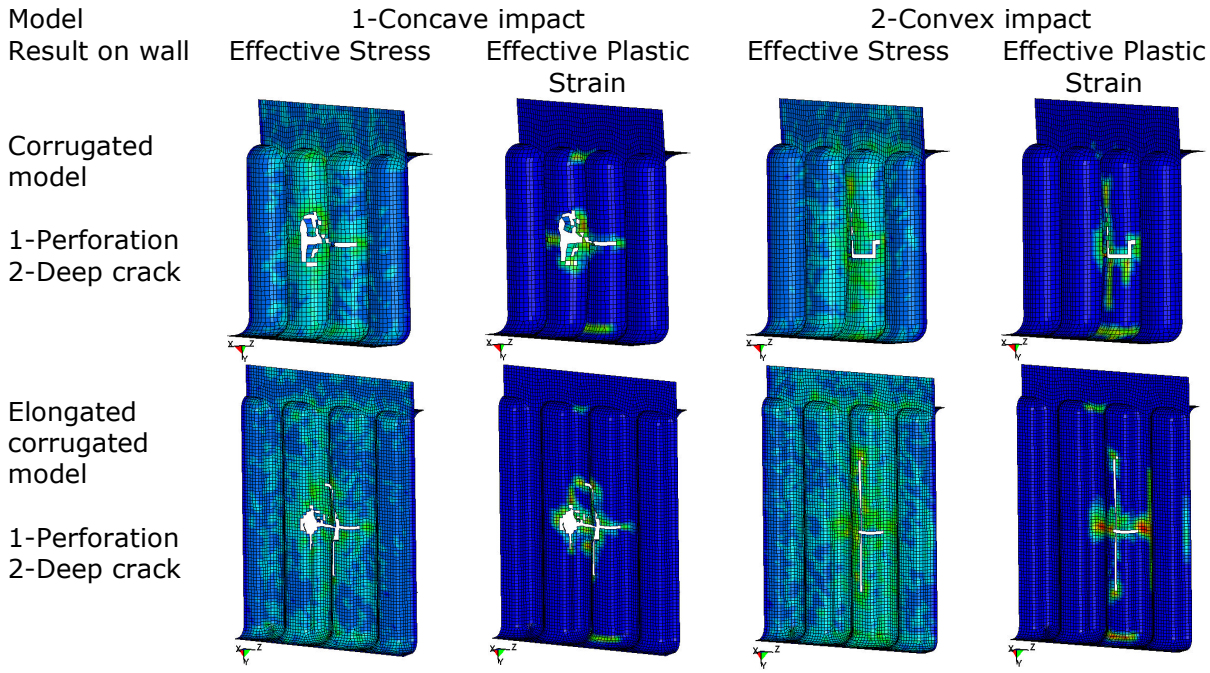

Figure 49 - Corrugated pattern and its elongated model at 7.5 J

Figure 50 pictures the effect of the elongation after a 7.5 J impact on and between the ribs of the ribbed model and its double height elongated model. Longer ribs mean long area to dissipate the impact energy. The elongation did improve the way the structure resists to the impact. The impact resistance is improved between 30 to 35 % and especially when the impact occurs between two ribs. Nevertheless, the ribbing still cracks and breaks in the same manner.

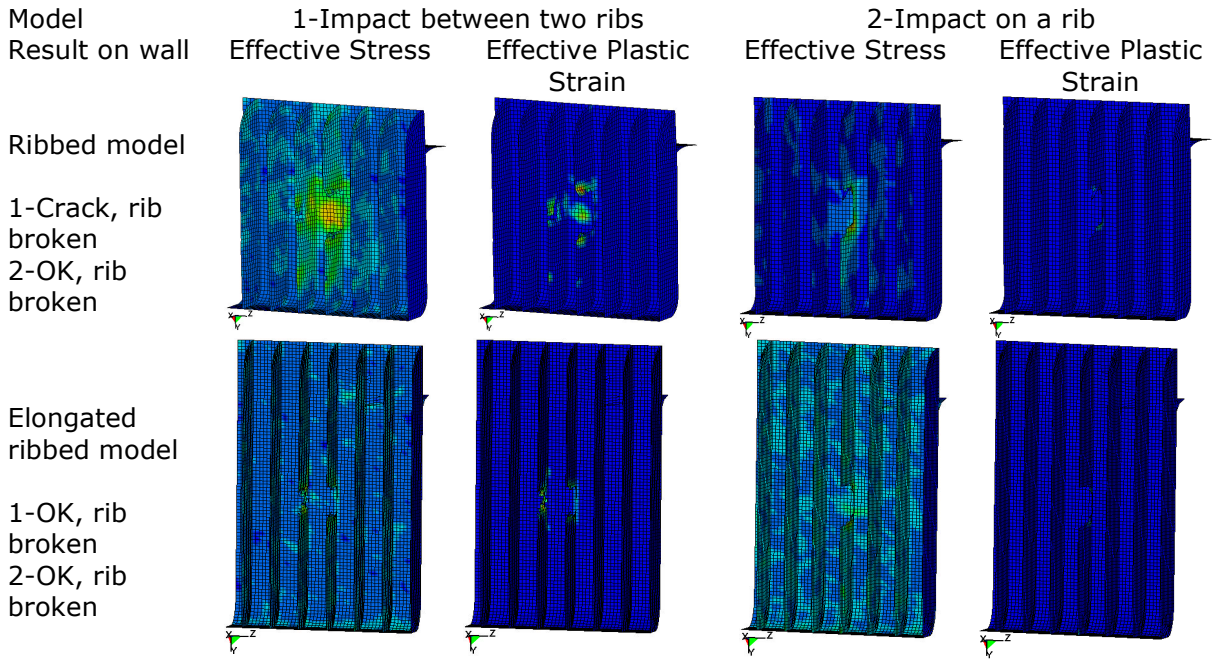

Figure 50 - Ribbed pattern and its elongated model at 7.5 J

6.3.3. Effect of the ribbing

The structural geometry determines the target impact response. Figure 51 shows the visual damage of a single impact conducted at 7.5 J and shows the contours of the effective plastic strain undergone by ribbed and un-ribbed oil pan. The ribbed oil pan has a rib damaged, half crushed, but the base wall remained entire despite a small and negligible point of plastic deformation at the bottom of the rib. The maximum strain collected at the wall is 0.2%. The wall of the un-ribbed oil pan, however, has directly supported the impact resulting to a 6 mm perforation which if filled with oil will have led to an oil leakage with bad consequences to the engine. The strain has reached and overcome the 3.8% strain failure criterion. This clearly shows the great contribution of the ribbing in the protection of the oil pan.

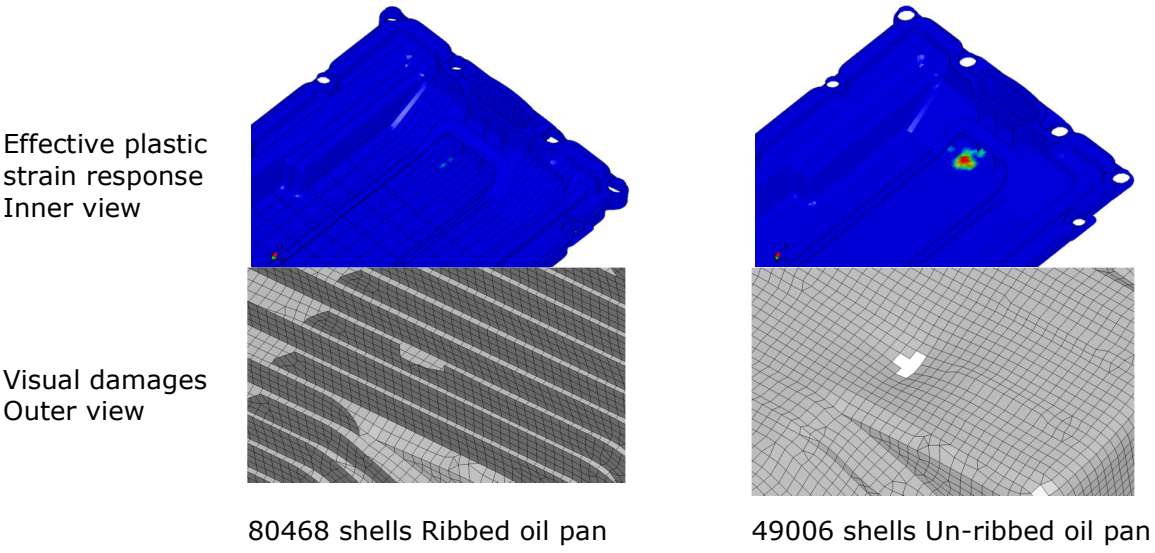

Figure 51 - Single 7.5 J impact on ribbed and un-ribbed oil pan

The effect of the ribbing is also highlighted on a 5 J impact on 100 mm diameter disks, flat disk and single ribbed disk impacted in the centre, on the rib and halfway off-centre the rib (see Figure 44). The measured point is situated on the base wall in line with the axis of the impact. Figure 52 shows the displacement histories and Figure 53 displays the energy histories of each model.

In the flat disk model, the disk has no protective feature. At 5 J centre impact (21.3 m/s), the disk undergoes the highest force (4 kN) and also the largest displacement (4 mm) and eventually fails, perforated.

In the single ribbed disk model with impact on the rib, the disk withstands the lowest force amongst all (1 kN) and the smallest displacement (0.7 mm). As the measure point is on the base wall and that the rib supports the impact, the maximum energy received by the disk is only 1.9 J from the initial 5 J impact. The disk remained entire. The rib has consumed over 60% of the incidental energy and an insignificant energy was given back to the projectile (0.1 J).

In the single ribbed disk model with impact halfway off-centre, the elongation allowed is half reduced because of the rib in the middle. Therefore the wall is stiffer than the flat disk model. The model withstands a force slightly lower (3.5 kN) but this rigidity permitted to reduce

considerably the base wall displacement (1.1 mm) compared to the flat disk model. The energies absorbed are somewhat equals (2.5 J). Despite an important effective plastic strain, the disk is unbroken.

The rib reduces significantly the maximum penetration and the forces undergone by the disk, and mostly when the rib is directly impacted. As a protective feature, it stiffens the structure and reduces the elongation of the wall.

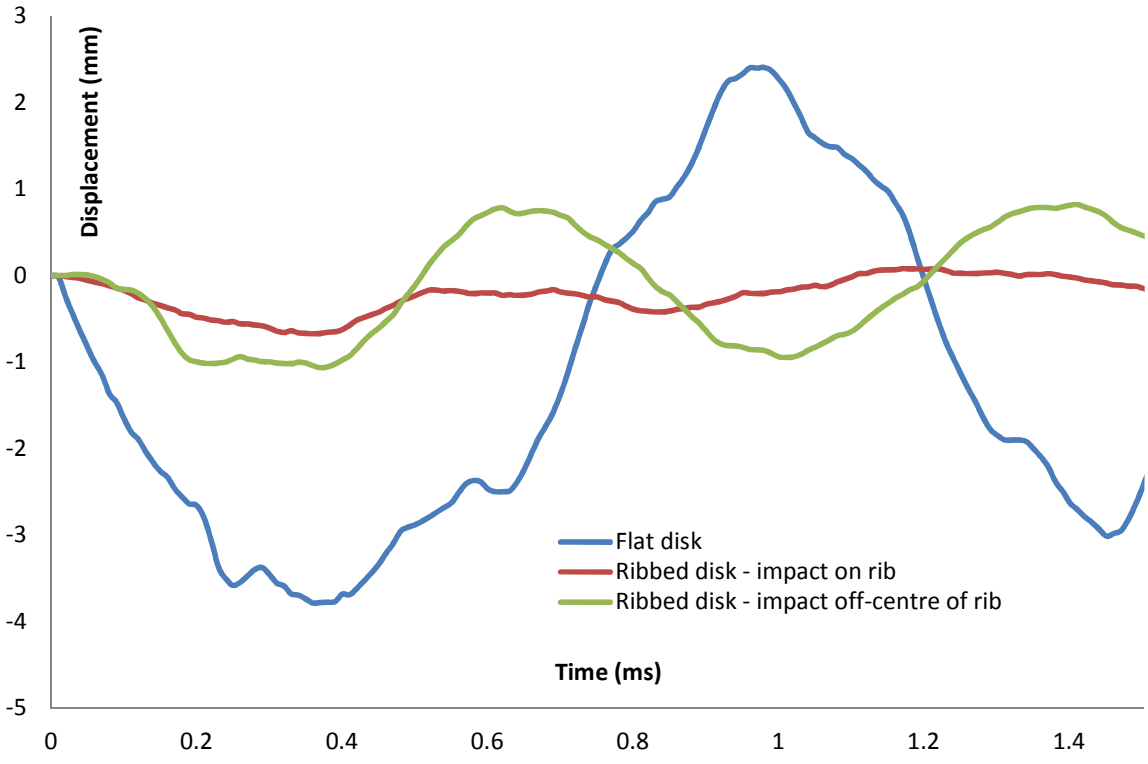

Figure 52 - Displacement histories of flat and single ribbed disks at 5 J

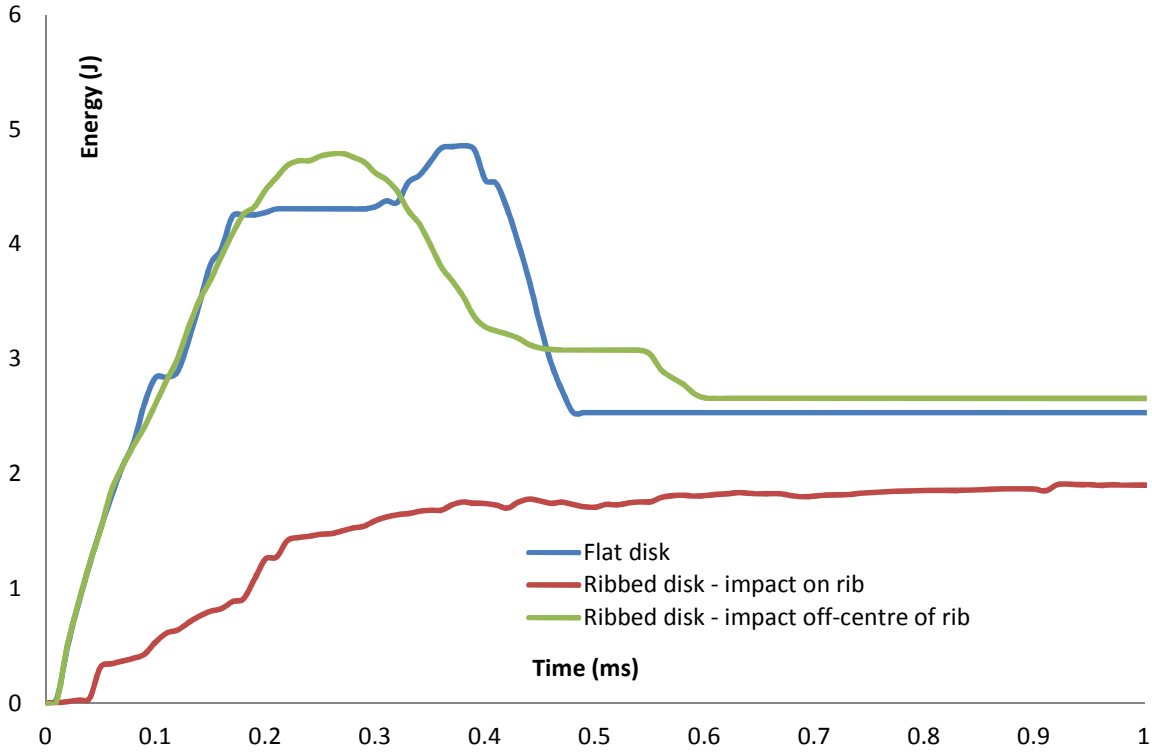

Figure 53 - Energy histories of flat and single ribbed disks at 5 J

6.4. Conclusions

In order to improve sidewall impact performance on the oil pan, two protective designs were investigated alongside the existing unprotected flat wall. This study highlighted the important role of the geometry in such situation. The unprotected flat pattern has no protections against impacts and therefore the structure is directly impacted. The corrugated model does improve the impact resistance compared to the flat wall but it suffers of its

succession of constrained areas creating zones where stresses are likely to be concentrated. This design is more dedicated to resist pressure homogeneously than a localised impact. Amongst the geometries tested, the ribbed model stands as the best design thanks to its ribbing pattern. The rib absorbs a significant amount of the impact energy (over 60% on a 5 J impact) as a result the base wall is, to an extent, not compromised. The rib erodes and keeps the wall structure safer than the two other designs by withstanding the impact and spreading the stress along themselves. The localised impact energy becomes spread in a much longer area reducing the risk of having the wall damage. However, this protective feature can be altered after the first shot and this can cause problems if there is another impact in the same position.

The elongation of the base wall by a factor 2 in height proved the ability of the structure to improve the impact resistance by deflecting more. However, each design was improved at different level. The flat wall was improved by 65% and the ribbed wall by 30 to 35%. However, the enhancement on the corrugated wall was very little, 2 to 8%.

On the oil pan, the ribbing stiffens the structure and therefore gives a dimensional stability. The ribbing pattern helps to keep the wall structure entire whilst consuming the major part of the impact energy. As a protective feature, it stiffens the structure and reduces the deflection of the wall by up to 95% compared to the unprotected flat wall.

Chapter 7. Localised low velocity impact performance on reinforced polyamides oil pans

7.1. Introduction

The under carriage of any road going production vehicle contains many vulnerable components. Driving on gravel surfaces, tough roads, near construction sites or during road maintenance can cause stones to be ejected from the wheels which then are projected into the air and could possibly damage the under carriage area of a car. The main concern of this research is the impact performance and damage caused by those stones to a recently converted engine oil pan for light utility vehicles into PA66 reinforced with 35% of short glass fibre. Figure 54 shows an early version of the thermoplastic oil pan that has been damaged by foreign flying debris, identified as a stone by the fragments left on the impacted surface (Figure 54-a). The engine oil was seeping out through the crack from the inner side (Figure 54-b) to the outer side of the pan (Figure 54-a).

Damage tolerant design of vehicle components requires a methodology to predict the likelihood of critical impacts occurring over the operational lifetime of the vehicle. Such information could be provided by examination of the damage caused in previous incidents, so that the locations of severe impact damage can be mapped out. In practice, the limited availability of such detailed records makes this approach very difficult to utilise. An

alternative approach relies on understanding the complex lofting processes of objects by wheels, which may be considered as an impact event given the high speed at which a tyre may contact the object [188].

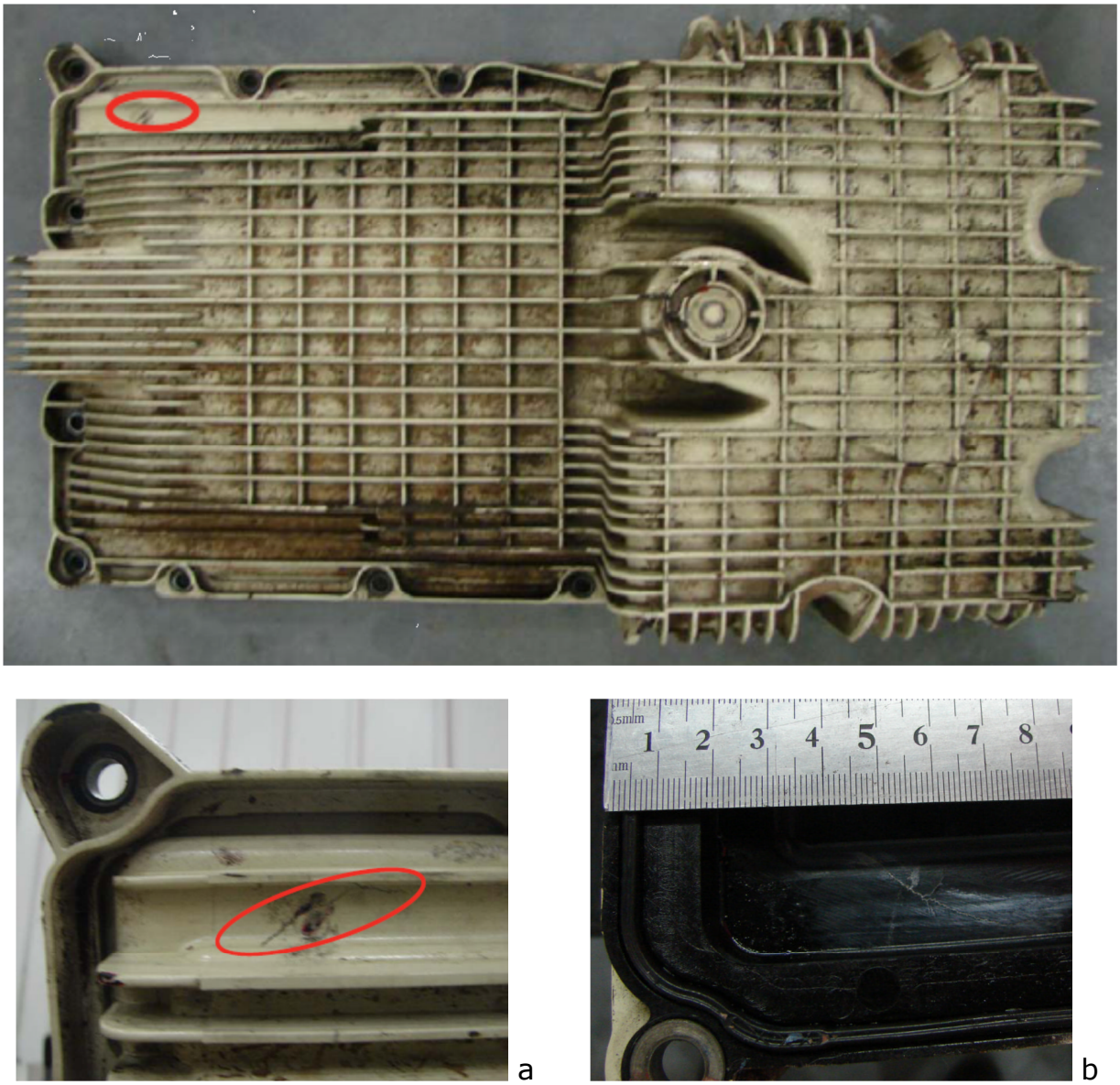

Figure 54 - Thermoplastic oil pan crack failure, a) outer side, b) inner side [34]

Few investigations were conducted to assess the threat of impact damage caused to vehicles or aircrafts by tyre-lofted runway debris, yet there is limited understanding in the stone lofting process and in the influence of stone characteristics [35; 188-192]. It comes out that a compilation of stones collected from roads or airfields led to stones of various shape with different overlaps, orientations and densities. However, the conditions most conducive to stone lifting concerns stones with small diameters lofted following different mechanisms. The tyres can hammer or pinch the stone, and in the process the stone can be deviated by some asperity on the road. The tyre tread grooves could also throw stones upwards. The tread of a tyre is typically a few millimetres in width. Table 28 shows the variables and attributes of the stone impact phenomenon [193].

Table 28 - Stone impact phenomenon

Variables	Attributes
Projectile	Shape, mass, density and material constants (modulus, Poisson's ratio)
Impact conditions	Velocity and angle of incidence
Ambient conditions	Temperature and humidity
Component system	Type (material properties), thickness (injection moulding), stiffness (ribbing), strain rate properties, moisture uptake

The characteristics of stones likely to cause damage into the engine oil pan presented in the Figure 54 were quantified allowing the measurement of road stones typical mass and size [194]. The granite stones shown in Figure 55-a weigh less than 17 g and all fit into the damaged area between two consecutive ribs except the two big stones on the right side; the rounded

stone weighs 21 g and the larger one weighs 78 g. There are variable gaps between the ribs in the area of impact. An 87 g random stone with a pointy profile is able to fit into the gap where damage is evident, Figure 55-b. A possible solution would be to reduce the rib spacing so as to exclude more stones, Figure 55-c. However, the mistake would be to overload the oil pan structure with protective features. The compromise is in the balance in where more or improved ribs are disposed in the areas prone to impacts.


a

b

c

Figure 55 - Collection of random stones

7.2. Experimental testing

7.2.1. Materials and manufacture of oil pan samples

Oil pans samples were supplied by Eaton Corporation (UK) using material grades PA66-GF35 and PA66-i-GF35 respectively BASF Ultramid® A3HG7 and A3ZG7. Details about each polyamide grade are outlined in section 3.2.1. Oil pans were manufactured using injection moulding. Details

of the injection moulding process are described in section 2.2.3. The design of the oil pan is made in such a way that its connection to the engine is consistent with the metal construction previously used. A distinguishable element of the design is the ribbing pattern which provided increased stiffness. Ribs are part of the oil pan and are not meant to snap, however, damage such as crushed or deflected ribs are acceptable at high impact energy.

Figure 56 shows an early version of the oil pan made with PA66-GF35. This oil pan weights around 2.4 kg. Overall dimensions are 580 × 300 × 75/160 mm. Thickness of the base wall is 3 mm. Ribbing heights varies from 6-20 mm, ribbing thickness is 2 mm, rib spacing varies from 5-30 mm.

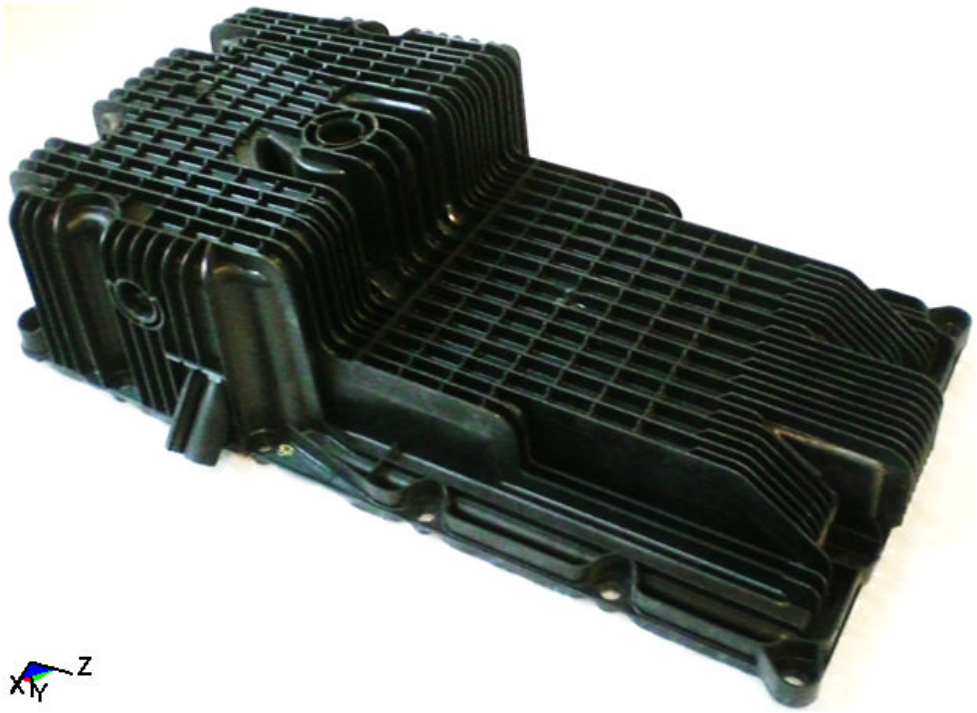

Figure 56 - Early version of the oil pan

Figure 57 shows the last improved version of the oil pan made with PA66-i-GF35. This oil pan weights around 2.8 kg. Overall dimensions are 580 × 300 × 60/205 mm. Thickness of the base wall is 3 mm. Ribbing heights varies from 10-20 mm, ribbing thickness is 2 mm, rib spacing varies from 5-15 mm. Despite the increased density of ribs, the weight difference with the early version is only 400 g thanks to a more homogeneous overall shape and with reduced rib height.

Figure 57 - Improved version of the oil pan

7.2.2. Mechanical testing and conditions

Experimental impact tests are carried out using a drop weight tower and a gas gun. The drop weight tower has been conducted by adjusting the height of a 10 mm hemi-spherical tip impactor (3170 g total falling weight) to the desired impact energies. Gas gun impact tester employs a 10 mm hemi-spherical projectile and has been conducted by adjusting the pressure in the gun to reach the desired impact velocities. The projectile and impactor were chosen according to the collection of random stones presented in Figure 55. A picture showing side-by-side, projectile, impactor and reference stone was provided in Figure 4, section 3.2.2.

Single impacts at room temperature of 20-23°C of energy range from 3-12 J at 90° to surface (maximum impact energy compared to an impact at an angle) are investigated on dry-as-moulded oil pans. The age of the mouldings vary from 1 to 3 months. Impact energies, for the reference stone or projectile, represent a driving speed from 50-120 km/h. Targeted positions are all around the oil pan, on flat walls, on ribs and between, and on groove walls. Each position has been impacted 10 times on 10 different samples. Oil pans are tested bolted on a steel plate and clamped to the test fixture. Oil pans do not contain oil or welded part. Impact resistance specifications are 7 J for sidewalls and 12 J for bottom walls facing the road.

Broken off fragments of the oil pan during testing were examined under Scanning Electron Microscope (SEM) to observe fracture mechanisms.

7.3. Finite element analysis

Simulation impacts on the oil pan were conducted using experimental data. Early design model (80468 shells) and improved design model (118205 shells) were meshed at density 1 element per 3 mm. Thickness of the part is 3 mm for the wall and 2 mm for the rib. Models are constrained in all directions on their sealing edges. Simulation settings are outlined in section 3.2.2.

7.4. Results and discussion

Figure 58 shows the early version of the PA66-GF35 oil pan with key areas highlighted. Gas gun tests results are:

- Areas in (A) are covered with flat walls, groove walls (25 mm diameter) and walls with Y-axis ribs (spacing 10 mm, height 6 mm). Areas in (A) must resist to a 7 J impact. However, 80% of flat walls failed at 3 J because walls are directly exposed; 100% of groove walls failed at 3 J because concave shape are fragile and uncovered; and

60% of walls with Y-axis ribs failed at 7 J with damaged ribs because impacts between ribs can be directly reached by the projectile.

- Bottom walls in (B) are covered with ribbing mesh pattern (Z-axis ribs height 10 mm, spacing 15 mm; X-axis ribs height 5 mm, spacing 25 mm). Areas in (B) must resist to a 12 J impact. However, in the low density ribbing area 60% of walls failed at 12 J because of rib spacing too large; and in the high density ribbing area 20% of walls failed at 12 J at the bottom of the rib.
- Walls in (C) are represented by Y-axis ribs, flat and groove walls. Areas near the pick-up oil channel feature must resist 7 J but 40% of walls failed especially nearby uncovered sharp angles. Areas near the cylinder feature must resist 12 J but 80% of walls failed because of uncovered concave walls, tall ribs easily snapped and a lack of dense ribbing pattern. Transitions between areas (C) and (B) are at 90° and characterise zones of stress concentration.
- Walls in (D) are covered with Y-axis ribs (spacing 15 mm) and groove walls. Area in (D) must resist 7 J. However 60% of ribbed walls failed because of rib spacing too large; 80% of groove walls failed because of uncovered concave walls.

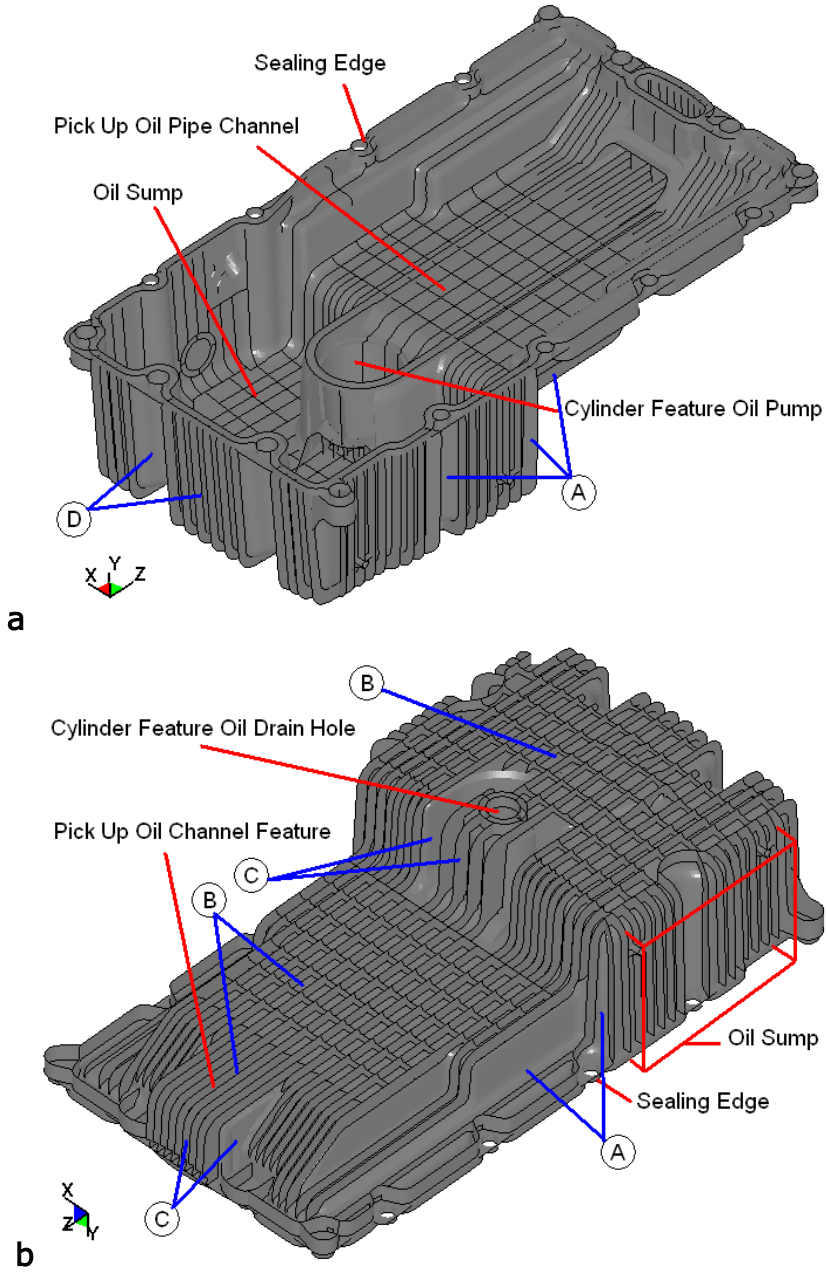

Figure 58 - Early version of the oil pan and key areas, a) inner view, b) outer view

Impact resistance results of the early version of the oil pan are rather alarming. Figure 59 and Figure 60 show typical failures encountered in each area. Figure 59 displays crack failures in Area A, impact between two ribs, and in Area D, impact in a concave groove wall. Figure 60 displays broken ribs and perforation in Area B and crack (sharp junction between surfaces) and perforation (concave cylinder feature) in Area C. Almost all causes of failure were taking place on exposed areas, on unprotected walls and where the rib spacing is too large. Other failures were spotted on sharp transitions between surfaces resulting in long scale cracks along the separating line between each surface. Unprotected concave groove walls are weak features in composite as found in the preceding Chapter 6. Finally, 95% of ribs higher than 15 mm were snapped. Tall ribs are not sufficiently stiff, they deflect too much which cause the removal of long portion of ribs whilst impacted. 90% of failures were cracks, 75% of them were only visible on the inner side of the oil pan and 15% were visible on both side of the wall. The rest 10% were perforations of the wall.

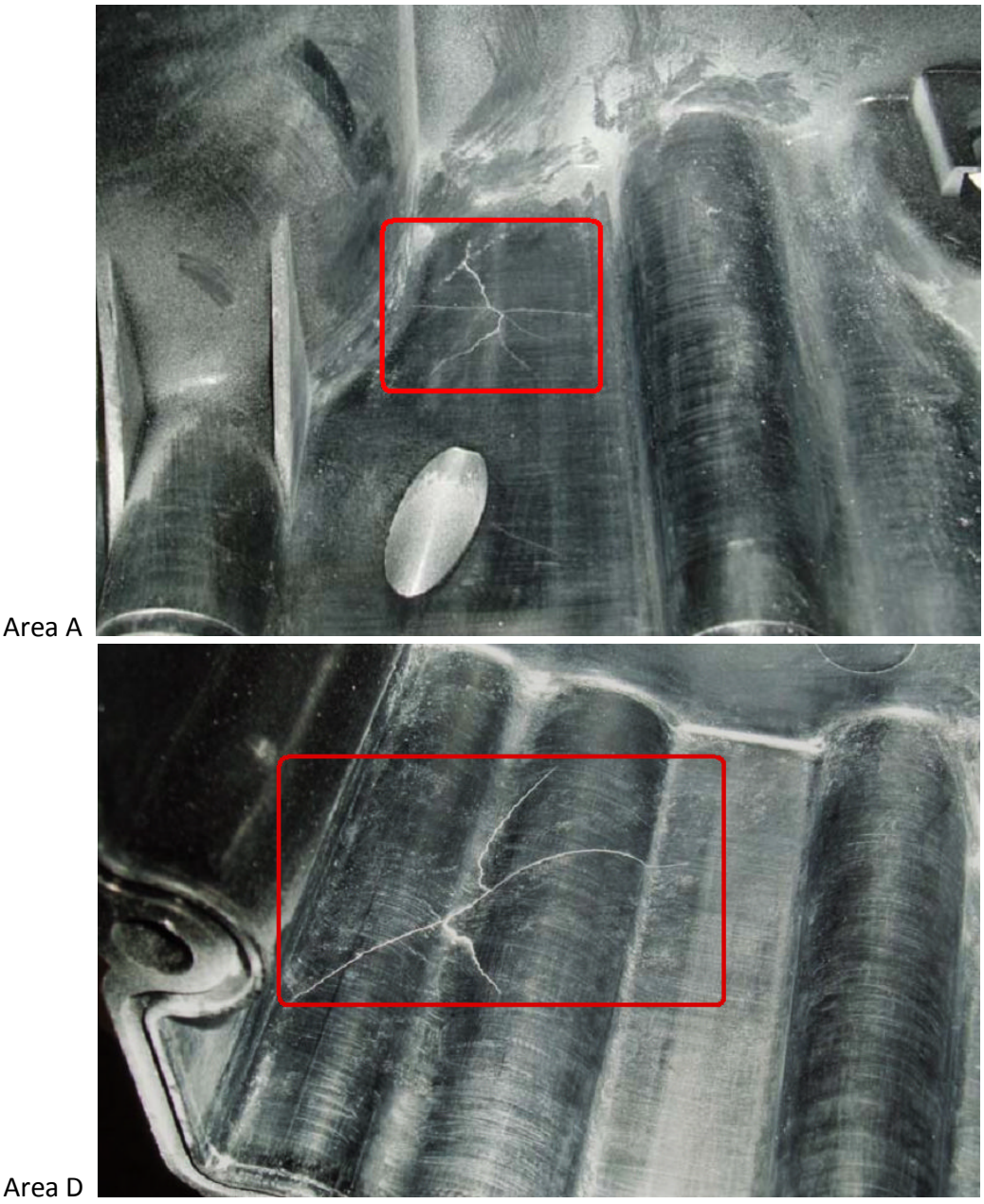

Figure 59 - Typical failures encountered in Area A and Area D

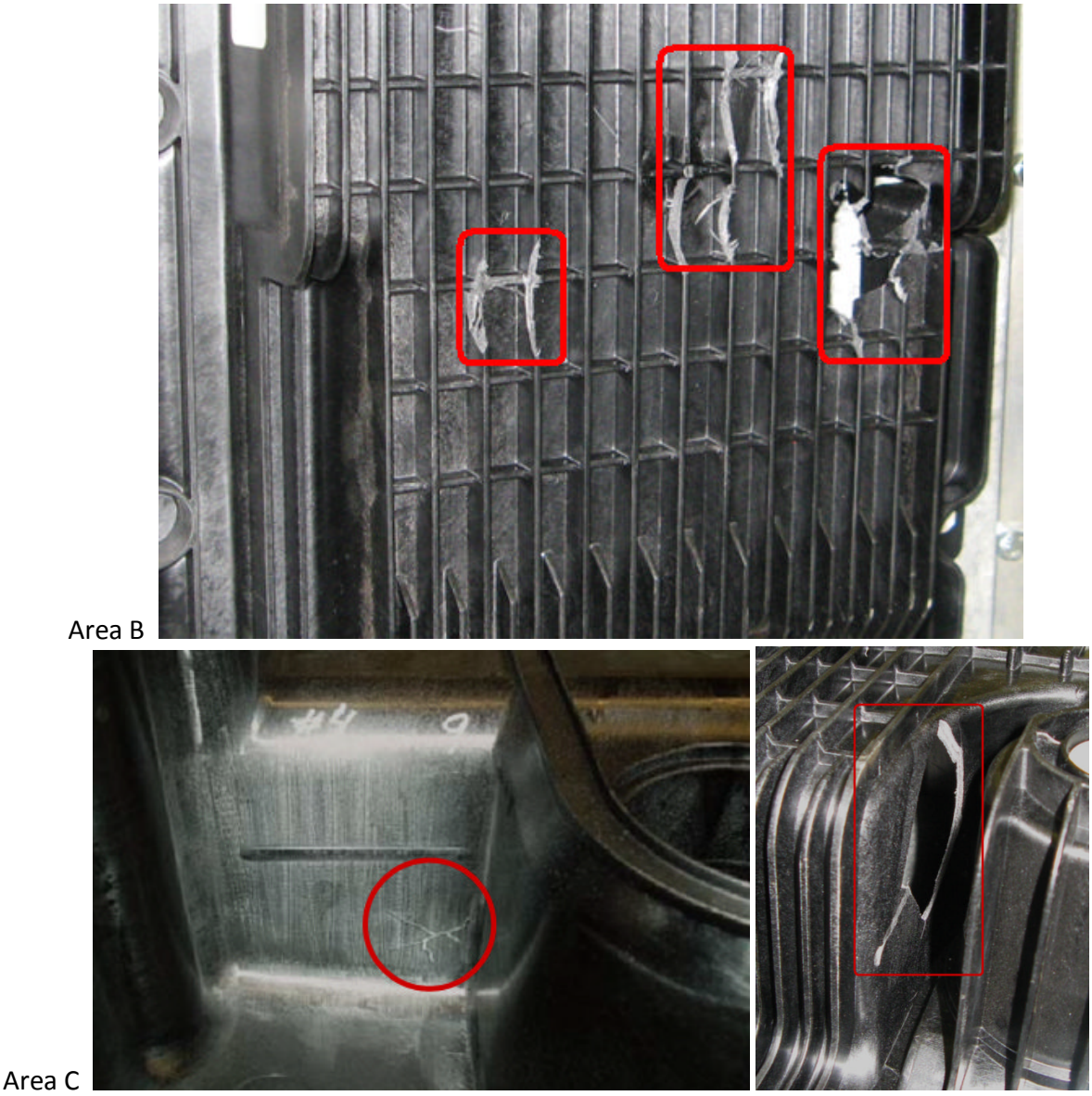

Figure 60 - Typical failures encountered in Area B and Area C

A broken off fragment from the Area B (PA66-GF35) was put under SEM observation. The magnification of the following Figures varies from 200-4000. In Figure 61, the two constituents characterising the composite are

clearly distinguishable that is to say short glass fibres and matrix resin wrapping the fibres. The picture reveals that there is a wide range of fibres pointing in one general direction, the direction of the injection moulding flow (skin area). At magnification of 200, fibres mostly appear uncut (average length of 300 μm), some are uncoated but they seem unaltered whilst the matrix is unevenly distributed with some bits peeled or detached. Besides, fibres emerging from the fractured surface have been displaced and are completely de-bonded from the matrix precisely because of a lack of matrix. Unmistakably, it is a sign of a matrix cracking failure.

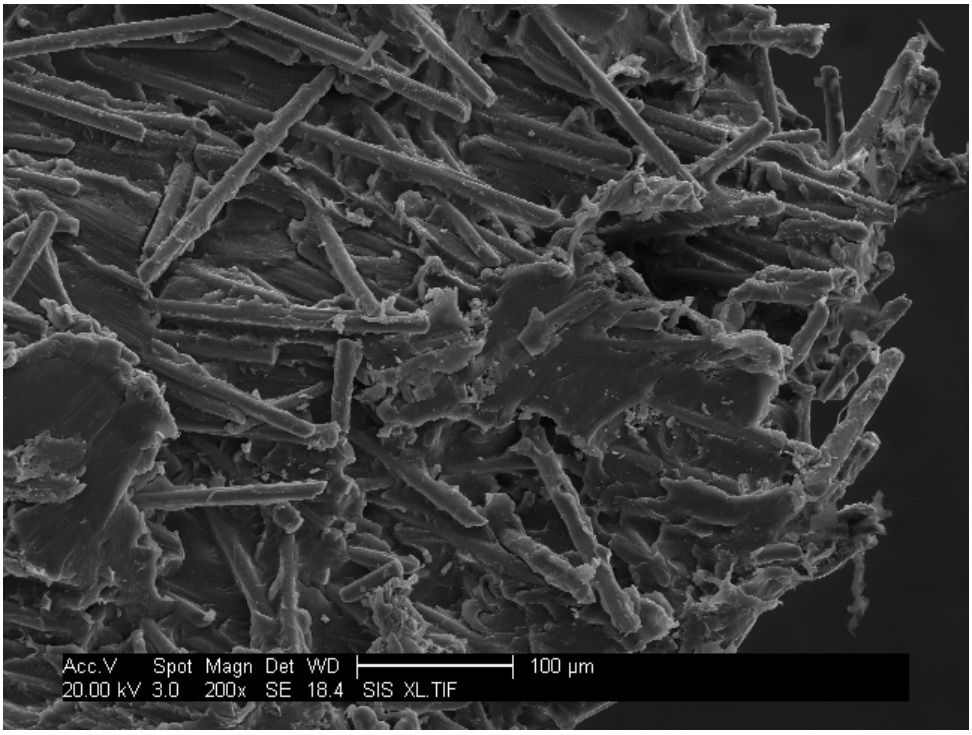

Figure 61 - Matrix cracking failure at magnification 200

When the area towards the centre of the fragment is magnified, we observe other types of failure, but they are still localised in the impact point area. At magnification of 400, Figure 62 shows failures surrounding the impacted surface. Both matrix and fibres have failed. The picture illustrates a net cut section of each material constituent. In this area, compression stress acted more than tension stress. Fibres are shorter than normal (<50 μm) and are also randomly dispersed (core area). They are also few holes and hollows caused by fibres pulling out of the matrix but for the major part, matrix and fibres remained linked together.

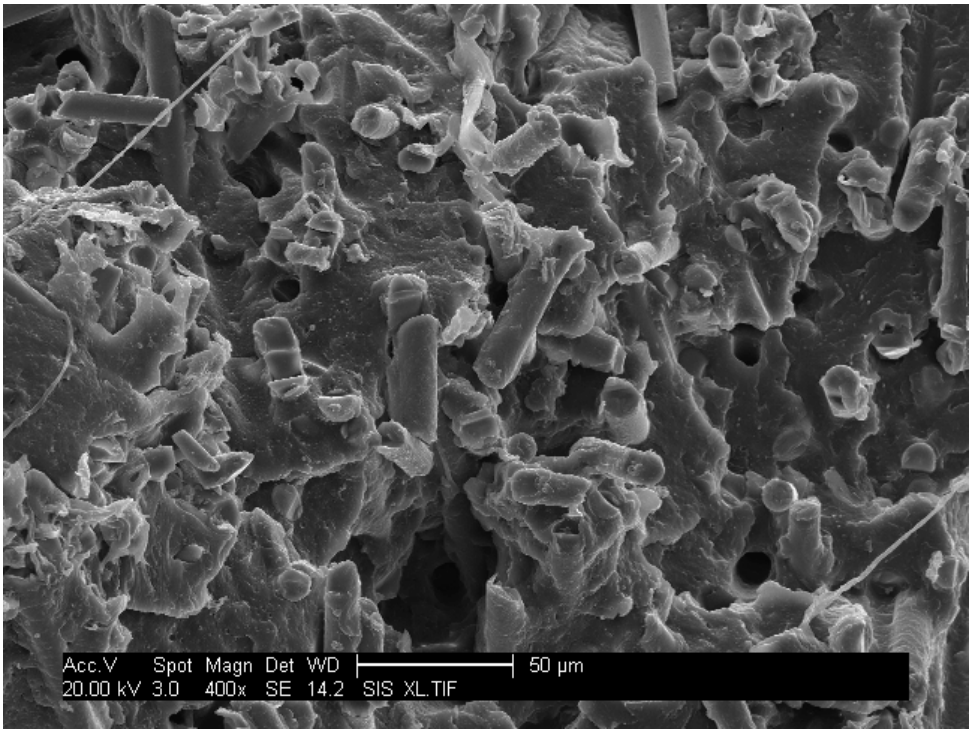

Figure 62 - Matrix cracking, fibres fracture and limited fibres pull out at magnification 400

At the same magnification of 400, Figure 63 shows failures taken from the backside of the impacted surface. Many hollows are visible from where fibres were filling them and also many uncoated fibres can be spotted. In this region of the fractured surface, the bond between fibres and the matrix has yielded first. This finding illustrates the fact that in this area of the sample tension stress is bigger than compression stress. The system de-bonds and fibres are pulled out of the matrix during fracture. Noticeably, the matrix has failed in its function. Fibres seem to have one general direction which confirms that the area is in the skin section of the sample (skin-core morphology during injection moulding).

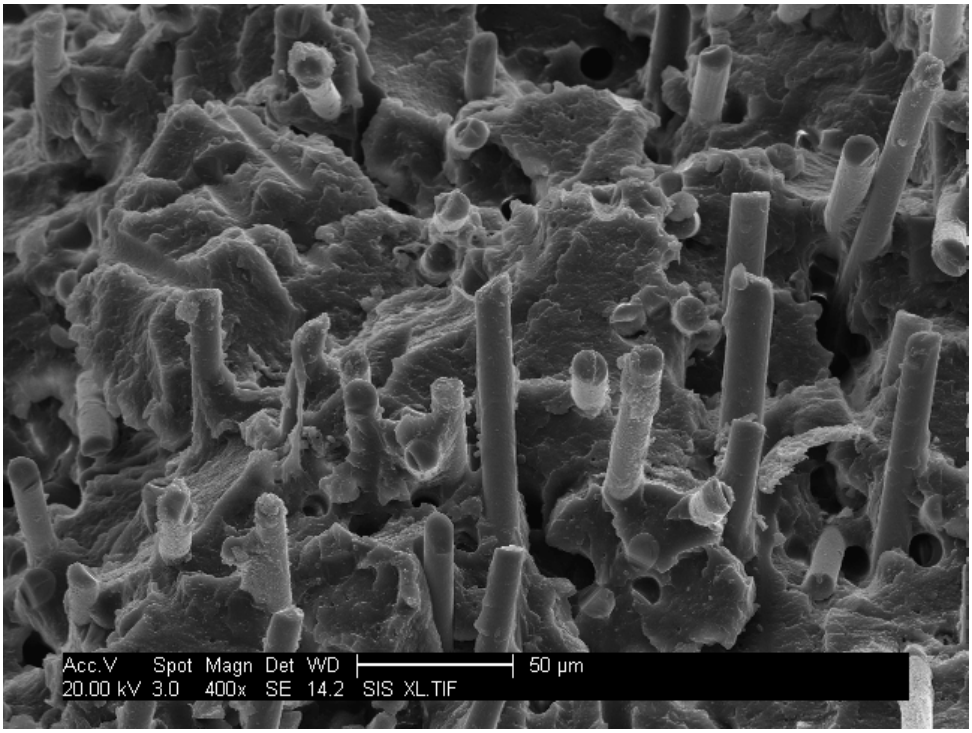

Figure 63 - De-bonded and pulled out fibres at magnification 400

Figure 64 shows one end of a fibre which presents a tear on its surface probably resulting from a failure across the diameter of the fibre. The fractured fibre was perpendicular and in line with the general direction of the impact. The stress was so intense that it has removed the matrix and split the fibre in two with a peeled chip still attached to the fibre. Chopped fibres in their major part present a bevel-shaped fracture. For a matter of comparison, another fibre is visible at the bottom background that presents a clean flat end surface. Furthermore, the base of the matrix where the ruptured fibre is attached displays also a fissure.

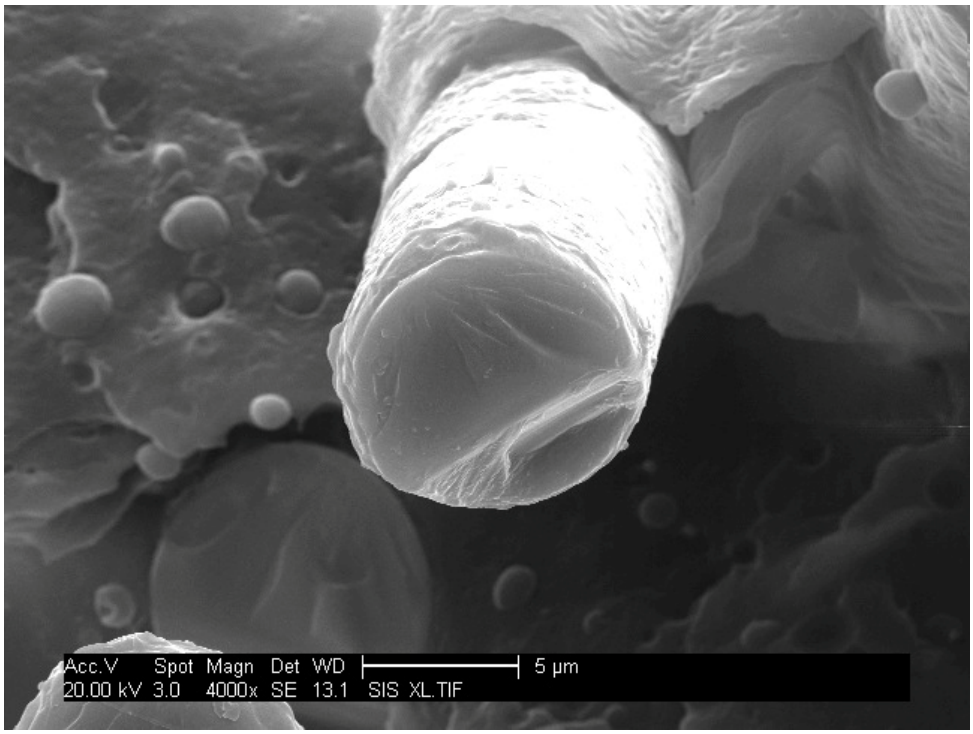

Figure 64 - Close-up of a fibre fracture at magnification 400

Figure 65 shows the latest improved version of the PA66-i-GF35 oil pan with key areas highlighted compared to the early version. Gas gun results are:

- Areas in (A) that were found weak received improvements. Flat walls are now covered with Y-axis ribs spaced by 8 mm (10 mm from the centre of each rib). Groove walls are reinforced by layered ribs from 10-5 mm in height around them. The pattern of ribbed walls was made denser with rib spacing of 8 mm and height of 10 mm. At 7 J, the only damage observed was crushed ribs by 2 mm maximum.
- Bottom walls in (B) received a denser ribbing pattern with homogeneous rib height of 10 mm (rib spacing in Z-axis is now 8 mm and 15 mm in X-axis). At 12 J, the base wall was never directly touched and no visible cracks were found.
- The main improvement in areas in (C) concerned the transition between the sump and the pan especially at the bottom transition. Instead of being at 90° which were zones of stress concentration, they are now presenting a smooth rounded transition. This chamfer allows a better distribution of the effort in a much wider surface area. Another chamfer or recess was introduced on the transition edges to accommodate the height difference. The cylinder feature found in the

previous design was extremely weak with large rib, large spacing and unprotected concave grooves. It was removed and the oil drain hole was moved off-centred to a position where it was feasible to integrate it. The pick-up oil channel is not straight anymore and has an S-shape look in accordance with the move of the drain hole. The other improvements are similar to areas in (A). No wall is left uncovered and Y-axis ribs were increased in density around grooves. The transition between sump and pan contains two X-axis ribs across the denser Y-axis ribs (spacing 8 mm). This was intended to reduce the broken-off fragments of ribs. At 7 J, no failure is visible, only marks, scratches or small crushes (1-2 mm). At 12 J, some Y-axis ribs are likely to be crushed (by 2-3 mm) but again no failures are observed.

- Walls in (D) received same improvements as in (A). Reduction of the rib spacing (8 mm), Y-axis ribs height to 10 mm, and grooves protected with layered ribs (10-5 mm height).

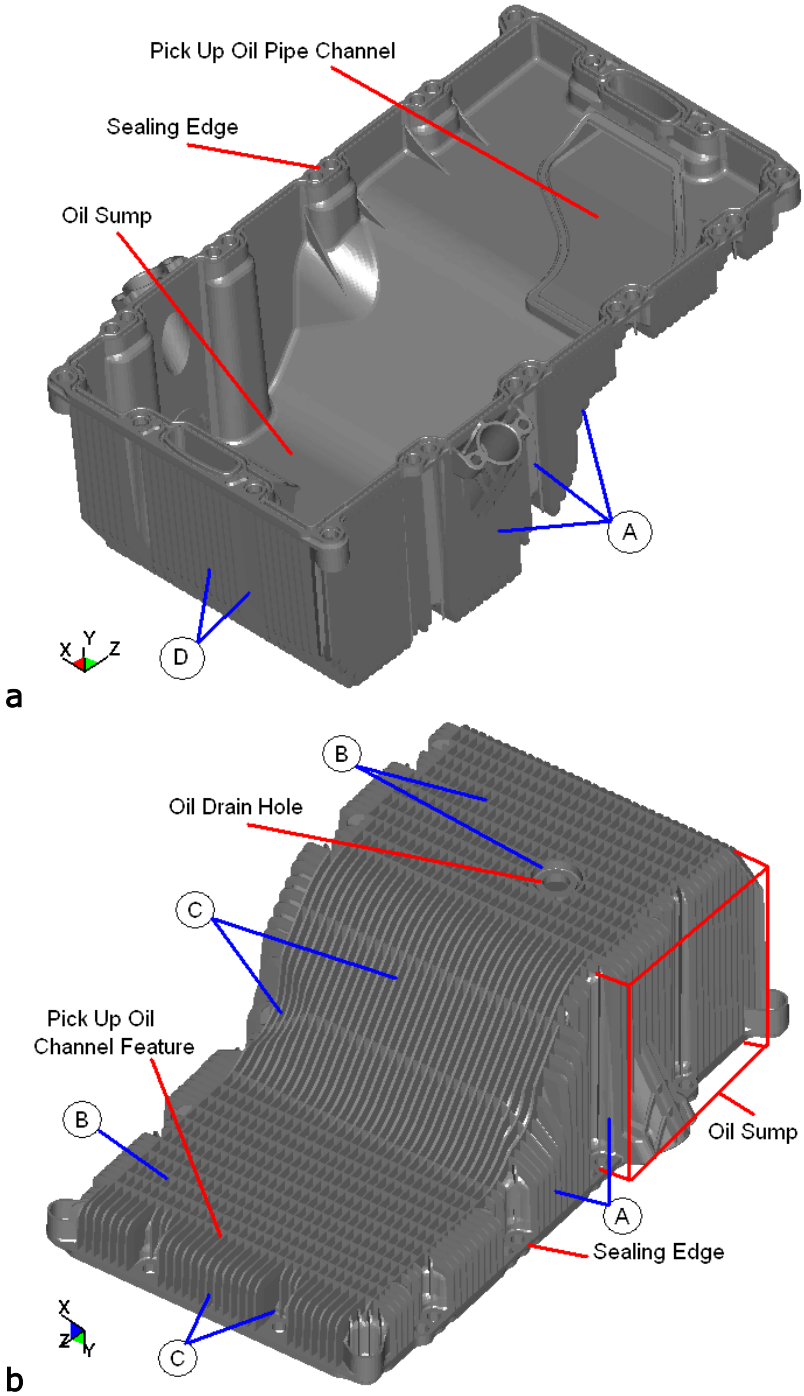

Figure 65 - Improved version of the oil pan and key areas, a) inner view, b) outer view

Figure 66 shows forces histories of each structure impacted at 3 J (drop tower) in the middle of a rib spacing in Area (B) on the pan section. In the early version, Z-axis ribs height is 10 mm and X-axis ribs height is 5 mm; spacing between Z-axis ribs is 15 mm and between X-axis is 25 mm. Therefore a 10 mm surface impact directly hits the wall. In the improved version, Z-axis and X-axis ribs heights are 10 mm and spacing between Z-axis ribs is 8 mm and between X-axis ribs is 15 mm. Consequently, a 10 mm surface impact inevitably hits the ribbing. The 3 J impact on the early version can be described as follows, between 0-3 ms, the wall deflects. At 3 ms, the maximum deflection is reached for the given impact. From then, the wall pushes back the impactor. The 3 J impact on the improved version has a different scenario. The impactor touches the two Z-axis ribs which resist and slightly deflects till 2.4 ms. From then, ribs deflect and the impactor slightly penetrates in between thus the fall in the force. At 2.6 ms, ribs start to stop deflecting and at 3 ms the walls of the ribs begin to push back the impactor. The oscillation in the force can be interpreted by successive returns between each rib wall. At 3 J, no failure is observed on each structure.

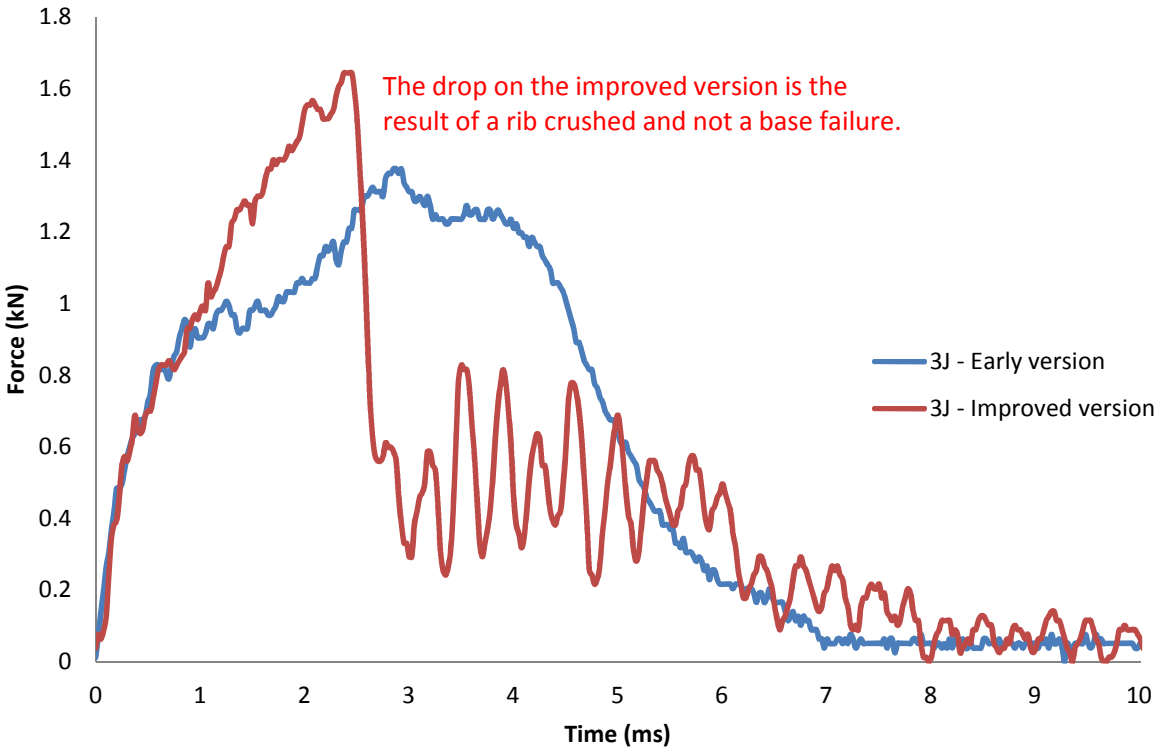

Figure 66 - Forces histories for each design at 3 J

Figure 67 shows force histories of each structure impacted at 7 J (drop tower) in the same area as before but on other samples. In the 7 J impact on the early version, the wall deflects and begins to show signs of damage at 2.4 ms till it eventually fails at 3.5 ms. Crash appeared on both sides of the wall. In the 7 J impact on the improved version, the two ribs are successively touched and crushed till their walls stop to crush at 0.75 ms. From then, they resist, deflect and push back the impactor. No failure is visible on the wall but only damaged ribs. Figure 68 illustrates an example of a 3 mm crushed rib on the pick-up oil channel feature.

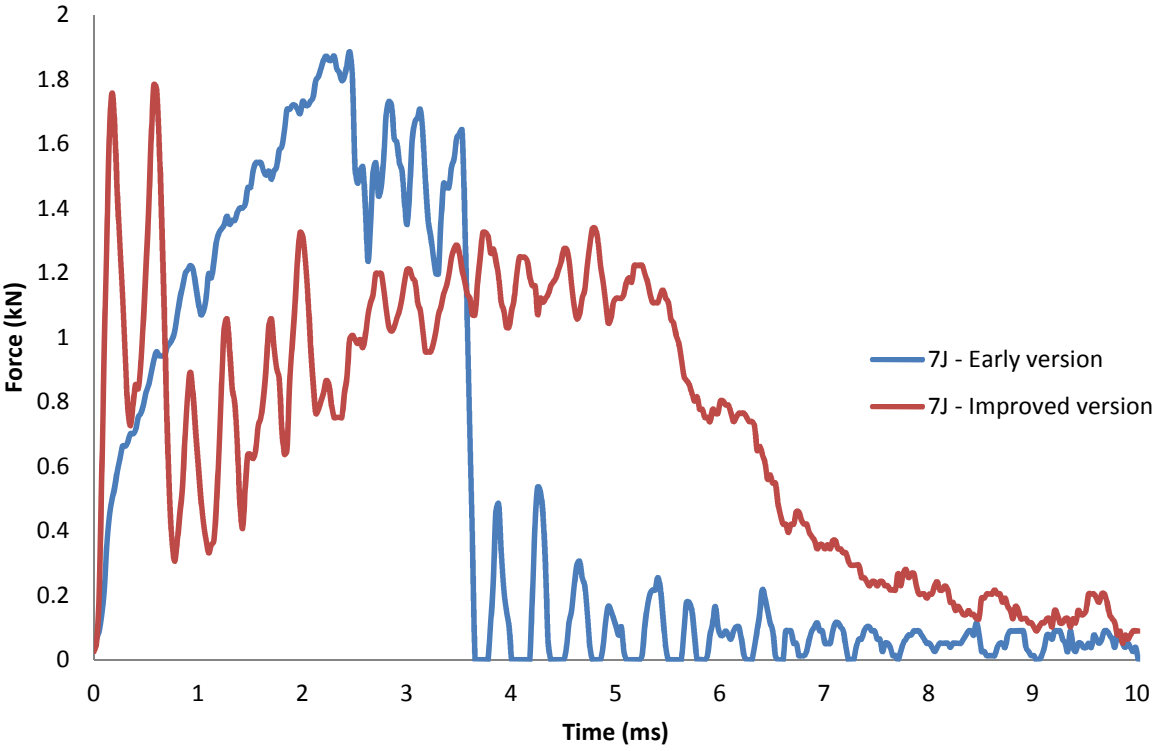

Figure 67 - Forces histories for each design at 7 J

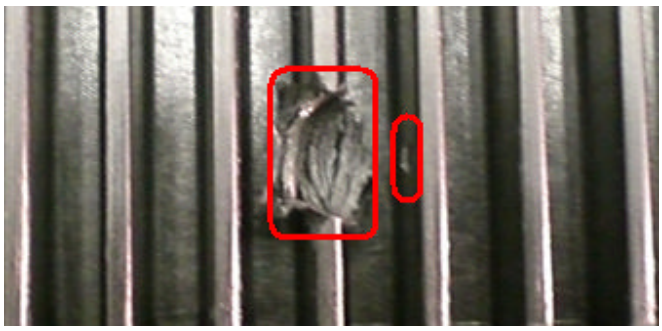

Figure 68 - Rib crushed after impact on rib at 7 J (PA66-i-GF35)

Figure 69 shows the correlation between 7 J experimental and simulated impacts on the same location of the improved version (PA66-i-GF35). The general look of each curve appears similar. However, forces in the model are overestimated at the beginning of the impact and underestimated towards the end. The model predicts around 20% more strength (2.15 kN instead of 1.76 kN) when the impactor tries to penetrate between the ribs and around 60% less towards the end (0.5 kN instead of 0.8 kN). However, the order of magnification is correct and the model can be used to approximate the impact behaviour of the oil pan.

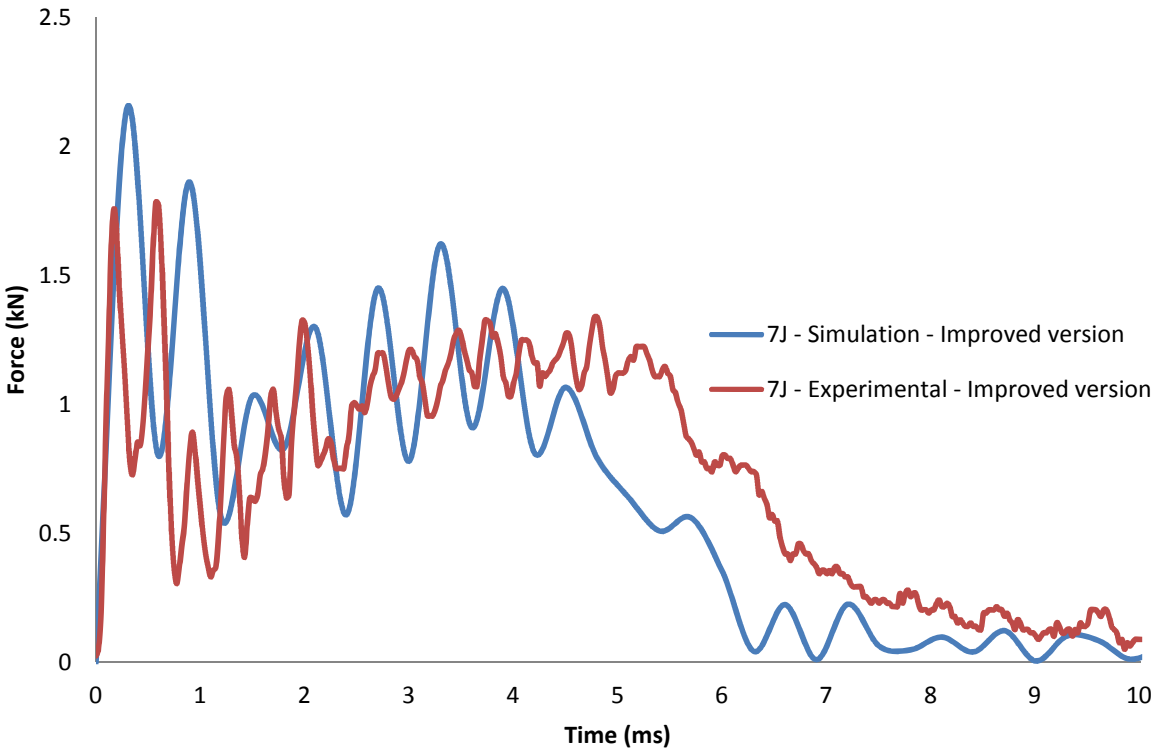

Figure 69 - Experimental and simulation forces histories on improved design at 7 J

Figure 70 shows a 10 mm projectile impact sequence at 14 m/s with shock waves stress distribution propagating in circle away from the impact spot. At t_2 when shock waves reach sharp edges, an accumulation of stress is created. The impact occurs in the base wall and the ribbing restrains the wall to deflect to a certain extent. The ribbing plays a major role in the stress distribution and my findings match other previous studies [195; 196].

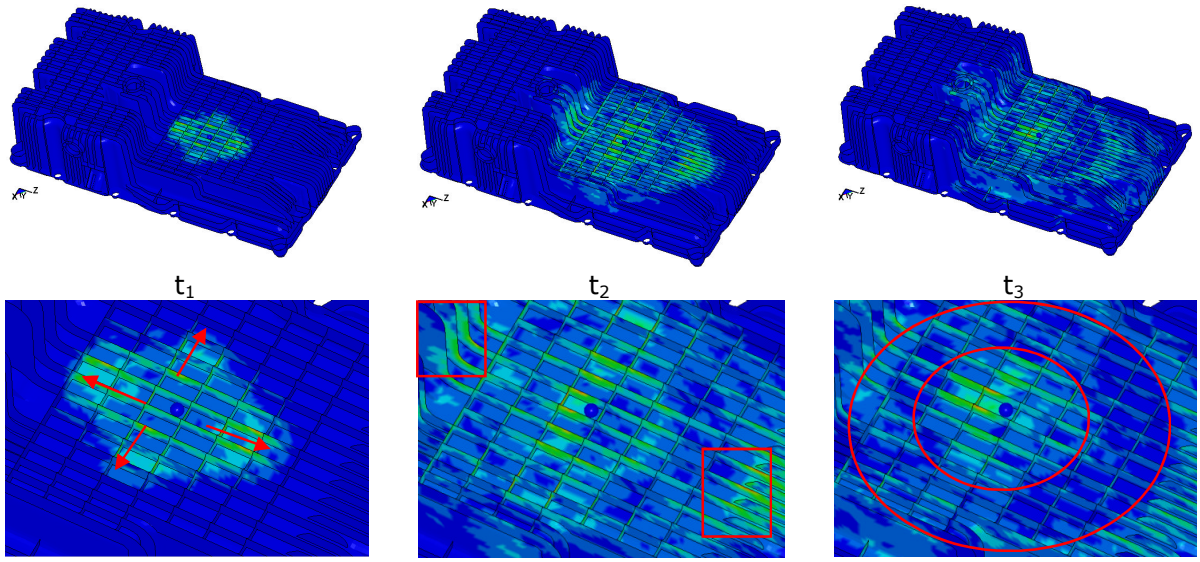

Figure 70 - Evolution of the stress undergone by the oil pan structure

7.5. Conclusions

Impact performance were realised on different oil pan design. Investigations of weak areas of the early version were identified such as, sharp surface transition which are stress concentration zones, unprotected areas displaying the base wall (concave grooves, flat walls), the oil cylinder feature which presents sharp angles, unprotected walls and tall ribs. From then, improvements were added on the design which led to the latest version. The improvement of the design was taking into account different elements of the engine surrounding the oil pan. Sharp angular surface transitions are made rounded. The oil cylinder feature was removed and the oil drain hole was moved to a compatible location. Therefore the transition between the sump and the pan is made with the same wall which also received stiffening rib lines. The surface transition between sump, pan and their respective side walls are accommodated by creating a curved recess on the edge. Uncovered walls needed protective ribbing feature. The reduction of the rib spacing or densification of the ribbing led to higher impact performance. The standardisation on the rib height permitted better distribution of the impact. In terms of materials, the toughness of PA66-i-GF35 allows more progressive deformation or damage of ribs (crushing) instead of brittle behaviours of PA66-GF35 ribs which were easily broken up. The improvement on the latest version of the oil pan did not show a sign of

failure on the base wall. This new version is optimum in terms of impact resistance thanks to the design of the structure and the optimised stone impact material. Impact simulations were found to give good correlations with impact experiments. However, when the impact induces material response close to its yielding point, the outcome can be slightly over or underestimated by 10-15%. Nevertheless, it was found as well in the experiments that the yield on the structure has to be considered with a 0.5-1 J margin. Therefore specifications were taking this parameter into account.

SEM analysis on PA66-GF35 showed that fibre-matrix interface rupture is observed. The damage is characterised by matrix plastication, matrix micro-cracks, fibre pull out and fibre fracture. Localised impact against the composite wall acts like a dynamic flexion with characteristic tension failure on the backside and compression failure on the impacted side. Once the projectile enters in contact with the wall, the wall quickly starts to undergo deformation, bends and eventually fails if the impact intensity is higher than the wall can cope. The excess of energy in the structure is evacuated through tension stresses that make the matrix to crack and the interfacial to break. Cracks were always found initiated on the backside of the impacted wall and can propagate towards the impacted side if the impact energy is sufficiently important.

Chapter 8. Conclusions and future work

8.1. Conclusions of the thesis

Glass reinforced polyamides 66 have good intrinsic mechanical properties that make them attractive to use in structural components. However, they also have some drawbacks. They were found sensitive to moisture and salt uptakes, very sensitive to temperature ageing and air oxidation. Those parameters have detrimental effects on impact performance. Nevertheless, the good flow property of the PA66 resin enables long flow distances allowing making reliable molding of complex thin-walled sections. The addition of ribs at the edge of the pan wall increases stiffness and strength of the component. Furthermore, brittle failure introduced by the addition of glass fibers can be reduced by the addition of rubber particles. The rubbery phase is blended intimately with the matrix which makes the material tougher enabling better elongation and impact performance. The impact loading response of glass reinforced polyamides 66 and the way the incident impact energy is dissipated is far different to that of metals. For Cantwell et al. [17] at low and intermediate incident energies, metals absorb energy through elastic and plastic deformation. Although the latter may cause some permanent structural deformation, its consequences on the load-carrying capability of the component are usually small. At high

incident impact energies, target perforation may occur and the passage of the impactor will generally result in petalling, cracking and spalling. Such damage degrades the load-bearing ability of the structure but its effects can generally be predicted using fracture mechanics principles. In studied composites however, the ability to undergo plastic deformation is extremely limited with the result that energy is frequently absorbed in creating large areas of fracture with ensuing reductions in both strength and stiffness. Furthermore, the prediction of the post-impact load-bearing capability of a damaged composite structure is more difficult than for metals since the damage zone is generally complex in nature and consequently very difficult to characterise. Furthermore, identical impact on a given target may have variable outcomes when the intensity of the impact is relatively close to the material failure limit. It is therefore essential to have a careful approach and to consider a security margin when assessing the impact performance of composite components.

8.2. Contributions of the present work

From the original design of the oil pan, some weaknesses have been found. Most of them were wall surfaces not sufficiently protected or stiffened against localised impact loadings. These weak areas were flat walls, grooves, incorrect configuration of the ribbing (height), or lack of ribs (concentration).

Other issues concerned abrupt edges between surfaces and also inappropriate design features such as the oil cylinder drain. Figure 71 presents the evolution on the oil pan design. The weight difference between each version, 2,4 kg for the early version against the 2,8 kg for the improved version is not a problem because it is completely optimized. Furthermore, the weight of a comparable die-casted oil pan is still significantly higher (around 55 to 60% more). Visually, the improved version has a smoother structure with reduced sharp corners and the colour of the part is matte black instead of shiny black.

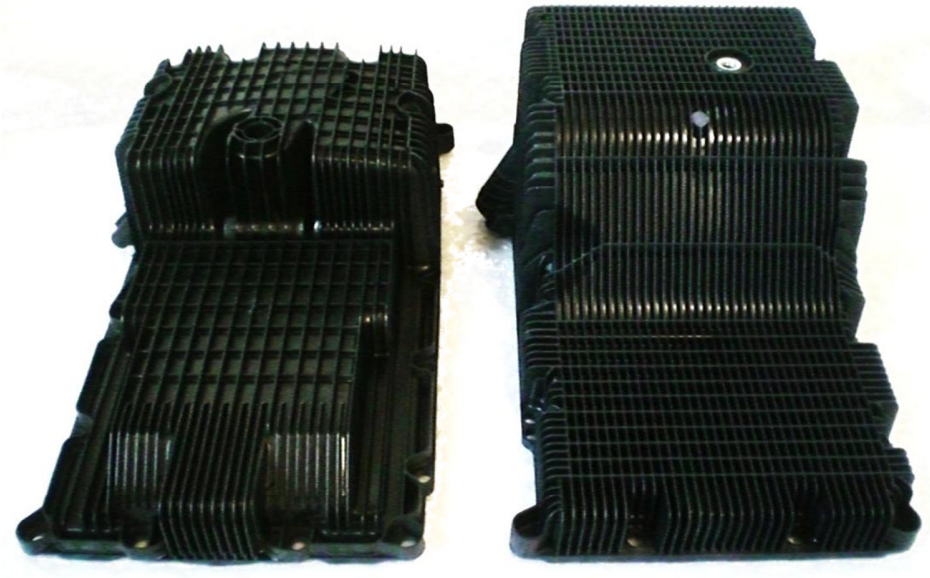

Early version Improved version

Figure 71 - Improvements on the oil pan design

The identified weakness areas were improved by covering the oil pan with a homogeneous and dense ribbing network. Abrupt edges were made curved and exposed features were integrated in a better position. Moreover, the rubber toughened glass reinforced polyamide 66 (PA66-i-GF35) is a material that has been specifically developed in collaboration with industrials (including BASF and Eaton Corporation) to fulfill the request in terms of impact improved material with better impact resistance at low temperature. The brittle to ductile temperature transition is lowered and therefore improves the toughness in the material. PA66-i-GF35 has a larger elongation to failure than PA66-GF35 and despite having lower tensile modulus and strength its impact resistance is significantly better. After series of impact tests, the latest design of the oil pan associated with a superior impact modified material has successfully passed the specifications imposed in terms of impact performance. That is to say, the ability to resist impact stones with kinetic energy range from 7-12 J.

The simulation modelling approach proposed is relatively simple to implement and gives good correlations of the relation between the structure and the material (more information in Appendix 4). Experimental data were used to validate the impact simulations and simulations were employed to predict component and material behaviours. As for the experiments, the impact simulations require the consideration of an error margin (±1 J) when the material failure limit is approached. The model is rigid as the failure

criterion is clearly defined. Furthermore, the model does not accommodate significant change in the impact parameters. Therefore, data implemented should be in accordance with the test performed.

Other under-the-hood parts could also benefit from this research work such as radiator end tanks, air intake tubes and gearbox covers (see Figure 72). The understanding acquired in the experimental program on the oil pan is replicable to other structural components. The contributions to knowledge are:

- A better understanding of the glass reinforced polyamide material in terms of mechanical properties and impact resistance along with the development of an improved impact material with the material supplier.
- The development of a material model and an extensive material database created from the experiments. This has allowed the relationship between structure and material property (intrinsic property of the material, of the structure and the combination of these properties) to be understood.

Radiator End Tank EGR / Air Intake Tubes

Figure 72 – Automotive composite plastic parts

8.3. Suggestions for future work

Investigations in this research work were focused on the understanding of polyamide 66 grades under several conditions and assess their influence on their mechanical properties. Except at 3 J where repeated impacts where performed, single localised impact were mostly achieved as the consideration of failure or damage is difficult to quantify. Consequently impact specifications were done at most to critical levels: 90 degree to surface, small tip for the projectile, high impact energy. However, further researches can investigate repeated impacts and its consequences on the progression of the damage. Other work can drop the entire oil pan in order to simulate engine manoeuver during maintenance as the oil pan may have to support the entire weight of the engine on its top. Further research can investigate the variables angles of impact or crash impact against a rigid wall or assess the friction welding strength of the oil pan module (see Appendix

5). Finally, the component can be tested in more realistic conditions with elevated temperature and with oil in the sump taking into account the ageing effects on the impact performance of the part.

Contributions to the thesis

Publications

Published: Mouti, Z.; Westwood, K.; Kayvantash, K. and Njuguna, J. (2010) "Low Velocity Impact Behavior of Glass Filled Fiber-Reinforced Thermoplastic Engine Components", *Materials*, vol. 3, no. 4 2463-2473

Published: Mouti, Z.; Westwood, K.; Long, D. and Njuguna, J. (2011) "Finite Element Analysis of Localized Impact Loading on Short Glass Fiber-Reinforced Polyamide Engine Oil Pan Subjected to Low Velocity Impact from Flying Projectiles", 8th European LS-DYNA Users Conference, Strasbourg, May 2011

Published: Mouti, Z.; Westwood, K.; Long, D. and Njuguna, J. "Finite Element Analysis of Glass Fiber-Reinforced Polyamide Engine Oil Pan Subjected to Localized Low Velocity Impact from Flying Projectiles", Steel Research International, August 2012

Submitted: Mouti, Z.; Westwood, K.; Long, D. and Njuguna, J. "An Experimental Investigation into Localised Low Velocity Impact Loading on Glass Fibre Reinforced Polyamide Automotive Product", International Conference on Mechanics of Nano, Micro and Macro Composite Structures, Torino, June 2012

Presentations in conferences

Mouti, Z.; Westwood, K.; Kayvantash, K. and Njuguna, J. "Impact resistance of a thermoplastic oil pan module", Low Carbon Vehicle Event, Millbrook Proving Ground, September 2009

Mouti, Z.; Westwood, K.; Long, D. and Njuguna, J. "Finite element analysis of localized impact loading on short glass fiber-reinforced polyamide engine oil pan subjected to low velocity impact from flying projectiles", 8th European LS-DYNA Users Conference, Strasbourg, May 2011

Mouti, Z.; Westwood, K.; Long, D. and Njuguna, J. "Experimental Investigations on Localized Low Velocity Impact Loading on Glass Filled Polyamide for Automotive Parts", European Congress and Exhibition on Advanced Materials and Processes - EUROMAT 2011, Montpellier, September 2011

Mouti, Z.; Westwood, K.; Long, D. and Njuguna, J. "An Experimental Investigation into Localised Low Velocity Impact Loading on Glass Fibre Reinforced Polyamide Automotive Product", International Conference on Mechanics of Nano, Micro and Macro Composite Structures, Torino, June 2012

Industrial reports

Njuguna, J. and Mouti, Z., "Falling Weight Impact Performance of Automotive Thermoplastic Pans", Cranfield University report OP-FW01 for Eaton Corp., January 2009

Njuguna J., Mouti, Z., Long, D. and Westwood K., "Falling Weight Impact Performance of Automotive Thermoplastic Oil Pans", Cranfield University report OP-FW02 for Eaton Corp., February 2009

Njuguna J., Mouti, Z. and Long, D., "Air Gun Impact Performance of Automotive Thermoplastic Oil Pans", Cranfield University report OP-AG01 for Eaton Corp., June 2009

Njuguna J. and Mouti, Z., "Analysis Method for Predicting Structural Response of Thermoplastic Parts from Projectile Impacts", Cranfield University report OP-FE01 for Eaton Corp., March 2010

Njuguna J. and Mouti, Z., "Finite Element Analysis Impact Performance of Oil Pan Protective Geometries for Improving Impact Resistance Part 1", Cranfield University report OP-FE02 for Eaton Corp., Mai 2010

Njuguna J. and Mouti, Z., "Differential Scanning Calorimetry and Thermogravimetric Analysis of Thermoplastic Materials", Cranfield University report OP-FE03 for Eaton Corp., Mai 2010

Njuguna J. and Mouti, Z., "Finite Element Analysis Impact Performance of Elongated Structures for Improving Impact Resistance Part 2", Cranfield University report OP-FE04 for Eaton Corp., July 2010

Njuguna J. and Mouti, Z., "Environmental Scanning Electron Microscopy Study for Assessing Typical Failures of Thermoplastic Structures Subjected to Localized Low Velocity Impact", Cranfield University report OP-MC01 for Eaton Corp., August 2010

Njuguna J. and Mouti, Z., "Finite Element Analysis Impact Benchmarking of Structures Made of Different Thermoplastic Materials Subjected to Various Temperatures for Improving Impact Resistance Part 3", Cranfield University report OP-FE05 for Eaton Corp., September 2010

Njuguna J. and Mouti, Z., "Finite Element Analysis Ballistic Assessment for Structural Response Related to Projectile Size", Cranfield University report OP-FE06 for Eaton Corp., March 2011

Njuguna J. and Mouti, Z., "Mechanical Testing on Tensile, Flexural and Plaques Polyamide Samples – Part1 Quasi-Static Tests", Cranfield University report OP-QS01 for Eaton Corp., June 2011

Njuguna J. and Mouti, Z., "Tension Tests on Oil Pump Pickups to Evaluate Friction Weld Strength", Cranfield University report OP-QS02 for Eaton Corp., July 2011

Njuguna J. and Mouti, Z., "The Influence of Water and Salt Uptake on Impact Performance of Glass Filled Polyamide Plates", Cranfield University report OP-DT01 for Eaton Corp., October 2011

References

[1] Marsh, G. (2003), "Composites on the road to the big time?", *Reinforced Plastics,* vol. 47, no. 2, pp. 33-47.

[2] Sınmazçelik, T., Arıcı, A. A. and Günay, V. (2006), "Impact–fatigue behaviour of unidirectional carbon fibre reinforced polyetherimide (PEI) composites", *Journal of Materials Science,* vol. 41, no. 19, pp. 6237-6244.

[3] Flexman, E. A. (1979), "Impact behavior of nylon-66 compositions: Ductile-brittle transitions", *Polymer Engineering & Science,* vol. 19, no. 8, pp. 564-571.

[4] Ghosh, S., Khastgir, D., Bhowmick, A. K. and Mukunda, P. G. (2000), "Thermal degradation and ageing of segmented polyamides", *Polymer Degradation and Stability,* vol. 67, no. 3, pp. 427-436.

[5] Gijsman, P., Tummers, D. and Janssen, K. (1995), "Differences and similarities in the thermooxidative degradation of polyamide 46 and 66", *Polymer Degradation and Stability,* vol. 49, no. 1, pp. 121-125.

[6] Murphy, J. (ed.) (1998), *The Reinforced Plastics Handbook,* 2nd ed. ed, Elsevier Advanced Technology.

[7] Helps, I. G. (ed.) (2001), *Plastics in European Cars 2000-2008,* Rapra Technology Limited.

[8] Cummins Ltd, (2008), *Every Innovation, ISF Automotive Engines 109-167 PS*, Bulletin 4951315 ed., Cummins Inc, United Kingdom.

[9] "Thermoplastic oil pan has increased functionality", (2009), *Reinforced Plastics,* vol. 53, no. 6, pp. 9.

[10] "Oil tank on sport motorcycle resists heat and pressure", (2005), *Advanced Materials and Processes,* vol. 163, no. 8, pp. 60.

[11] Zhao, G. P. and Cho, C. D. (2007), "Damage initiation and propagation in composite shells subjected to impact", *Composite Structures,* vol. 78, no. 1, pp. 91-100.

[12] Bartus, S. D. and Vaidya, U. K. (2005), "Performance of long fiber reinforced thermoplastics subjected to transverse intermediate velocity blunt object impact", *Composite Structures,* vol. 67, no. 3, pp. 263-277.

[13] Dear, J. P., Lee, H. and Brown, S. A. (2005), "Impact damage processes in composite sheet and sandwich honeycomb materials", *International Journal of Impact Engineering,* vol. 32, no. 1–4, pp. 130-154.

[14] Santulli, C., Brooks, R., Long, A. C., Warrior, N. A. and Rudd, C. D. (2002), "Impact properties of compression moulded commingled E-glass–polypropylene composites", *Plastics, Rubber and Composites,* vol. 31, no. 6, pp. 270-277.

[15] Putnoki, I., Moos, E. and Karger-Kocsis, J. (1999), "Mechanical performance of stretched knitted fabric glass fibre reinforced poly(ethylene terephthalate) composites produced from commingled yarn", *Plastics, Rubber and Composites,* vol. 28, no. 1, pp. 40-46.

[16] Bigg, D. M. (1994), "The Impact Behavior of Thermoplastic Sheet Composites", *Journal of Reinforced Plastics and Composites,* vol. 13, no. 4, pp. 339-354.

[17] Cantwell, W. J. and Morton, J. (1991), "The impact resistance of composite materials — a review", *Composites,* vol. 22, no. 5, pp. 347-362.

[18] Naik, N. K. and Meduri, S. (2001), "Polymer-matrix composites subjected to low-velocity impact: effect of laminate configuration", *Composites Science and Technology,* vol. 61, no. 10, pp. 1429-1436.

[19] Alcock, B., Cabrera, N. O., Barkoula, N. M., Wang, Z. and Peijs, T. (2008), "The effect of temperature and strain rate on the impact performance of recyclable all-polypropylene composites", *Composites Part B: Engineering,* vol. 39, no. 3, pp. 537-547.

[20] Alcock, B., Cabrera, N. O., Barkoula, N. M. and Peijs, T. (2006), "Low velocity impact performance of recyclable all-polypropylene composites", *Composites Science and Technology,* vol. 66, no. 11–12, pp. 1724-1737.

[21] Xu, T. and Farris, R. J. (2007), "Comparative studies of ultra-high molecular weight polyethylene fiber reinforced composites", *Polymer Engineering & Science,* vol. 47, no. 10, pp. 1544-1553.

[22] Walsh, S. M., Scott, B. R., Spagnuolo, D. M. and ARMY RESEARCH LAB ABERDEEN PROVING GROUND MD. (2005)*, The Development of a Hybrid Thermoplastic Ballistic Material With Application to Helmets*.

[23] Reyes, G. and Sharma, U. (2010), "Modeling and damage repair of woven thermoplastic composites subjected to low velocity impact", *Composite Structures,* vol. 92, no. 2, pp. 523-531.

[24] Studer, F. (1983), "Automotive applications of stampable reinforced thermoplastics development prospects", *Materials & Design,* vol. 4, no. 4, pp. 804-808.

[25] Akay, M., O'Regan, D. F. and Bailey, R. S. (1995), "Fracture toughness and impact behaviour of glass-fibre-reinforced polyamide 6,6 injection mouldings", *Composites Science and Technology,* vol. 55, no. 2, pp. 109-118.

[26] Duan, Y., Saigal, A., Greif, R. and Zimmerman, M. A. (2003), "Impact behavior and modeling of engineering polymers", *Polymer Engineering & Science,* vol. 43, no. 1, pp. 112-124.

[27] Kohan, M. I., Barineau, J. M. and Rao, M. K. K. (1995), "Commercial Nylon Plastics and their Applications", in *Nylon Plastics Handbook,* 1st edition ed, Hanser, Munich, pp. 56.

[28] Platt, D. (ed.) (2003), *Engineering and High Performance Plastics,* Rapra Technology Limited.

[29] Aslan, Z., Karakuzu, R. and Okutan, B. (2003), "The response of laminated composite plates under low-velocity impact loading", *Composite Structures,* vol. 59, no. 1, pp. 119-127.

[30] Daiyan, H., Andreassen, E., Grytten, F., Lyngstad, O. V., Luksepp, T. and Osnes, H. (2010), "Low-velocity impact response of injection-moulded polypropylene plates – Part 1: Effects of plate thickness, impact velocity and temperature", *Polymer Testing,* vol. 29, no. 6, pp. 648-657.

[31] Hassan, A., Hassan, A. A. and Mohd Rafiq, M. I. (2011), "Impact properties of injection molded glass fiber/polyamide-6 composites: effect of testing parameters", *Journal of Reinforced Plastics and Composites,* vol. 30, no. 10, pp. 889-898.

[32] Leach, D. C. and Moore, D. R. (1985), "Failure and fracture of short glass fibre-reinforced nylon composites", *Composites,* vol. 16, no. 2, pp. 113-120.

[33] Belingardi, G. and Vadori, R. (2003), "Influence of the laminate thickness in low velocity impact behavior of composite material plate", *Composite Structures,* vol. 61, no. 1–2, pp. 27-38.

[34] EA R&D Avalon Field Test Cummins (2008), *Oil Pan Crack Failure*.

[35] Pacejka, H. B. (ed.) (2006), *Tyre and Vehicle Dynamics,* Elsevier/Butterworth-Heinemann, Amsterdam/London.

[36] Zhou, G. and Davies, G. A. O. (1995), "Impact response of thick glass fibre reinforced polyester laminates", *International Journal of Impact Engineering,* vol. 16, no. 3, pp. 357-374.

[37] Viana, J. C., Cunha, A. M. and Billon, N. (2007), "Experimental characterization and computational simulations of the impact behavior of

injection-molded polymers", *Polymer Engineering & Science,* vol. 47, no. 4, pp. 337-346.

[38] Galea, S. C. and Chiu, W. K. (1996), "The effect of multiple impact damage on the residual compressive strength of composite structures", *International Journal of Crashworthiness,* vol. 1, no. 3, pp. 305-313.

[39] Van Nuffel, D., De Baere, I., Van Paepegem, W. V. and Degrieck, J. (2010), "An experimental study on repetitive slamming wave impact on deformable composite structures", *Sampe Benelux Student Seminar 2010,* Ermelo, The Netherlands, Society for the Advancement of Material and Process Engineering (SAMPE), pp. 17.

[40] Mittelman, A., (1992), *Low-energy repetitive impact in carbon-epoxy composite*, Springer Netherlands.

[41] Eriksson, P., Boydell, P., Eriksson, K., Månson, J. -. E. and Albertsson, A. (1997), "Effect of thermal-oxidative aging on mechanical, chemical, and thermal properties of recycled polyamide 66", *Journal of Applied Polymer Science,* vol. 65, no. 8, pp. 1619-1630.

[42] Curtis, P. T., Bader, M. G. and Bailey, J. E. (1978), "The stiffness and strength of a polyamide thermoplastic reinforced with glass and carbon fibres", *Journal of Materials Science,* vol. 13, no. 2, pp. 377-390.

[43] Lhymn, C. and Schultz, J. M. (1987), "Strength and toughness of fibre-reinforced thermoplastics: effect of temperature and loading rate", *Composites,* vol. 18, no. 4, pp. 287-292.

[44] Valentin, D., Paray, F. and Guetta, B., (1987), *The hygrothermal behaviour of glass fibre reinforced PA66 composites: A study of the effect of water absorption on their mechanical properties*, Springer Netherlands.

[45] Starkweather, H. W. "The effect of water on some properties of oriented nylon", *Journal of Macromolecular Science, Part B,* , no. 4, pp. 727.

[46] Drake, N. (ed.) (1998), *Thermoplastics and Thermoplastic Composites in the Automotive Industry 1997-2000,* Rapra Technology Limited.

[47] Dhevi, D. M., Choi, C. W., Prabu, A. A. and Kim, K. J. (2009), "Deterioration in mechanical properties of glass fiber-reinforced nylon 6,6 composites by aqueous calcium chloride mixture solutions", *Polymer Composites,* vol. 30, no. 4, pp. 481-489.

[48] Cheremisinoff, N. P. (ed.) (1989), *Handbook of Polymer Science and Technology,* CRC Press.

[49] CAMPUS*, CAMPUSplastics*, available at: http://www.campusplastics.com/campus/.

[50] Sato, N., Kurauchi, T., Sato, S. and Kamigaito, O., (1984), *Mechanism of fracture of short glass fibre-reinforced polyamide thermoplastic*, Springer Netherlands.

[51] Sato, N., Kurauchi, T., Sato, S. and Kamigaito, O. (1998), "Reinforcing mechanism by small diameter fiber in short fiber composite ", *Journal of Composite Materials,* vol. 22, pp. 850-873.

[52] Horst, J. J. and Spoormaker, J. L. (1997), "Fatigue fracture mechanisms and fractography of short-glassfibre-reinforced polyamide 6", *Journal of Materials Science,* vol. 32, no. 14, pp. 3641-3651.

[53] Akay, M. and O'Regan, D. F. (1995), "Fracture behaviour of glass fibre reinforced polyamide mouldings", *Polymer Testing,* vol. 14, no. 2, pp. 149-162.

[54] Thomason, J. L. (1999), "The influence of fibre properties of the performance of glass-fibre-reinforced polyamide 6,6", *Composites Science and Technology,* vol. 59, no. 16, pp. 2315-2328.

[55] Hassan, A., Yahya, R., Yahaya, A. H., Tahir, A. R. M. and Hornsby, P. R. (2004), "Tensile, Impact and Fiber Length Properties of Injection-Molded Short and Long Glass Fiber-Reinforced Polyamide 6,6 Composites", *Journal of Reinforced Plastics and Composites,* vol. 23, no. 9, pp. 969-986.

[56] Bernasconi, A. and Cosmi, F. (2011), "Analysis of the dependence of the tensile behaviour of a short fibre reinforced polyamide upon fibre volume fraction, length and orientation", *Procedia Engineering,* vol. 10, no. 0, pp. 2129-2134.

[57] Thomason, J. L. (2007), "Structure-property relationships in glass reinforced polyamide, part 2: The effects of average fiber diameter and diameter distribution", *Polymer Composites,* vol. 28, no. 3, pp. 331-343.

[58] Ramsteiner, F. and Theysohn, R. (1985), "The influence of fibre diameter on the tensile behaviour of short-glass-fibre reinforced polymers", *Composites Science and Technology,* vol. 24, no. 3, pp. 231-240.

[59] Thomason, J. L. (2006), "Structure-property relationships in glass-reinforced polyamide, part 1: The effects of fiber content", *Polymer Composites,* vol. 27, no. 5, pp. 552-562.

[60] Thomason, J. L. (2008), "The influence of fibre length, diameter and concentration on the modulus of glass fibre reinforced polyamide 6,6", *Composites Part A: Applied Science and Manufacturing,* vol. 39, no. 11, pp. 1732-1738.

[61] Thomason, J. L. (2009), "The influence of fibre length, diameter and concentration on the impact performance of long glass-fibre reinforced polyamide 6,6", *Composites Part A: Applied Science and Manufacturing,* vol. 40, no. 2, pp. 114-124.

[62] Karger-Kocsis, J. and Friedrich, K. (1988), "Fracture behavior of injection-molded short and long glass fiber—polyamide 6.6 composites", *Composites Science and Technology,* vol. 32, no. 4, pp. 293-325.

[63] Schang, O., Billon, N. and Muracciole, J. M. (1996), "Mechanical behaviour of a ductile polyamide 12 during impact", *Polymer Engineering and Science,* vol. 36, no. 4, pp. 541-550.

[64] Mouhmid, B., Imad, A., Benseddiq, N., Benmedakhène, S. and Maazouz, A. (2006), "A study of the mechanical behaviour of a glass fibre reinforced polyamide 6,6: Experimental investigation", *Polymer Testing,* vol. 25, no. 4, pp. 544-552.

[65] Tancrez, J., Pabiot, J. and Rietsch, F. (1996), "Damage and fracture mechanisms in thermoplastic-matrix composites in relation to processing and structural parameters", *Composites Science and Technology,* vol. 56, no. 7, pp. 725-731.

[66] Güllü, A., Özdemir, A. and Özdemir, E. (2006), "Experimental investigation of the effect of glass fibres on the mechanical properties of polypropylene (PP) and polyamide 6 (PA6) plastics", *Materials & Design,* vol. 27, no. 4, pp. 316-323.

[67] Blumentritt, B. F., Vu, B. T. and Cooper, S. L. (1975), "Fracture in oriented short fibre-reinforced thermoplastics", *Composites,* vol. 6, no. 3, pp. 105-114.

[68] Bucknall, C. B. (1990), "Fracture resistance in rubber-toughened polymers", *Makromolekulare Chemie.Macromolecular Symposia,* vol. 38, no. 1, pp. 1-15.

[69] Çoban, O., Bora, M. Ö., Sinmazçelik, T., Cürgül, İ. and Günay, V. (2009), "Fracture morphology and deformation characteristics of repeatedly impacted thermoplastic matrix composites", *Materials & Design,* vol. 30, no. 3, pp. 628-634.

[70] Lauke, B. and Pompe, W. (1986), "Fracture toughness of short-fibre reinforced thermoplastics", *Composites Science and Technology,* vol. 26, no. 1, pp. 37-57.

[71] Thomason, J. L. and Vlug, M. A. (1997), "Influence of fibre length and concentration on the properties of glass fibre-reinforced polypropylene: 4. Impact properties", *Composites Part A: Applied Science and Manufacturing,* vol. 28, no. 3, pp. 277-288.

[72] Leaversuch, R. D. (2004), "Metal Replacement Accelerates In Under-Hood Parts", *Plastics Technology,* [Online], no. March 2004 available at: http://www.ptonline.com/articles/metal-replacement-accelerates-in-under-hood-parts.

[73] Leaversuch, R. D. (2003), "Strength and Beauty - New Nylons Bring Both To Under-Hood Parts", *Plastics Technology,* [Online], no. January 2003 available at: http://www.ptonline.com/articles/strength-and-beauty-new-nylons-bring-both-to-under-hood-parts.

[74] BASF SE (2011)*, Processing by injection molding*, available at: http://www.plasticsportal.net/wa/plasticsEU~en_GB/portal/show/common/content/products/engineering_plastics/ultramid/processing_by_injection_molding.

[75] Thomason, J. L. (2002), "The influence of fibre length and concentration on the properties of glass fibre-reinforced polypropylene: 5. Injection moulded long and short fifre PP'
", *Composites Part A: Applied Science and Manufacturing,* vol. 33, pp. 1641-1652.

[76] Gibson, A. G. and Payne, D. J. (1989), "Flexural and impact strength improvement in injection moulded SMC", *Composites,* vol. 20, no. 2, pp. 151-158.

[77] Russell, D. P. and Beaumont, P. W. R. (1980), "Structure and properties of injection-moulded nylon-6. Part 1. Structure and morphology of nylon-6'", *Journal of Materials Science,* vol. 15, no. 1, pp. 197-207.

[78] Russell, D. P. and Beaumont, P. W. R. (1980), "Structure and properties of injection-moulded nylon-6. Part 2. Residual stresses in injection-moulded nylon-6'", *Journal of Materials Science,* vol. 15, no. 1, pp. 208-215.

[79] Russell, D. P. and Beaumont, P. W. R. (1980), "Structure and properties of injection-moulded nylon-6. Part 3. Yield and fracture of injection-moulded nylon 6'", *Journal of Materials Science,* vol. 15, no. 1, pp. 216-221.

[80] Apichartpattanasiri, S., Hay, J. N. and Kukureka, S. N. (2001), "A study of the tribological behaviour of polyamide 66 with varying injection-moulding parameters", *Wear,* vol. 251, no. 1–12, pp. 1557-1566.

[81] Paterson, M. W. A. and White, J. R. (1992), "Effect of water absorption on residual stresses in injection-moulded nylon 6,6", *Journal of Materials Science,* vol. 27, no. 22, pp. 6229-6240.

[82] Paterson, M. W. A. and White, J. R. (1993), "Distortion of nylon 6,6 moldings caused by asymmetric water absorption", *Polymer Engineering & Science,* vol. 33, no. 22, pp. 1475-1482.

[83] De Monte, M., Moosbrugger, E. and Quaresimin, M. (2010), "Influence of temperature and thickness on the off-axis behaviour of short glass fibre reinforced polyamide 6.6 – cyclic loading", *Composites Part A: Applied Science and Manufacturing,* vol. 41, no. 10, pp. 1368-1379.

[84] Bartus, S. D. (2003), *Long-fiber-reinforced thermoplastic: process modeling and resistance to blunt object impact,* Materials Science and Engineering Department, University of Alabama at Birmingham.

[85] Lee, S., Cheon, J. and Im, Y. (1999), "Experimental and numerical study of the impact behavior of SMC plates", *Composite Structures,* vol. 47, no. 1–4, pp. 551-561.

[86] Sabre Ballistics (2008), *System Manual for Low Velocity Gas Gun,* 2776.

[87] Wu, S. (1985), "Phase structure and adhesion in polymer blends: A criterion for rubber toughening", *Polymer,* vol. 26, no. 12, pp. 1855-1863.

[88] Wu, S. (1988), "Generalized criterion for rubber toughening: The critical matrix ligament thickness.", *Journal of Applied Polymer Science,* vol. 35, no. 2, pp. 549-561.

[89] Laura, D. M., Keskkula, H., Barlow, J. W. and Paul, D. R. (2003), "Effect of rubber particle size and rubber type on the mechanical properties of glass fiber reinforced, rubber-toughened nylon 6", *Polymer,* vol. 44, no. 11, pp. 3347-3361.

[90] Pegoretti, A. and Ricco, T. (2006), "On the essential work of fracture of neat and rubber toughened polyamide-66", *Engineering Fracture Mechanics,* vol. 73, no. 16, pp. 2486-2502.

[91] Dermanaki Farahani, R. and Ramazani S.A., A. (2008), "Melt preparation and investigation of properties of toughened Polyamide 66 with SEBS-g-MA and their nanocomposites", *Materials & Design,* vol. 29, no. 1, pp. 105-111.

[92] Gaymans, R. J., Borggreve, R. J. M. and Oostenbrink, A. J. (1990), "Toughening behavior of polyamide-rubber blends", *Makromolekulare Chemie.Macromolecular Symposia,* vol. 38, no. 1, pp. 125-136.

[93] González-Montiel, A., Keskkula, H. and Paul, D. R. (1995), "Impact-modified nylon 6/polypropylene blends: 2. Effect of reactive functionality on morphology and mechanical properties", *Polymer,* vol. 36, no. 24, pp. 4605-4620.

[94] Wong, S. and Mai, Y. (1999), "Essential Fracture Work of Short Fiber Reinforced Polymer Blends", *Polymer Engineering and Science,* vol. 39, no. 2, pp. 356-364.

[95] Laura, D. M., Keskkula, H., Barlow, J. W. and Paul, D. R. (2000), "Effect of glass fiber and maleated ethylene–propylene rubber content on tensile and impact properties of Nylon 6", *Polymer,* vol. 41, no. 19, pp. 7165-7174.

[96] Huang, J. J., Keskkula, H. and Paul, D. R. (2004), "Rubber toughening of an amorphous polyamide by functionalized SEBS copolymers: morphology and Izod impact behavior", *Polymer,* vol. 45, no. 12, pp. 4203-4215.

[97] Akay, M. (1994), "Moisture absorption and its influence on the tensile properties of glass-fibre reinforced polyamide 6,6", *Polymers and Polymer Composites,* vol. 2, no. 6, pp. 349-354.

[98] Camino, G., Polishchuk, A. Y., Luda, M. P., Revellino, M., Blancon, R. and Martinez-Vega, J. J. (1998), "Water ageing of SMC composite materials: a tool for material characterisation", *Polymer Degradation and Stability,* vol. 61, no. 1, pp. 53-63.

[99] Bergeret, A., Pires, I., Foulc, M. P., Abadie, B., Ferry, L. and Crespy, A. (2001), "The hygrothermal behaviour of glass-fibre-reinforced thermoplastic composites: a prediction of the composite lifetime", *Polymer Testing,* vol. 20, no. 7, pp. 753-763.

[100] Steward, S. (1999), *The Effect of Salt Splash on Nylon 6,6* (Master of Science thesis), Virginia Polytechnic Institute and State University, Blacksburg.

[101] Pagilagan, R.U., (1995), *Degradation of nylons*, M.I. Kohan ed., Hanser/Gardner, New York.

[102] Kim, K. J., Dhevi, D. M., Lee, J. S., Cho, Y. D. and Choe, E. K. (2006), "Mechanism of glycolysis of nylon 6,6 and its model compound by ethylene glycol", *Polymer Degradation and Stability,* vol. 91, no. 7, pp. 1545-1555.

[103] Hong, J. H., Dhevi, D. M., Lee, J. S. and Kim, K. J. (2007), "Origin of deterioration in mechanical properties of glass fiber reinforced nylon 6,6 composites by aqueous ethylene glycol solution", *Polymer Composites,* vol. 28, no. 6, pp. 778-784.

[104] Hattori, M., Saito, M., Okajima, K. and Kamide, K. (1995), "Molecular characterization of nylon 6,6 and its dissolved state in mixture of calcium chloride and methanol", *Polymer Journal,* vol. 27, no. 6, pp. 631-644.

[105] Hattori, M. and Saito, M. (1996), "Thermal gelation of the nylon 6,6-calcium chloride-methanol system", *Polymer Journal,* vol. 28, pp. 139-144.

[106] Wyzgoski, M.G. and Novak, G.E., (1987), *Stress cracking of nylon polymers in aqueous salt solutions: Part 1 Stress-rupture behaviour* , Springer Netherlands.

[107] Wyzgoski, M.G. and Novak, G.E., (1987), *Stress cracking of nylon polymers in aqueous salt solutions: Part 2 Nylon-salt interactions* , Springer Netherlands.

[108] Wyzgoski, M.G. and Novak, G.E., (1987), *Stress cracking of nylon polymers in aqueous salt solutions: Part 3 Craze-growth kinetics* , Springer Netherlands.

[109] Xiong, Z., Li, X., Jia, Q., Fu, Z. and Yang, Z. (2010), "Complexation mechanism of polyamide 6/calcium chloride", *Acta Polymerica Sinica,* no. 8, pp. 1003-1008.

[110] Chevali, V. S., Dean, D. R. and Janowski, G. M. (2010), "Effect of environmental weathering on flexural creep behavior of long fiber-reinforced thermoplastic composites", *Polymer Degradation and Stability,* vol. 95, no. 12, pp. 2628-2640.

[111] Rudzinski, S., Häussler, L., Harnisch, C., Mäder, E. and Heinrich, G. (2011), "Glass fibre reinforced polyamide composites: Thermal behaviour of sizings", *Composites Part A: Applied Science and Manufacturing,* vol. 42, no. 2, pp. 157-164.

[112] Sonsino, C. M. and Moosbrugger, E. (2008), "Fatigue design of highly loaded short-glass-fibre reinforced polyamide parts in engine compartments", *International Journal of Fatigue,* vol. 30, no. 7, pp. 1279-1288.

[113] Vincent, M., Giroud, T., Clarke, A. and Eberhardt, C. (2005), "Description and modeling of fiber orientation in injection molding of fiber reinforced thermoplastics", *Polymer,* vol. 46, no. 17, pp. 6719-6725.

[114] Verleye, V., Couniot, A. and Dupret, F. (1994), "Numerical prediction of fiber orientation in complex composite injection-molded parts", *American Society of Mechanical Engineers, Materials Division (Publication) MD,* Vol. 49, pp. 265.

[115] Dray, D., Gilormini, P. and Régnier, G. (2007), "Comparison of several closure approximations for evaluating the thermoelastic properties of an injection molded short-fiber composite", *Composites Science and Technology,* vol. 67, no. 7–8, pp. 1601-1610.

[116] Vincent, M., Devilers, E. and Agassant, J. (1997), "Fibre orientation calculation in injection moulding of reinforced thermoplastics", *Journal of Non-Newtonian Fluid Mechanics,* vol. 73, no. 3, pp. 317-326.

[117] Doghri, I. and Friebel, C. (2005), "Effective elasto-plastic properties of inclusion-reinforced composites. Study of shape, orientation and cyclic response", *Mechanics of Materials,* vol. 37, no. 1, pp. 45-68.

[118] Doghri, I. and Tinel, L. (2005), "Micromechanical modeling and computation of elasto-plastic materials reinforced with distributed-orientation fibers", *International Journal of Plasticity,* vol. 21, no. 10, pp. 1919-1940.

[119] Mlekusch, B. (1999), "Thermoelastic properties of short-fibre-reinforced thermoplastics", *Composites Science and Technology,* vol. 59, no. 6, pp. 911-923.

[120] Pierard, O. and Doghri, I. (2006), "An enhanced affine formulation and the corresponding numerical algorithms for the mean-field homogenization of elasto-viscoplastic composites", *International Journal of Plasticity,* vol. 22, no. 1, pp. 131-157.

[121] Meraghni, F., Desrumaux, F. and Benzeggagh, M. L. (2002), "Implementation of a constitutive micromechanical model for damage analysis in glass mat reinforced composite structures", *Composites Science and Technology,* vol. 62, no. 16, pp. 2087-2097.

[122] Zaïri, F., Naït-Abdelaziz, M., Gloaguen, J. M., Bouaziz, A. and Lefebvre, J. M. (2008), "Micromechanical modelling and simulation of chopped random fiber reinforced polymer composites with progressive debonding damage", *International Journal of Solids and Structures,* vol. 45, no. 20, pp. 5220-5236.

[123] Launay, A., Marco, Y., Maitournam, M. H., Raoult, I. and Szmytka, F. (2010), "Cyclic behavior of short glass fiber reinforced polyamide for fatigue life prediction of automotive components", *Procedia Engineering,* vol. 2, no. 1, pp. 901-910.

[124] Regrain, C., Laiarinandrasana, L., Toillon, S. and Saï, K. (2009), "Multi-mechanism models for semi-crystalline polymer: Constitutive relations and finite element implementation", *International Journal of Plasticity,* vol. 25, no. 7, pp. 1253-1279.

[125] Zhou, Y. and Mallick, P. K. (2005), "A non-linear damage model for the tensile behavior of an injection molded short E-glass fiber reinforced polyamide-6,6", *Materials Science and Engineering: A,* vol. 393, no. 1-2, pp. 303-309.

[126] Lobo, H. and Hurtado, J. "Characterization and Modeling of Nonlinear Behavior of Plastics", 2006, Boston.

[127] Lobo, H. "Methodology for Selection of Material Models for Plastics Impact Simulation", 2006, Detroit.

[128] Ibrahim, R. A. and Pettit, C. L. (2005), "Uncertainties and dynamic problems of bolted joints and other fasteners", *Journal of Sound and Vibration,* vol. 279, no. 3–5, pp. 857-936.

[129] Chadegani, A. and Batra, R. C. (2011), "Analysis of adhesive-bonded single-lap joint with an interfacial crack and a void", *International Journal of Adhesion and Adhesives,* vol. 31, no. 6, pp. 455-465.

[130] Chen, G.L., (2011), *Study the application of laser welding in the automotive transmission parts*.

[131] Anon (1995), "Vibration welding of moulded parts and semi-finished parts of thermoplastic polymers in mass production", *Welding in the World, Le Soudage Dans Le Monde,* vol. 35, no. 2, pp. 138-146.

[132] Plastics Design Library (ed.) (1997), *Handbook of Plastics Joining: A Practical Guide,* Plastics Design Library.

[133] Branson Ultrasonics (2001), "Automotive parts benefit from vibration welding", *Reinforced Plastics,* vol. 45, no. 2, pp. 46-50.

[134] Gowri, S., Hariharan, P. and Suresh Babu, A. (eds.) (2008), *Manufacturing Technology-I,* Dorling Kindersley.

[135] Hatcher, W. J. (1983), "Vibration welding of automotive thermoplastic box beam bumpers", *National Technical Conference - Society of Plastics Engineers,* pp. 133.

[136] Patham, B. and Foss, P. H. (2011), "Thermoplastic vibration welding: Review of process phenomenology and processing-structure-property interrelationships", *Polymer Engineering and Science,* vol. 51, no. 1, pp. 1-22.

[137] M-Base*, Material Data Center*, available at: http://www.materialdatacenter.com/mb/main.

[138] BASF SE, (2009), *Target Ultramid grade comparison for hot oil applications*.

[139] Chapman, R. D. and Chruma, J. L. (eds.) (1985), *Engineering Thermoplastics, Properties and Applications,* Margolis J.M. ed, Marcel Dekker, New York.

[140] Titow, W. V. and Lanham, B. J. (eds.) (1975), *Reinforced Thermoplastics,* Applied Science ed, Elsevier Science Ltd, London.

[141] Darden, E. T. (ed.) (1973), *Nylon Plastics,* Kohan, M. I. ed, John Wiley and Sons, New York.

[142] Shiao, M., Nair, S. V., Garrett, P. D. and Pollard, R. E. (1994), "Deformation mechanism and fibre toughening of nylon 6,6", *Polymer,* vol. 35, no. 2, pp. 306-314.

[143] Bonner, R. M., Kohan, M. I., Lacey, E. M., Richardson, P. N., Roder, T. M. and Sherwood Jr, L. T. (eds.) (1973), *Nylon Plastics,* Kohan, M.I. ed, John Whiley and Sons, New York.

[144] McCrum, N. G., Buckley, C. P. and Bucknall, C. B. (eds.) (1997), *Principles of polymer engineering,* 2nd Revised edition ed, Oxford University Press, Oxford.

[145] Bader, M. G. and Bowyer, W. H. (1972), "The mechanical properties of thermoplastics strengthened by short discontinuous fibres", *Journal of Physics D: Applied Physics,* vol. 5, no. 12, pp. 2215-2225.

[146] Hashemi, S. and Mugan, J. (1993), "Fracture mechanics of short glass fibre-reinforced nylon composite", *Journal of Materials Science,* vol. 28, no. 15, pp. 3983-3990.

[147] Shiao, M. L., Nair, S. V., Garrett, P. D. and Pollard, R. E. (1994), "Effect of glass-fibre reinforcement and annealing on microstructure and mechanical behaviour of nylon 6,6 - Part II Mechanical behaviour", *Journal of Materials Science,* vol. 29, no. 7, pp. 1739-1752.

[148] Gomina, M., Pinot, L., Moreau, R. and Nakache, E. (2003), "Fracture behaviour of short glass fibre-reinforced rubber-toughened nylon composites", in *European Structural Integrity Society,* Elsevier, , pp. 399-418.

[149] Bucknall, C. B., Heather, P. and Lazzeri, A. (1989), "Rubber toughening of plastics", *Journal of Materials Science,* vol. 24, no. 6, pp. 2255-2261.

[150] Borggreve, R. J. M., Gaymans, R. J. and Eichenwald, H. M. (1989), "Impact behaviour of nylon-rubber blends: 6. Influence of structure on voiding processes; toughening mechanism", *Polymer,* vol. 30, no. 1, pp. 78-83.

[151] Borggreve, R. J. M., Gaymans, R. J., Schuijer, J. and Housz, J. F. I. (1987), "Brittle-tough transition in nylon-rubber blends: effect of rubber concentration and particle size", *Polymer,* vol. 28, no. 9, pp. 1489-1496.

[152] Huang, D. D. and Williams, J. G. (1987), "Testing of toughened nylons", *Journal of Materials Science,* vol. 22, no. 7, pp. 2503-2508.

[153] Cimmino, S., D'Orazio, L., Greco, R., Maglio, G., Malinconico, M., Mancarella, C., Martuscelli, E., Palumbo, R. and Ragosta, G. (1984), "Morphology - Properties Relationships in Binary Polyamide 6/Rubber Blends: Influence of the Addition of a Functionalized Rubber", *Polymer Engineering and Science,* vol. 24, no. 1, pp. 48-56.

[154] Oostenbrink, A. J. and Gaymans, R. J. (1992), "Maleic anhydride grafting on EPDM rubber in the melt", *Polymer,* vol. 33, no. 14, pp. 3086-3088.

[155] Ghidoni, D., Fasulo, G. C., Cecchele, D., Merlotti, M., Sterzi, G. and Nocci, R. (1993), "A study on compatibilization of AES/PA6 blends", *Journal of Materials Science,* vol. 28, no. 15, pp. 4119-4128.

[156] Sui, G., Wong, S. and Yue, C. (2001), "Effect of extrusion compounding on the mechanical properties of rubber-toughened polymers containing short glass fibers", *Journal of Materials Processing Technology,* vol. 113, no. 1-3, pp. 167-171.

[157] Oshinski, A. J., Keskkula, H. and Paul, D. R. (1996), "The role of matrix molecular weight in rubber toughened nylon 6 blends: 1. Morphology", *Polymer,* vol. 37, no. 22, pp. 4891-4907.

[158] Oshinski, A. J., Keskkula, H. and Paul, D. R. (1996), "The role of matrix molecular weight in rubber toughened nylon 6 blends: 3. Ductile-brittle transition temperature", *Polymer,* vol. 37, no. 22, pp. 4919-4928.

[159] Laura, D. M., Keskkula, H., Barlow, J. W. and Paul, D. R. (2001), "Effect of glass fiber and maleated ethylene–propylene rubber content on the impact fracture parameters of nylon 6", *Polymer,* vol. 42, no. 14, pp. 6161-6172.

[160] Ahn, Y. and Paul, D. R. (2006), "Rubber toughening of nylon 6 nanocomposites", *Polymer,* vol. 47, no. 8, pp. 2830-2838.

[161] González-Montiel, A., Keskkula, H. and Paul, D. R. (1995), "Impact-modified nylon 6/polypropylene blends: 1. Morphology-property relationships", *Polymer,* vol. 36, no. 24, pp. 4587-4603.

[162] González-Montiel, A., Keskkula, H. and Paul, D. R. (1995), "Impact-modified nylon 6/polypropylene blends: 3. Deformation mechanisms", *Polymer,* vol. 36, no. 24, pp. 4621-4637.

[163] Wong, S. C. and Mai, Y. W. (1999), "Effect of rubber functionality on microstructures and fracture toughness of impact-modified nylon 6,6/polypropylene blends: 1. Structure–property relationships", *Polymer,* vol. 40, no. 6, pp. 1553-1566.

[164] Willis, J. M. and Favis, B. D. (1988), "Processing-morphology relationships of compatibilized polyolefin/polyamide blends. Part I: The effect of an Ionomer compatibilizer on blend morphology", *Polymer Engineering & Science,* vol. 28, no. 21, pp. 1416-1426.

[165] Wu, S. (1983), "Impact fracture mechanisms in polymer blends: Rubber-toughened nylon", *Journal of Polymer Science: Polymer Physics Edition,* vol. 21, no. 5, pp. 699-716.

[166] Bala, S. (2001), *Contact Modeling in LS-DYNA*, available at: http://www.dynasupport.com/tutorial/ls-dyna-users-guide/contact-modeling-in-ls-dyna.

[167] Abrate, S. (2001), "Modeling of impacts on composite structures", *Composite Structures,* vol. 51, no. 2, pp. 129-138.

[168] Avery, J. (ed.) (1998), *Injection Moulding Alternatives: a Guide for Designers and Product Engineers,* Hanser/Gardner Publications.

[169] Sun, B. (1994), "Study on the Mechanism of Nylon 6,6 Dissolving Process Using $CaCl_2$/MeOH as the Solvent", *Chinese Journal of Polymer Science,* vol. 12, no. 1, pp. 57.

[170] Wei, W., Qiu, L., Wang, X., Chen, H., Lai, Y., Tsai, F., Zhu, P. and Yeh, J., (2011), *Drawing and tensile properties of polyamide 6/calcium chloride composite fibers*, Springer Netherlands.

[171] Cheng, X., He, Q. J. and Zhang, A. M. (2004), "Time-resolved FTIR study of amorphous process of nylon 6 with calcium chloride.", *Guangpuxue Yu Guangpu Fenxi,* vol. 24, no. 3, pp. 295.

[172] Pazur, A. S. (1981), "PVC corrugated drainage pipe", *Journal of Vinyl Technology,* vol. 3, no. 4, pp. 219-221.

[173] Shelley, T. (2009), "New shape helps to resist pressure", *Eureka Magazine,* [Online], available at: http://www.eurekamagazine.co.uk/article/21056/New-shape-helps-to-resist-pressure.aspx.

[174] Moser, A. P. (ed.) (2001), *Buried Pipe Design,* 2nd ed. ed, McGraw-Hill, New York.

[175] Hurd, J. O. and Sargand, S. (1988), "Field performance of corrugated metal box culverts", in *Culverts and Tiebacks,* no. 1191, Transportation Research Board, Washington DC, pp. 39-45.

[176] Duncan, J. M., Seed, R. B. and Drawsky, R. H. (1985), "Design of corrugated metal box culverts", in *Analysis of Soil-Culvert Interaction and Design,* 1008th ed, Transport Research Board, Washington DC, pp. 33-41.

[177] Sokol, Z., Wald, F. and Kallerová, P. (2008), "Design of corrugated sheets exposed to fire", *Steel & Composite Structures,* vol. 8, no. 3.

[178] Sek, M. A. and Rouillard, V. (2006), "Behaviour of Multi-Layered Corrugated Paperboard Cushioning Sytems under Impact Loads", *Applied Mechanics and Materials,* vol. 3-4, pp. 383-390.

[179] Chonhenchob, V. and Singh, S. P. (2003), "A comparison of corrugated boxes and reusable plastic containers for mango distribution", *Packaging Technology and Science,* vol. 16, no. 6, pp. 231-237.

[180] Urbanik, T. J. (1996), "Machine Direction Strength Theory of Corrugated Fiberboard", *Journal of Composites Technology & Research,* vol. 18, no. 2, pp. 80-88.

[181] Johnson, M. W. J. and Urbanik, T. J. (1989), "Analysis of the localized buckling in composite plate structures with application to determine the strength of corrugated fiberboard", *Journal of Composites Technology & Research,* vol. 11, no. 4, pp. 121-127.

[182] Marzbanrad, J., Alijanpour, M. and Kiasat, M. S. (2009), "Design and analysis of an automotive bumper beam in low-speed frontal crashes", *Thin-Walled Structures,* vol. 47, no. 8–9, pp. 902-911.

[183] Billon, N. and Haudin, M. (1992), "Numerical methods in industrial forming processes", *4th International Conference on Numerical Methods in Industrial Forming Processes,* 1992, Sophia-Antipolis, NUMIFORM'92, pp. 335.

[184] Singh, R., Mattoo, A. and Saigal, A. (2006), "Optimizing the design and impact behavior of a polymeric enclosure", *Materials & Design,* vol. 27, no. 10, pp. 955-967.

[185] Brilmyer, G. H. (1999), "Impact of separator design on battery performance in traction applications", *Journal of Power Sources,* vol. 78, no. 1–2, pp. 68-72.

[186] Nimmer, R. P. (1983), "Analysis of the puncture of a bisphenol-a polycarbonate disc", *Polymer Engineering & Science,* vol. 23, no. 3, pp. 155-164.

[187] Hohenstein, T. *Impact simulation on aged plastic: 5,000 hours in hot oil and then struck by stones,* , BASF Plastics, Ludwigshafen.

[188] Nguyen, S. N., Greenhalgh, E. S., Olsson, R., Lannucci, L. and Curtis, P. T. (2010), "Parametric analysis of runway stone lofting mechanisms", *International Journal of Impact Engineering,* vol. 37, no. 5, pp. 502-514.

[189] Nguyen, S. N., Greenhalgh, E. S., Olsson, R., Lannucci, L. and Curtis, P. T. (2008), "Modeling the Lofting of Runway Debris by Aircraft Tires", *Journal of AIircraft,* vol. 45, no. 5, pp. 1701-1714.

[190] Nguyen, S. N., Greenhalgh, E. S., Lannucci, L., Longstaff, S., Olsson, R. and Curtis, P. T. (2011), "Experimental Characterisation of Tyre Indentation by Simulated Runway Debris", *Strain,* vol. 47, no. 4, pp. 343-350.

[191] Longstaff, S. (2008), *Experimental characterisation of the interaction between tyres and stones* (Final Year Project (M.E.) thesis), Department of Aeronautics, Imperial College, London.

[192] Mines, R. A. W., McKown, S. and Birch, R. S. (2007), "Impact of aircraft rubber tyre fragments on aluminium alloy plates: I – Experimental", *International Journal of Impact Engineering,* , no. 34, pp. 627–646.

[193] Ramamurthy, A. C., Lorenzen, W. I. and Bless, S. J. (1994), "Stone impact damage to automotive paint finishes: An introduction to impact physics and impact induced corrosion", *Progress in Organic Coatings,* vol. 25, no. 1, pp. 43-71.

[194] Mouti, Z., Westwood, K., Kayvantash, K. and Njuguna, J. (2010), "Low Velocity Impact Behavior of Glass Filled Fiber-Reinforced Thermoplastic Engine Components", *Materials,* vol. 3, no. 4, pp. 2463-2473.

[195] Mouti, Z., Westwood, K., Long, D. and Njuguna, J. (2011), "Finite element analysis of localised impact loading on short glass fibre-reinforced polyamide engine oil pan subjected to low velocity impact from flying projectiles", *8th European LS-DYNA Users Conference,* May 2011, Strasbourg, .

[196] Hasenauer, J., Küper, D., Laumeyer, J. E. and Welsh, I. *Top Ten Design Tips - A Series of 10 Articles*.

Appendices

Appendix 1: PA66-GF35 material data sheet

Product Information

Sep 2012

Ultramid® A3HG7
Polyamide 66

BASF
The Chemical Company

Product Description

Ultramid A3HG7 is a 35% glass fiber reinforced injection molding PA66 grade.

Applications

Typical applications include machinery components and housings of high stiffness and dimensional stability such as gears, solenoid valve housings, electrical flow heaters, trailing cable attachments, as well as electrically insulating parts.

PHYSICAL	ISO Test Method	Property Value	
Density, g/cm	1183	1.41	
Moisture, %	62		
(50% RH)		1.6	
(Saturation)		5	
RHEOLOGICAL	**ISO Test Method**	**Dry**	**Conditioned**
Melt Volume Rate (275 C/- Kg), cc/10min.	1133	40	-
MECHANICAL	**ISO Test Method**	**Dry**	**Conditioned**
Tensile Modulus, MPa	527		
23C		11,500	8,500
Tensile stress at break, MPa	527		
23C		210	150
Tensile strain at break, %	527		
23C		3	5
Flexural Modulus, MPa	178		
23C		10,000	-
IMPACT	**ISO Test Method**	**Dry**	**Conditioned**
Charpy Notched, kJ/m²	179		
23C		13	22
-30C		12	-
Charpy Unnotched, kJ/m²	179		
23C		95	105
-30C		75	-
THERMAL	**ISO Test Method**	**Dry**	**Conditioned**
Melting Point, C	3146	260	-
HDT A, C	75	250	-
HDT B, C	75	250	-
Coef. of Linear Thermal Expansion, Parallel, mm/mm C		0.17 X10-4	-
Coef. of Linear Thermal Expansion, Normal, mm/mm C		0.65 X10-4	-
ELECTRICAL	**ISO Test Method**	**Dry**	**Conditioned**
Comparative Tracking Index	IEC 60112	550	550
Volume Resistivity	IEC 60093	1E15	1E10
Dielectric Constant (1 MHz)	IEC 60250	3.5	5.7

BASF Corporation
Engineering Plastics
1609 Biddle Avenue
Wyandotte, MI 48192

General Information: 800-BC-RESIN
Technical Assistance: 800-527-TECH (734-324-5150)
Web address: http://www.plasticsportal.com/usa

Page 1 of 2

Dissipation Factor (100 Hz)	IEC 60250	200	3,000
Dissipation Factor (1 MHz)	IEC 60250	200	1,500

UL RATINGS	UL Test Method	Property Value
Flammability Rating, 1.5mm	UL94	HB
Relative Temperature Index, 1.5mm	UL746B	
Mechanical w/o Impact, C		130
Mechanical w/ Impact, C		120
Electrical, C		120

Processing Guidelines

Material Handling
Max. Water content: 0.12%
Product is supplied in sealed containers and drying prior to molding is not required. If drying becomes necessary, a dehumidifying or desiccant dryer operating at 80 degC (176 degF) is recommended. Drying time is dependent on moisture level, but 2-4 hours is generally sufficient. Further information concerning safe handling procedures can be obtained from the Material Safety Data Sheet. Alternatively, please contact your BASF representative.

Typical Profile
Melt Temperature 280-305 degC (535-580 degF)
Mold Temperature 80-90 degC (176-194 degF)
Injection and Packing Pressure 35-125 bar (500-1500 psi)

Mold Temperatures
A mold temperature of 80-90 degC (176-194 degF) is recommended, but temperatures of as low as 45 degC (113 degF) and as high as 105 degC (221 degF) can be used where applicable.

Pressures
Injection pressure controls the filling of the part and should be applied for 90% of ram travel. Packing pressure affects the final part and can be used effectively in controlling sink marks and shrinkage. It should be applied and maintained until the gate area is completely frozen off.

Back pressure can be utilized to provide uniform melt consistency and reduce trapped air and gas. Minimal back pressure should be utilized to prevent glass breakage.

Fill Rate
Fast fill rates are recommended to ensure uniform melt delivery to the cavity and prevent premature freezing. Surface appearance is directly affected by injection rate.

Note

BASF Corporation
Engineering Plastics
1609 Biddle Avenue
Wyandotte, MI 48192

General Information: 800-BC-RESIN
Technical Assistance: 800-527-TECH (734-324-5150)
Web address: http://www.plasticsportal.com/usa

Appendix 2: PA66-i-GF35 material data sheet

Product Information

Sep 2012

Ultramid® A3WG7 BK23210

Polyamide 66

BASF The Chemical Company

Product Description

Ultramid A3WG7 BK23210 is a 35% glass fiber reinforced, pigmented black and heat resistance injection molding PA66 grade for machinery for industrial items.

Applications

Typical applications include gear wheels, solenoid valve housings, cable attachments, automotive fuel distributors and components for automotive gear shift.

PHYSICAL	ISO Test Method	Property Value	
Density, g/cm	1183	1.41	
Moisture, %	62		
(50% RH)		1.6	
(Saturation)		5	
MECHANICAL	**ISO Test Method**	**Dry**	**Conditioned**
Tensile stress at break, MPa	527		
23C		190	-
Tensile strain at break, %	527		
23C		2.5	-
Flexural Modulus, MPa	178		
23C		9,600	-
IMPACT	**ISO Test Method**	**Dry**	**Conditioned**
Izod Notched Impact, kJ/m^2	180		
23C		10	-
THERMAL	**ISO Test Method**	**Dry**	**Conditioned**
Melting Point, C	3146	260	-
HDT A, C	75	250	-

Processing Guidelines

Material Handling
Max. Water content: 0.12%
Product is supplied in sealed containers and drying prior to molding is not required. If drying becomes necessary, a dehumidifying or desiccant dryer operating at 80 degC (176 degF) is recommended. Drying time is dependent on moisture level, but 2-4 hours is generally sufficient. Further information concerning safe handling procedures can be obtained from the Material Safety Data Sheet. Alternatively, please contact your BASF representative.

Typical Profile
Melt Temperature 280-305 degC (535-580 degF)
Mold Temperature 80-90 degC (176-194 degF)
Injection and Packing Pressure 35-125 bar (500-1500 psi)

Mold Temperatures
A mold temperature of 80-90 degC (176-194 degF) is recommended, but temperatures of as low as 45 degC (113 degF) and as high as 105 degC (221 degF) can be used where applicable.

Pressures
Injection pressure controls the filling of the part and should be applied for 90% of ram travel. Packing pressure affects the final part and can be used effectively in controlling sink marks and shrinkage. It should be applied and maintained until the gate area is completely frozen off.

BASF Corporation
Engineering Plastics
1609 Biddle Avenue
Wyandotte, MI 48192

General Information: 800-BC-RESIN
Technical Assistance: 800-527-TECH (734-324-5150)
Web address: http://www.plasticsportal.com/usa

Back pressure can be utilized to provide uniform melt consistency and reduce trapped air and gas. Minimal back pressure should be utilized to prevent glass breakage.

Fill Rate
Fast fill rates are recommended to ensure uniform melt delivery to the cavity and prevent premature freezing. Surface appearance is directly affected by injection rate.

Note

Appendix 3: PA6-i-GF35 material data sheet

Product Information
Sep 2012

Ultramid® B3ZG8 BK20560
Polyamide 6

BASF
The Chemical Company

Product Description

Ultramid B3ZG8 BK20560 is an impact-modified, pigmented black and 40% glass fiber reinforced injection molding PA6 grade having very high impact strength and rigidity.

Applications

Typical applications include airbag housings and half-shells for suitcases.

PHYSICAL	ISO Test Method	Property Value	
Density, g/cm	1183	1.42	
Moisture, %	62		
(50% RH)		1.6	
(Saturation)		5	
RHEOLOGICAL	**ISO Test Method**	**Dry**	**Conditioned**
Melt Volume Rate (235 C/5 Kg), cc/10min.	1133	4	-
MECHANICAL	**ISO Test Method**	**Dry**	**Conditioned**
Tensile Modulus, MPa	527		
23C		11,600	6,700
Tensile stress at break, MPa	527		
23C		160	115
Tensile strain at break, %	527		
23C		4	9
Flexural Modulus, MPa	178		
23C		9,500	6,100
IMPACT	**ISO Test Method**	**Dry**	**Conditioned**
Izod Notched Impact, kJ/m²	180		
23C		22	-
THERMAL	**ISO Test Method**	**Dry**	**Conditioned**
Melting Point, C	3146	220	-
HDT A, C	75	205	-
HDT B, C	75	220	-

Processing Guidelines

Material Handling
Max. Water content: 0.08%
Product is supplied in sealed containers and drying prior to molding is not required. If drying becomes necessary, a dehumidifying or desiccant dryer operating at 80 degC (176 degF) is recommended. Drying time is dependent on moisture level but 2-4 hours is generally sufficient. Further information concerning safe handling procedures can be obtained from the Material Safety Data Sheet. Alternatively, please contact your BASF representative.

Typical Profile
Melt Temperature 270-295 degC (518-563 degF)
Mold Temperature 80-95 degC (176-203 degF)
Injection and Packing Pressure 35-125 bar (500-1800psi)
Rear Zone 245-275 degC (473-527 degF)
Center Zone 260-285 degC (500-545 degC)
Front Zone 270-295 degC (518-563 degF)

BASF Corporation
Engineering Plastics
1609 Biddle Avenue
Wyandotte, MI 48192

General Information: 800-BC-RESIN
Technical Assistance: 800-527-TECH (734-324-5150)
Web address: http://www.plasticsportal.com/usa

Nozzle 270-295 degC (518-563 degF)

Mold Temperatures

This product can be processed over a wide range of mold temperatures; however, for applications where aesthetics are critical, a mold surface temperature of 80-95 degC (176-203 degF) is required.

Pressures

Injection pressure controls the filling of the part and should be applied for 90% of ram travel. Packing pressure affects the final part and can be used effectively in controlling sink marks and shrinkage. It should be applied and maintained until the gate area is completely frozen off.

Back pressure can be utilized to provide uniform melt consistency and reduce trapped air and gas. Minimal back pressure should be utilized to prevent glass breakage.

Fill Rate

Fast fill rates are recommended to ensure uniform melt delivery to the cavity and prevent premature freezing. Surface appearance is directly affected by injection rate.

Note

BASF Corporation
Engineering Plastics
1609 Biddle Avenue
Wyandotte, MI 48192

General Information: 800-BC-RESIN
Technical Assistance: 800-527-TECH (734-324-5150)
Web address: http://www.plasticsportal.com/usa

Appendix 4: Guidance for impact simulation on plastic part using LS-DYNA with stress-strain relations

Introduction

This report gives some general guidance on how to represent, analyse and interpret localised low-velocity impact using finite element method to predict performance and damage of reinforced plastic structure. The application is the assessment of localised impact on short glass reinforced polyamide oil pan structure.

Thermoplastic polymers and thus, polyamides, are complex materials to describe. Their behaviours are rate-dependent therefore their mechanical properties diverge with changing environment. Thermoplastics perform in a non-linear way that is not easily accessible by conventional material models with roots in metals theory. They do not exhibit ideally elastic behaviour. The plastic strain begins prior to yield and the elastic behaviour is non-linear. Another problem arises with the reinforcement with short glass fibres filling the matrix, those considerations complicate evens more the description of their mechanical behaviours. In addition to increasing stiffness, fibres also change the way plastics fail and often from ductile to brittle. The material is anisotropic due to short glass fibres. There is a particular dependency in the direction of the fibres since they are strongly oriented by the flow during the injection moulding process. Nonetheless,

despite fully dedicated material laws, it is possible to conduct meaningful analyses with limited data input.

The simulations described in this document are based on stress-strain relations at fixed conditions to describe a very specific situation at each time. The failure is considered and is flagged by the maximum strain leading to failure. The finite element analyses are carried out with LS-PrePost as a pre and post-processor and LS-DYNA as the solver.

Pre-Processing

System of units

LS-DYNA is dimensionless computational solver and therefore the end user is free to use any mechanical system of homogeneous units (examples given at Table 29). It is important to be consistent with the system of units chosen as the output parameters will be given according to the system employed.

Table 29 - System of units

Example	Length	Time	Mass	Force	Pressure	Velocity	Density	Energy
1	mm	s	t	N	MPa	mm/s	t/mm^3	mJ
2	mm	ms	g	N	MPa	mm/s	g/mm^3	mJ

Part section and Meshing

The representation of the part section can be in two or three dimension and it depends on the application needs and time resource. In the case of a large part with complex geometries, the time necessary for calculation on a 3D quad model can rapidly be excessively important. As a result, its representation in a mid-surface 2D shell thickness model is sensible and practical. The quality of the meshing has also an important role on the accuracy of the simulated model. The partition of an interval depends on the type of simulation realised. The mesh does not need to be dense if the represented impact is a macro-scale crash. In the case of a localised impact, only the impacted area does really need to have a refine mesh. Beyond that area, it is not essential to have a dense mesh. It increases unnecessarily the calculation time. A possible solution is to implement a dynamic adaptive mesh refinement that will track the feature of the result as the computation progresses (CONTROL_ADAPTIVE). In the case of the impactor or projectile, the meshing density should not be too different from the meshing of the impacted surface. One way to assess the quality of the mesh is by plotting the hourglass energy of the model (CONTROL_ENERGY). If the hourglass is not negligible, the mesh density is to be revised. If the quality of the mesh is good but the hourglass energy is still important, the solution is to control that energy (CONTROL_HOURGLASS).

Material and failure criteria

The material model is based on elasto-plastic material law using stress-strain relations. The elastic Young's modulus defines the stress-strain relation up to the yield stress. Above yield stress, there are several options. The plastic behaviour can be described by the plastic modulus which defines a linear relation between the stress and effective plastic strain. This relation can also be a curve, defined by a range of stress-strain coordinates (LCSS: Loaded Curve Stress Strain). Finally, the relation can also be dependent on the strain rate (LCSR: Loaded Curve Strain Rate) in which several stress-strain curves are defined together with a parameter setting the velocity for which each curve is representative. The stress for a certain effective strain value is determined as a linear interpolation from these curves.

The stress-strain relations depend on the type of loading considered. If the aim is to model a simple tensile test, the tensile stress-strain relation should be used. If the test considered is a localised impact, the tensile stress-strain is not recommended. Instead, a dynamic flexion test is more appropriate for given the right stress-strain relation.

Example of how to use stress-strain relation in a material card (MAT 24):

Initially, one should make sure that the experimental data used is expressed in terms of true stress (σ_{true}) versus true strain (ε_{true}) and not

engineering stress versus engineering strain. If not, the conversion has to be done as follows (see differences in Figure 73):

$$\sigma_{true} = \sigma_{\text{engineering}} * (1 + \varepsilon_{\text{engineering}})$$

$$\varepsilon_{true} = \ln(1 + \varepsilon_{engineering})$$

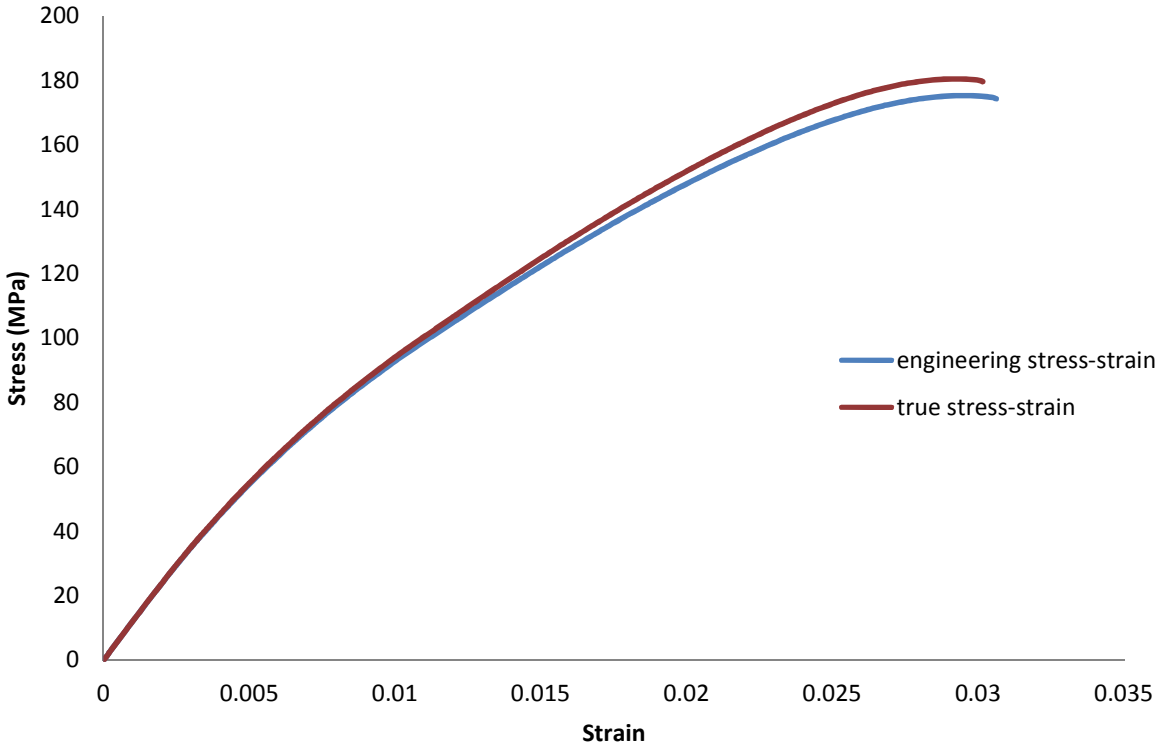

Figure 73 - True and Engineering stress-strain relation

Secondly, the stress-strain curve input in the material card concerns only the plastic domain. Therefore, the curve used is the true stress versus the effective plastic strain. The curve should be smooth and utilising a

minimal number of points. The input of a noisy experimental data may cause unwanted behaviour reaction (see Figure 74, Table 30 and Figure 75). The effective plastic strain (ε_{ep}) is defined as follows with E representing the elastic Young's modulus:

$$\varepsilon_{ep} = \varepsilon_{true} - \frac{\sigma_{true}}{E}$$

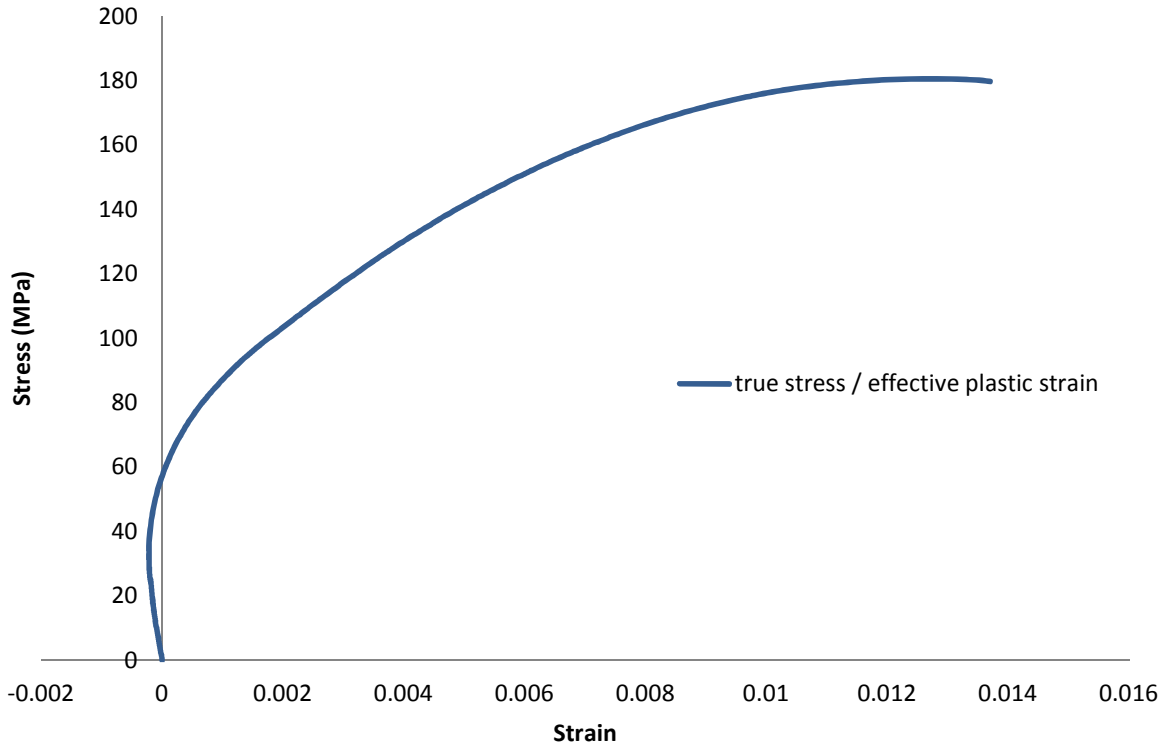

Figure 74 - True stress / Effective Plastic Strain

The first plastic strain value should be input as zero and the first stress value should be the initial yield stress.

Table 30 - Smoothed stress / effective plastic strain curve

σ_{true}	ε_{ep}	σ_{true}	ε_{ep}
57,57	0	107,23	0,002
62,79	0,0001	122,55	0,003
66,99	0,0002	136,37	0,004
71,02	0,0003	148,08	0,005
74,17	0,0004	157,9	0,006
77,2	0,0005	165,79	0,007
80,18	0,0006	172,16	0,008
83	0,0007	176,65	0,009
85,1	0,0008	179,43	0,01
87,18	0,0009	180,46	0,011
89,88	0,001	180	0,012

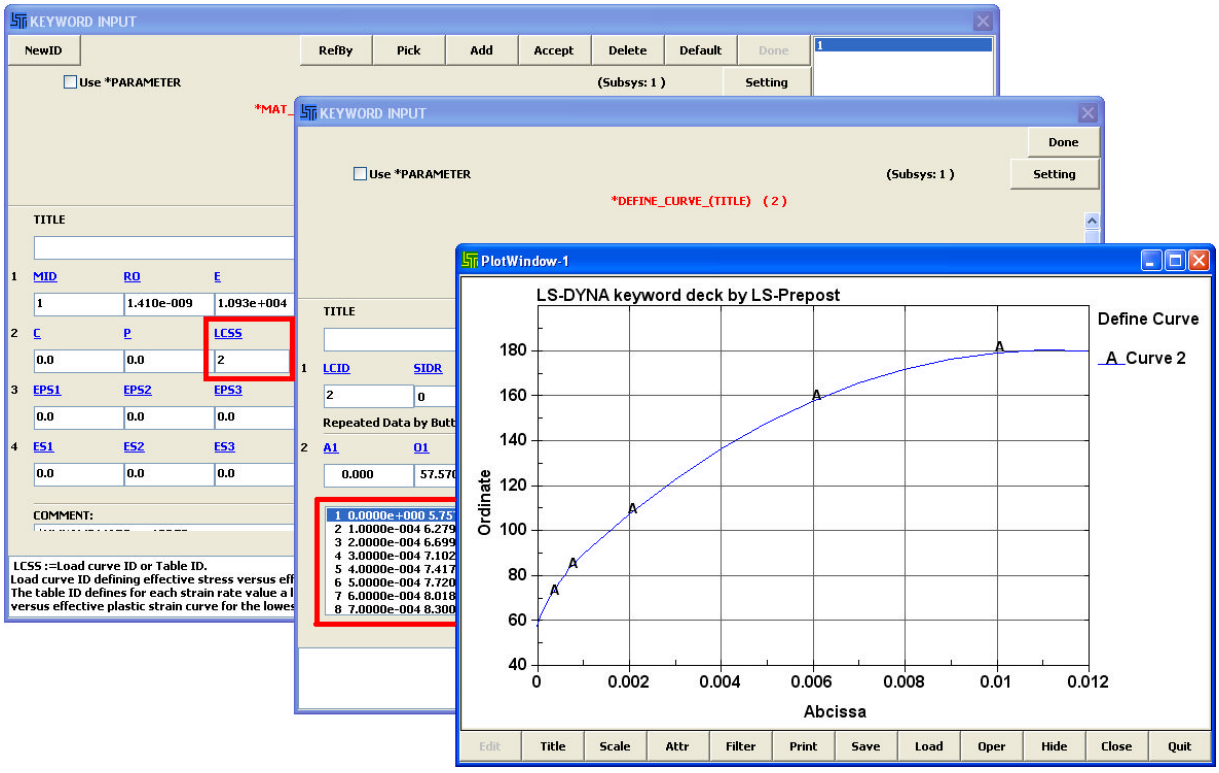

Figure 75 - Implementation of defined stress-strain curve in LS-Dyna

The material failure is considered in each model using strain failure criterion. If the calculated effective plastic strain for any element exceeds the predefined value, the element will be removed from the model and the simulation continues with the eroded model. However, with thermoplastics, if the strain rate increases the failure strain drops but the model understands that this parameter is constant and independent. That is the reason why, if simulations follow only one curve defined in LCSS it will only well represent the material behaviour in one condition. If very different strain rate are applied, it is as many curves to input. This can be done by defining many materials per conditions or by using LCSR in which several stress-strain curves are defined together with a parameter setting the velocity for which each curve is representative.

Concerning the impactor or projectile, it can be defined with a rigid material (MAT_RIGID).

Initial and Boundary conditions

Initial load

In general case in the simulation, an impact can be defined via a displacement over the time or via an initial velocity. In a localised impact

due to a projectile, the initial velocity is the right way to define the kinetic energy of impact (VELOCITY_NODE).

Contact

A contact algorithm should be formulated to prevent interpenetration between the projectile and the impacted surface or self-contact during the crash. The accurate modelling of the contact interfaces between each part is critical to have good and accurate prediction capability with the simulations. In LS-DYNA, a contact is defined by identifying what locations are to be checked for a potential penetration of a slave node through a master segment. In the case of a penalty-based contact, when a penetration is found a force proportional to the penetration depth is applied to resist and ultimately eliminate the penetration. The automatic contact options are recommended, as these contacts are non-oriented. This means that they can detect penetration coming from either side of a shell element. In the case of shell elements, automatic contact types determine the contact surfaces by projecting normally from the shell mid-plane a distance equal to one-half the contact thickness. Further, at the exterior edge of a shell surface, the contact surface wraps around the shell edge with a radius equal to one-half the contact thickness thus forming a continuous contact surface. The contact treatment allows for compression and tangential loads to be transferred between the slave nodes and the master segments. The choice of the master and slave surfaces is arbitrary when the symmetric penalty treatment is

employed. Otherwise, the most coarsely meshed surface should be chosen as the master surface unless there is a large difference in mass densities in which case the side corresponding to the material with the highest density is recommended. The projectile is assigned as master and the impacted part is assigned as slave and the recommended contact is the AUTOMATIC_SURFACE_TO_SURFACE.

Boundary conditions

The model boundary conditions are essential in the simulations. There are defined by single point constraint (SPC) on the nodes of the model.

Output Database

In Dbase, numerous of outputs can be defined. The ASCII_option (DATABASE_OPTION) allows setting the wanted data and defines a time interval between outputs: *Global Statistics, Material Energies, Nodal/Resultant Interface Forces, Nodal Displacement/Velocity/Acceleration data, Element Output Data, Sliding Interface Energies* and so on. DATABASE_BINARY_D3PLOT defines the time interval between complete output states. DATABASE_BINARY_D3THDT defines the time interval between outputs of time history data for elements subsets (DATABASE_HISTORY). The histories of particular nodes or elements can be set for interests via DBHist.

Other controls

CONTROL_TERMINATION: time of the impact event/ CONTROL_TIMESTEP: if the calculation time is excessive, it can be reduced by increasing the time step calculation (to be use with caution).

Post-Processing

Mode animation

D3PLOT animation is the animation defined in DATABASE_D3PLOT. The animation displayed is just a representation and should be taken for what it is and not for being truly realistic. The Fringe plotting (Fcomp) allows displaying different parameters in different axis or plans into the animation according to a colour scheme: *stress, plastic strain, displacement* and so on.

Section analysis

ASCII and Time history plotting or History allows plotting relevant parameters (*stress, effective plastic strain, force, displacement, energies, etc.*). These simulated data can be compared with the experimental data in order to assess the accuracy of the defined model. The stress-strain can be retrieved and plotted against the experimental curve. The force or displacement histories can also be compared against the experimental data (see Figure 76).

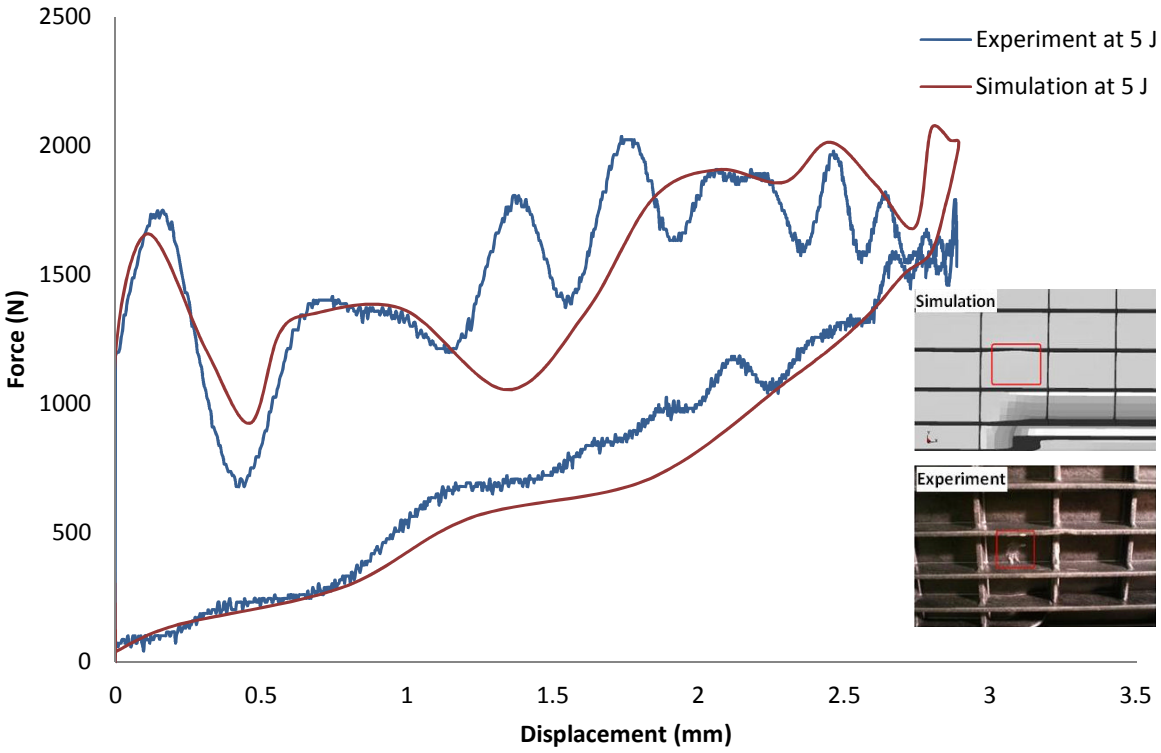

Figure 76 - 10 mm impact from a 22 g projectile at 5 joules

Figure 76 shows the force versus displacement on a PA66-GF35 impacted at 5 J experimentally and into the simulations. The experimental impact is measured from the impactor of the falling weight impact tester whereas the simulated air gun impact is measured from an element of the base wall in the area of the impact point. There are some variations on the forces, and particularly half way into the deflection. However, the general behaviour of the simulated impact is correlating to some extent with the experimental impact. Both impacts start to deflect at approximately an

equivalent force of 1200 N, and fail after 0.5 mm deflection. From then on, the increase of the damage is arbitrary, the forces fluctuate but augment. The maximum deflections are matching at around 2.88 mm. The recovering rate to the initial position follows a comparable slope.

Appendix 5: Traction tests on oil pick-up pipes to evaluate friction weld strength

Conditions, samples and preparation

Tests were performed at the Cranfield Mechanical Testing Laboratory on a 5/100 kN Instron 5500R Electro-mechanical Test Instrument.

Traction Rate: 1 mm/min

Air Temperature: 21.9-22.4 °C

Five oil pans were tested, labelled as follows:

Numbering	Date	Material	Modifications
1	Mai (2011)	A3WG7	OSI
2	April (2011)	A3WG7	OSI
3	April (2011)	A3WG7	OSI
4	2011	A3WG7	No modifications
5	2010	A3WG7	No modifications

Table 31 - Oil pan samples tested

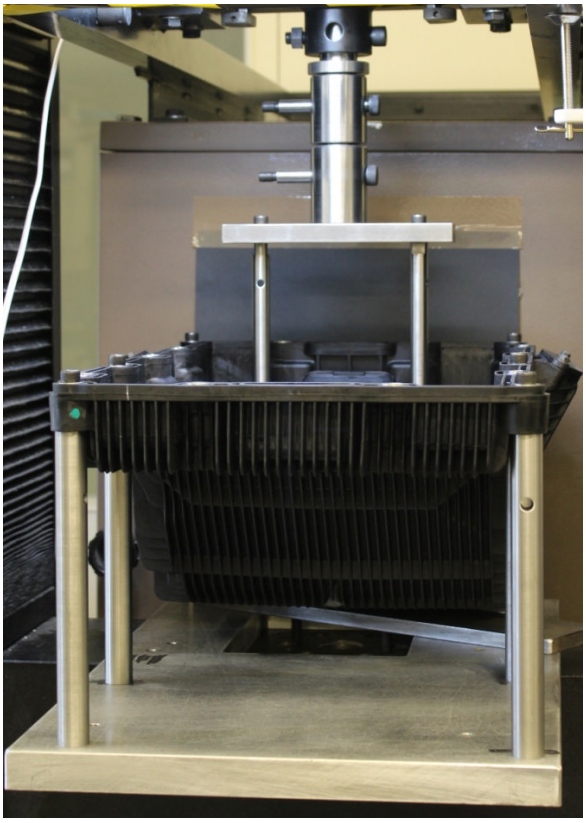

Figure 77 - Test set-up

The oil pans (Table 31) are attached on a cradle steel plate bolted to the moving part of the machine (Figure 77). At the top, a fixture is pined to the fixed end part of the machine where the load cell is. A transversal bar shackles the natural notch of each oil pump pickup. When the set-up is done (Figure 78 and Figure 79), the test starts with the oil pan going down at a speed rate of 1 mm/min.

Oil pans (1, 2 and 3) have the same outer design and oil pump pickup – **Prod. Avalon Reversible**

Figure 78 - View of the Avalon Reversible Oil Pump Pickup

Oil pans (4 and 5) have the same outer design and oil pump pickup - **Hawkeye**

Figure 79 - View of the Hawkeye Oil Pump Pickup

Results

Load vs. Extension curves (1, 2 and 3 A3WG7 OSI) – Production Avalon Reversible

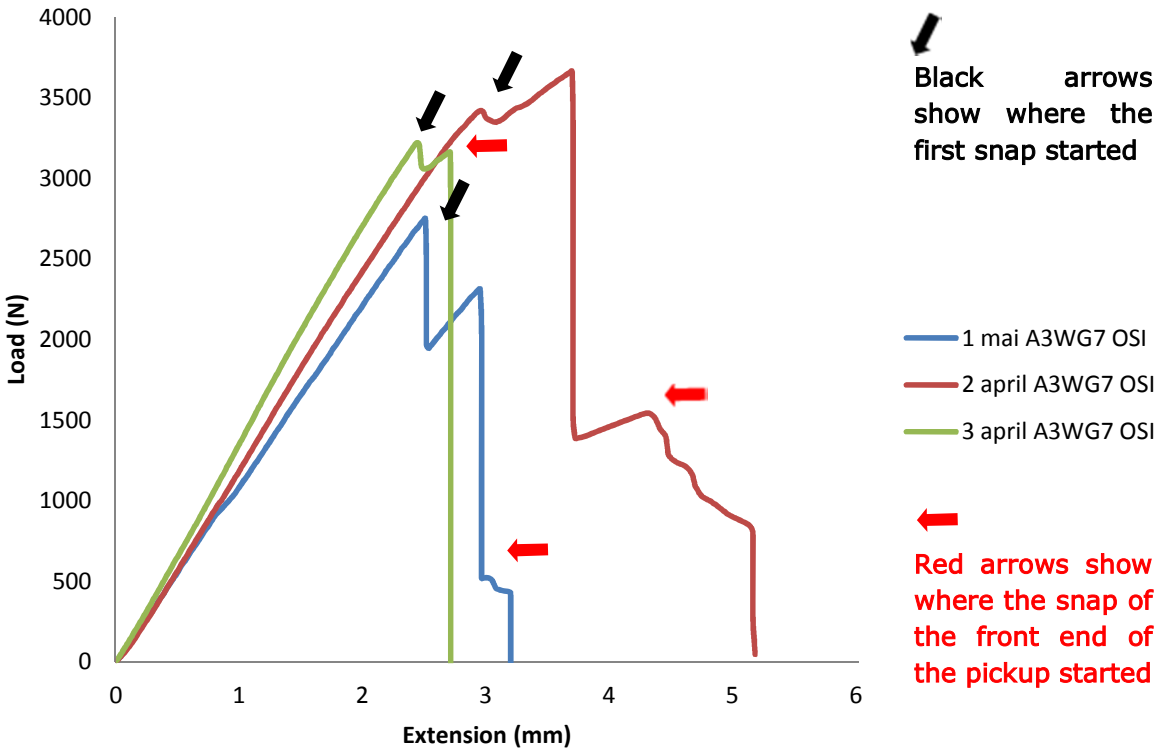

1 – after the test

2 – after the test

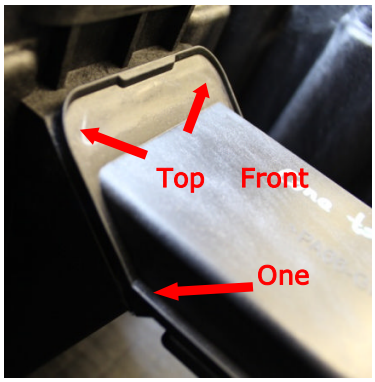

3 – after the test

Figure 80 - Tests on the Production Avalon Reversible Oil Pans

Two ways of failure were observed (Figure 80): (1) and (2) had three steps, respectively one side failed followed by its opposite one then the complete end of the pickup snapped. (3) had two close steps, respectively the sides failed together and quickly followed by the top front end of the pickup. This difference could be explained by the imperfect horizontality between the bar that shackles the pickup and its surface area in contact. Even a very small angle will affect the way the force is applied. If it is the case, the test with (3) is the one to look at or take into consideration. Nonetheless, the comparable conclusion is that the sides failed before the top front end of the pickup. The first failure occurred between 2.4 and 2.9 mm at between 2.75 and 3.4 kN.

Load vs. Extension curves (4 and 5 A3WG7 no modifications) – Hawkeye

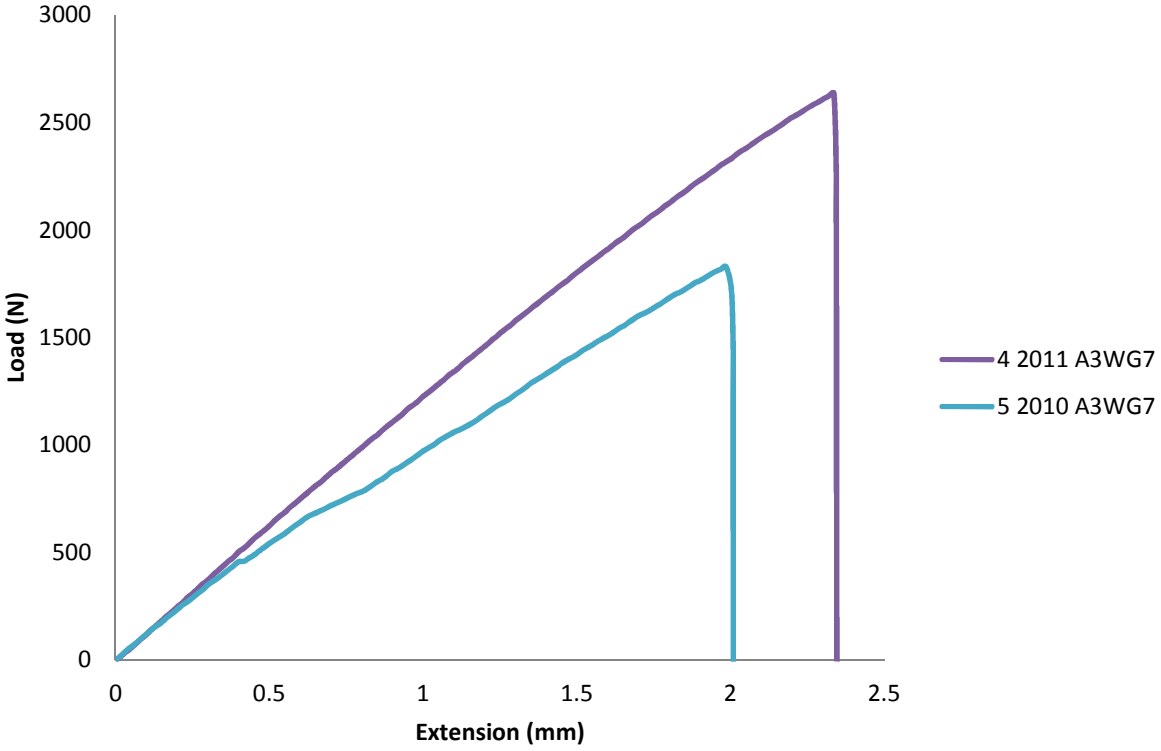

4 – after the test

5 – after the test

Figure 81 - Tests on the Hawkeye Oil Pans

The explanation previously given about the imperfect horizontality can be applied here as well. However, due to the important inclination of the front end, the sequence of events is slightly different. In the Figure 81, (4) snapped homogeneously in one step at 2.34 mm whereas (5) had a snap at 0.4 mm with no visible damage before to completely snap at 2 mm. Again, if the statement applies, the test with (4) is the one to be considered as good.

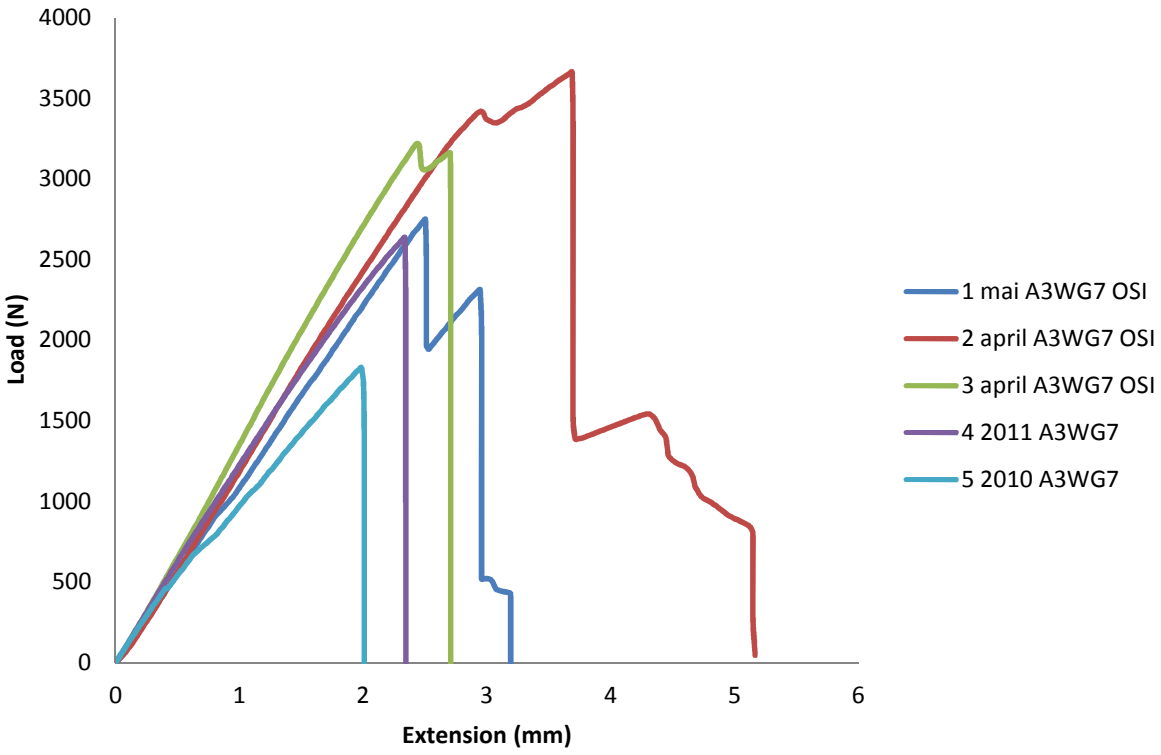

Figure 82 - Load vs. Extension Curves of all of the 5 oil pans

The graph in Figure 82 compiles load versus extension curves of all the 5 oil pans (3 Production Avalon Reversible and 2 Hawkeye) but the test (1,2 and 3) is not completely comparable with the test (4 and 5) as the notch in each design is different and the force applied is not stressing the same surface area. This force is spread in a much bigger area with the Production Avalon Reversible than the Hawkeye.